

Aspects of QCD perturbative evolution

Andrea Piccione

*Dipartimento di Fisica, Università di Genova
and
INFN, Sezione di Genova,
Via Dodecaneso 33, I-16146 Genova, Italy*

Abstract

This thesis is devoted to the study of some aspects of perturbative QCD, and in particular to the development of high-precision techniques for the extraction of physical parameters such as structure functions, parton distributions, and the strong coupling from the analysis of deep inelastic scattering data. First, we will discuss scaling violations of singlet and nonsinglet truncated moments, and the use of truncated moments to solve the Altarelli-Parisi equation. Then we will suggest an approach based on neural networks to the parametrization and interpolation of experimental data, which retains information on experimental errors and correlations. The method of truncated moments can be combined with the neural network fit to extract various quantities of phenomenological interest in a bias-free way. As an example of such application, we will discuss the determination of the strong coupling constant.



Università degli Studi di Genova

Facoltà di Scienze Matematiche Fisiche e Naturali

Andrea Piccione

Aspects of QCD perturbative evolution

Tesi di Dottorato in Fisica

Dicembre 2001

Relatore:
Dr. G. Ridolfi

Relatore esterno:
Dr. S. Forte

a Tania

Contents

1	Introduction	1
2	Basics of QCD	5
2.1	$SU(N)$ gauge invariance	5
2.2	QCD Lagrangian	8
2.3	Feynman rules	9
2.4	Running coupling	12
2.4.1	The β function	12
2.4.2	Asymptotic freedom and confinement	14
2.4.3	Thresholds at quark masses	16
3	QCD and the parton model	19
3.1	Deep inelastic scattering and the parton model	19
3.2	Factorization	22
3.2.1	Coefficient functions	25
3.3	Evolution equations	26
3.3.1	Scaling violations and the Altarelli-Parisi equations	26
3.3.2	Solution of the Altarelli-Parisi equations	28
3.4	Factorization schemes	30
3.4.1	The unpolarized case: $\overline{\text{MS}} \rightarrow \text{DIS}$	31
4	Truncated Moments of parton distributions	35
4.1	Evolution equations for truncated moments and their solutions	36
4.2	Numerical methods and their accuracy	40
4.3	Techniques for phenomenological applications	43
4.4	Solving the Altarelli-Parisi equation with truncated moments	48
5	Introduction to Neural Networks	57
5.1	From biology to artificial neural networks	57
5.2	Multilayer Neural Networks	59

5.3	Learning process of Neural Networks	61
5.3.1	A simple perceptron learning algorithm	61
5.3.2	Learning by error back-propagation	63
5.4	Practical issues	64
5.4.1	Rules of thumb	65
5.4.2	Generalization	66
6	Neural Network fit of F_2	69
6.1	Experimental data	69
6.1.1	NMC	70
6.1.2	BCDMS	71
6.2	Fitting procedure	72
6.3	Generation of artificial data	75
6.4	Building and Training Neural Networks	79
6.4.1	Non-singlet	86
6.4.2	Proton and Deuteron	89
6.5	Results	90
7	Determination of α_s with truncated moments	95
7.1	The DIS phenomenology	95
7.1.1	Target Mass Corrections	95
7.1.2	Renormalization and factorization scales	98
7.1.3	Elastic contribution	99
7.1.4	Evolution uncertainties	99
7.2	Fitting procedure and results	100
7.3	The theoretical uncertainties	105
8	Conclusions	109
A	Diagonalization of triangular matrices	111
B	Tools of statistics	113
B.1	Distribution of several random variables	113
B.2	Gaussian distribution	114
B.3	Estimators for mean, variance, covariance	115
B.4	Least squares minimization	118
C	Numerical routines	123
	References	125

1

Introduction

Quantum Chromodynamics (QCD) is believed to be the theory of strong interactions. QCD as a gauge theory of quarks and gluons is unique among renormalizable theories in providing a basis for the parton model within the principles of relativistic quantum field theory and at present times it stands as a main building block of the “Standard Model” of the fundamental interactions.

The strength of electro-weak interaction is so weak that perturbation theory is extremely reliable. Furthermore, the leptons are at the same time the fields in the Lagrangian and the particles in the detector. The case of QCD is different in both respects. Perturbative methods are only applicable in those particular domains of strong interactions physics where the asymptotic freedom can actually be reached. Although there are several attempts to describe non-perturbative effects of QCD, at present times we have not yet a solution of QCD in the low-energy domain. Also, QCD is a theory of quarks and gluons, while the real world is made up of hadrons. Clearly, some model is needed to match one to the other.

Essentially all physic aspects of present and future hadron colliders, from particles searching beyond the Standard Model to electro-weak precision measurements and study of heavy quarks, need a detailed information on the hadronic initial states. Factorization is a central issue, as it allows to separate perturbative and non-perturbative contributions. In particular, it ensures that a non-perturbative quantity, as a structure function, is process independent. As a consequence, we can extract structure functions from, say, deep inelastic scattering processes, and use them as inputs for a hadron-hadron collision. Thus, we need a knowledge as precise as possible on the inputs of hadron colliders that we extract from other processes.

The present thesis is devoted to the study of some aspects of perturbative QCD, and in particular to the development of high-precision techniques for the extraction of phenomenological parameters such as structure functions,

parton distributions, and the strong coupling from the analysis of deep inelastic scattering data. This analysis is usually characterized by theoretical assumptions on the phenomenological parameters, such as the functional parametrizations of the structure functions or the small- x behavior of parton distributions. These assumptions introduce potentially large biases, whose size is very hard to assess.

In this thesis we will develop methods to reduce the sources of theoretical uncertainties. Specifically, we will first extend the method of truncated moments from its original formulation for the non-singlet parton distributions to all flavor combinations. Truncated moments of parton distributions are defined by restricting the integration range over the Bjorken variable to an experimentally accessible subset $x_0 < x < 1$ of the allowed kinematic range $0 < x < 1$. As a consequence this method provides a way to avoid theoretical biases on the small- x behavior of parton distributions.

Special attention will be devoted to the numerical implementation of the technique of truncated moments. We will write the evolution equations for truncated moments in a particular form, which has the advantage of increasing the efficiency of the method considerably.

A crucial ingredient of most phenomenological analyses is the technique adopted to interpolate experimental data, and to reproduce the corresponding errors and correlations. We will suggest an approach to this problem based on neural networks. We will show that with this method it is possible to extract information from experimental data without introducing a functional parametrization of structure functions based on theoretical assumptions. Errors and correlations of the data points will be determined by a Monte Carlo technique. We will discuss results and details of the numerical implementation, based on a subset of the available experimental data for unpolarized deep inelastic scattering.

The method of truncated moments can be combined with the neural network fit to extract various quantities of phenomenological interest in a bias-free way. Here, as an application, we will adopt these techniques to determine the strong coupling constant. Other possible applications will be sketched in the conclusions.

In Chapters 2 and 3 we will define our frameworks, *i.e.* QCD and the parton model. Besides all the general issues, such as the QCD Lagrangian, the Feynman rules, running coupling constant, deep inelastic scattering cross section and parton distributions evolution equations, we will discuss in detail some technical issues, such as the matching of the running coupling constant at quarks mass thresholds and the change of factorization schemes, since they are essential ingredients of our analysis.

In Chapter 4 we will introduce the method of truncated moments. We will derive the relevant evolution equations and the corresponding solution.

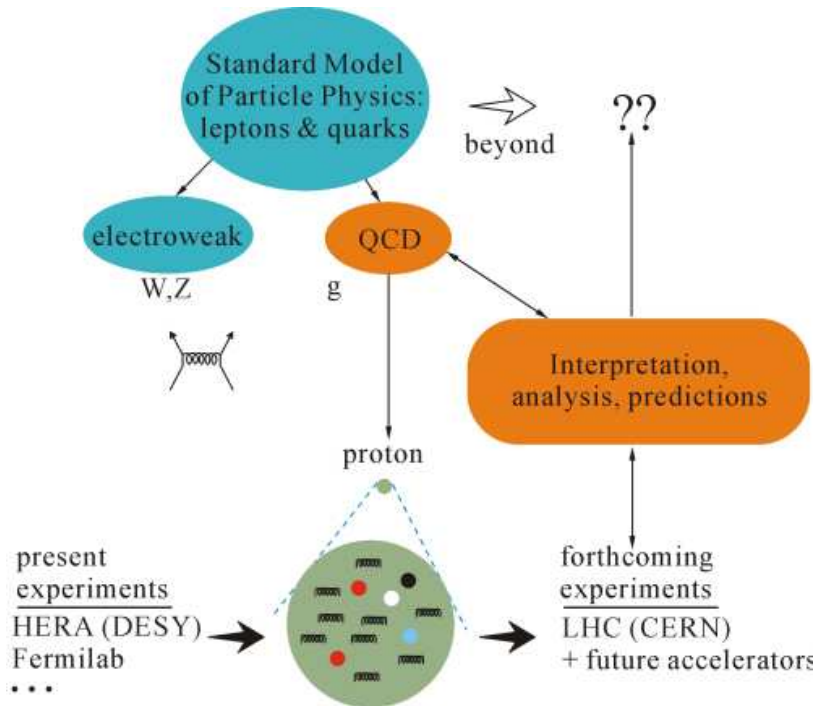


Figure 1.1. *General framework.*

We will discuss the numerical accuracy of the technique, and the way it can be implemented for phenomenological applications.

Chapter 5 is a very brief introduction to neural networks and it is mainly devoted to introduce the main algorithms and some practical rules. In Chapter 6, we will first describe the main features of the experimental data, and we will discuss under which conditions we can reproduce them by a Monte Carlo technique. Then, we will address to the neural network fit of data, and we will give details on the behavior of neural networks, such as their ability of finding an underlying law, and on the way we have to train them.

As an application, the efforts of the previous Chapters will be used in Chapter 7 to give a determination of the strong coupling constant α_s . The phenomenology of deep inelastic scattering will be completed with the discussion of target mass corrections, the renormalization scale dependence, and the corrections due to the elastic contributions. The fitting procedure, as well as the estimation of the theoretical errors, will be illustrated in detail. Finally, in Chapter 8 we will summarize and discuss results and outlook.

2

Basics of QCD

This chapter is a very basic and brief introduction on QCD. Lots of reviews on this subject have been written (see *e.g.* [1, 2, 3]), and we could not write about it better. Here we will limited ourselves to introduce the essential aspects of the QCD framework, as the $SU(N)$ gauge invariance, the QCD Lagrangian and the Feynman rules. We will pay more attention on the running coupling α_s , as it is an essential tool for Chapter 7. For this purpose, a very technical issue as matching conditions on quark mass thresholds will be reviewed with details.

2.1 $SU(N)$ gauge invariance

We are interested in building a Lagrangian invariant under local phase transformations related to a non-Abelian group. We consider the Lagrangian

$$\mathcal{L} = i\bar{\psi}\gamma_\alpha\partial^\alpha\psi \quad (2.1.1)$$

and the transformation

$$\psi(x) \rightarrow U(x)\psi(x) \quad (2.1.2)$$

where

$$U(x) = \exp[ig\omega^A(x)t^A] \quad (2.1.3)$$

in which the t^A are the N^2-1 traceless Hermitean matrices generating $SU(N)$ and satisfying the relations

$$[T^A, T^B] = if^{ABC}T^C, \quad (T^A)_{BC} = -if^{ABC}. \quad (2.1.4)$$

By convention the normalization of the $SU(N)$ matrices is chosen to be

$$\text{Tr } t^A t^B = T_R \delta^{AB}, \quad T_R = \frac{1}{2}. \quad (2.1.5)$$

With this choice, the generators obey the following relations:

$$\sum_A t_{ab}^A t_{bc}^A = C_F \delta_{ac}, \quad C_F = \frac{N^2 - 1}{2N} \quad (2.1.6)$$

$$\text{Tr } T^C T^D = \sum_{A,B} f^{ABC} f^{ABD} = C_A \delta^{CD}, \quad C_A = N. \quad (2.1.7)$$

As U depends on x , the derivative term $\partial_\alpha \psi$ no longer transforms as it should: indeed

$$\partial_\alpha \psi \rightarrow \partial_\alpha U \psi = (\partial_\alpha U) \psi + U \partial_\alpha \psi \neq U \partial_\alpha \psi. \quad (2.1.8)$$

We now look for a generalization of the derivative which does not spoil the invariance of \mathcal{L} . We define accordingly the *covariant derivative* D_α by demanding that

$$D_\alpha \psi \rightarrow U D_\alpha \psi \quad (2.1.9)$$

or in operator form

$$D_\alpha \rightarrow D'_\alpha = U D_\alpha U^{-1}. \quad (2.1.10)$$

Since D_α is to generalize ∂_α , let us introduce the *ansatz*

$$D_\alpha = \partial_\alpha I + ig A_\alpha(x) \quad (2.1.11)$$

where $A_\alpha(x)$ is the $N \times N$ Hermitean matrix defined by

$$A_\alpha = A_\alpha^A t^A. \quad (2.1.12)$$

The transformation requirement (2.1.10) implies that

$$A'_\alpha = U A_\alpha U^{-1} - \frac{i}{g} U \partial_\alpha U^{-1}. \quad (2.1.13)$$

We have enlarged our Lagrangian in order to have $SU(N)$ local invariance, but we have introduced $N^2 - 1$ vector fields to build the covariant derivative. In order to give these fields an existence on their own, we should include their kinetic terms in a way that does not break the original local symmetry. The Hermitean quantity

$$F_{\alpha\beta} \equiv -\frac{i}{g} [D_\alpha, D_\beta] \quad (2.1.14)$$

will transform covariantly since D_α does, *i.e.*

$$F_{\alpha\beta}(x) \rightarrow U(x) F_{\alpha\beta}(x) U^{-1}(x). \quad (2.1.15)$$

Using the definition of the covariant derivative (2.1.11), we obtain

$$F_{\alpha\beta} = \partial_\alpha A_\beta - \partial_\beta A_\alpha + ig [A_\alpha, A_\beta] \quad (2.1.16)$$

that is the Yang-Mills generalization of the field strengths of electromagnetism. The kinetic term is then given by

$$\mathcal{L}_{YM} = -\frac{1}{4}(F_{\alpha\beta}F^{\alpha\beta}) \quad (2.1.17)$$

with the normalization of eq. (2.1.5) for the T -matrices. \mathcal{L} does not depend on the representation of the fermions and therefore stands on its own as a highly non-trivial theory.

If we consider the equation of motion without sources we have

$$D^\alpha F_{\alpha\beta} = 0. \quad (2.1.18)$$

Just as in electrodynamics, there are plane waves solutions and they have infinite energy (but finite energy density). However, unlike in Maxwell's theory, they cannot be superimposed to produce finite energy solutions because of the non-linear nature of this theory, unless they move in the same direction. In addition the $F_{\alpha\beta}$ fields satisfy the kinematic (Bianchi) constraints

$$D_\alpha \tilde{F}^{\alpha\beta} = 0 \quad (2.1.19)$$

where

$$\tilde{F}^{\alpha\beta} = \frac{1}{2}\epsilon^{\alpha\beta\gamma\delta} F_{\gamma\delta} \quad (2.1.20)$$

is the dual of $F_{\alpha\beta}$. We emphasize that (2.1.19) is not an equation of motion since it is trivially solved by expressing $F_{\alpha\beta}$ in terms of the potentials.

There is even another way to construct a gauge and Lorentz invariant kinetic term from $F_{\alpha\beta}$, that is

$$I = \text{Tr} \epsilon^{\alpha\beta\gamma\delta} F_{\alpha\beta} F_{\gamma\delta}. \quad (2.1.21)$$

We did not consider this term as it can be expressed as a pure divergence

$$\epsilon^{\alpha\beta\gamma\delta} \text{Tr} F_{\alpha\beta} F_{\gamma\delta} = 4\partial_\gamma W^\gamma \quad (2.1.22)$$

with

$$W^\gamma = \epsilon^{\alpha\beta\gamma\delta} \text{Tr} \left[A_\delta \partial_\alpha A_\beta + \frac{2ig}{3} A_\delta A_\alpha A_\beta \right]. \quad (2.1.23)$$

This means that by taking I as the kinetic Lagrangian, we could not generate any equation of motion for the vector potential since it would only affect the action at its end points.

Finally note that there is no gauge invariant way of including a mass for the gauge boson. A term such as

$$m^2 A^\alpha A_\alpha, \quad (2.1.24)$$

is not gauge invariant. This is very similar to the Quantum Electrodynamics (QED) requirement of a massless photon. On the other hand a mass term for the fermions given by

$$m\bar{\psi}\psi, \quad (2.1.25)$$

is gauge invariant.

2.2 QCD Lagrangian

QCD is an $SU(3)$ gauge invariant field theory. The expression for the classical Lagrangian density is

$$\mathcal{L}_{\text{classical}} = -\frac{1}{4}F_{\alpha\beta}^A F_A^{\alpha\beta} + \sum_{\text{flavors}} \bar{q}_a (i \not{D} - m)_{ab} q_b, \quad (2.2.1)$$

where $\not{D} = \gamma_\alpha D^\alpha$, the metric is given by $g^{\alpha\beta} = (1, -1, -1, -1)$ and $\hbar = c = 1$. These terms describe the interaction of spin- $\frac{1}{2}$ quarks of mass m and massless spin-1 gluons. $F_{\alpha\beta}^A$ is the field strength tensor derived from the gluon field A_α^A

$$F_{\alpha\beta}^A = \partial_\alpha A_\beta^A - \partial_\beta A_\alpha^A - g f^{ABC} A_\alpha^B A_\beta^C \quad (2.2.2)$$

and the indices A, B, C run over the eight color degrees of freedom of the gluon field. It is the third “non-Abelian” term on the *r.h.s.* of eq. (2.2.2) which distinguishes QCD from QED, giving rise to triplet and quartic gluon self-interactions and ultimately to the property of asymptotic freedom. Note that each term in the Lagrangian has mass dimension four, in order to give the correct dimensions for the action when integrated over all space-time. It follows that the dimensions of the fields q_a and A_α^A are $\frac{3}{2}$ and 1, respectively.

The explicit sum in eq. (2.2.1) runs over the n_f different flavors of quarks, g in eq. (2.2.2) is the coupling constant which determines the strength of the interaction between colored quanta, and f^{ABC} ($A, B, C = 1, \dots, 8$) are the structure constants of the $SU(3)$ color group. The quark fields q_a are in the triplet representation of the color group, ($a = 1, 2, 3$) and D is the covariant derivative (2.1.11). Acting on triplet and octet fields the covariant derivatives takes form

$$(D_\alpha)_{ab} = \partial_\alpha \delta_{ab} + ig(t^C A_\alpha^C)_{ab}, \quad (D_\alpha)_{AB} = \partial_\alpha \delta_{AB} + ig(T^C A_\alpha^C)_{AB}, \quad (2.2.3)$$

where t and T are matrices in the fundamental and adjoint representations of $SU(3)$ respectively. A representation for the generators t^A is provided by the eight Gell-Mann matrices λ^A , which are Hermitean and trace-less,

$$t^A = \frac{1}{2}\lambda^A. \quad (2.2.4)$$

For the specific case of $SU(3)$, from eqs. (2.1.6) and (2.1.7) we have

$$C_F = \frac{4}{3} \quad C_A = 3. \quad (2.2.5)$$

2.3 Feynman rules

It may be shown (see *e.g.* [4, 5]) that it is not possible to define the propagator for the gluon field, without making a choice of the gauge. As a consequence without a choice of gauge we can not perform perturbation theory with the Lagrangian of eq. (2.2.1). The choice

$$\mathcal{L}_{\text{gauge-fixing}} = -\frac{1}{2\lambda} (\partial^\alpha A_\alpha^A)^2, \quad (2.3.1)$$

fixes the class of *covariant gauges* with gauge parameter λ . Two common choices are the Feynman gauge, $\lambda = 1$, and the Landau gauge, $\lambda = 0$. In the following we will consider a general case. In a non Abelian theory such as QCD the covariant gauge fixing term must be supplemented by a ghost Lagrangian, which is given by

$$\mathcal{L}_{\text{ghost}} = \partial_\alpha \eta^{A\dagger} (D_{AB}^\alpha \eta^B). \quad (2.3.2)$$

Here η^A is a complex scalar field which obeys Fermi statistics. The derivation of the form of the ghost Lagrangian is best provided by the path integral formalism and the procedures of Faddeev and Popov. The ghost field cancel unphysical degrees of freedom which would otherwise propagate in covariant gauges.

Eqs. (2.2.1),(2.3.1) and (2.3.2) are sufficient to derive the Feynman rules of the theory in a covariant gauge. The Feynman rules are defined from the operator

$$S = i \int d^4x \mathcal{L}(x) \quad (2.3.3)$$

which gives the phase of transition amplitude, rather than from the Lagrangian density. The Lagrangian density can be separated into a free piece

\mathcal{L}_0 , which normally contains all the terms bilinear in the fields, and an interaction piece, \mathcal{L}_I , which contains all the rest:

$$S = S_0 + S_I,$$

$$S_0 = i \int d^4x \mathcal{L}_0(x), \quad S_I = i \int d^4x \mathcal{L}_I(x). \quad (2.3.4)$$

The practical recipe to determine the Feynman rules is that the inverse propagator is derived from $-S_0$, whereas the Feynman rules for the interacting parts of the theory which are treated as perturbations are derived from S_I .

In order to understand this recipe, we will follow [2] and compare the following two different approaches to the quantization of a theory. For simplicity, we will take a theory which contains only a complex scalar field ϕ and an action which contains only bilinear terms, $S = \phi^*(K + K')\phi$. In the first approach, both K and K' are included in the free Lagrangian, $S_0 = \phi^*(K + K')\phi$. Using the above rule the propagator Δ for the ϕ field is given by

$$\Delta = \frac{-1}{K + K'}. \quad (2.3.5)$$

In the second approach K is regarded as the free Lagrangian, $S_0 = \phi^*K\phi$, and K' as the interaction Lagrangian, $S_I = \phi^*K'\phi$. Now S_I is included to all orders in perturbation theory by inserting the interaction term an infinite number of times:

$$\begin{aligned} \Delta &= \frac{-1}{K} + \left(\frac{-1}{K}\right) K' \left(\frac{-1}{K}\right) + \left(\frac{-1}{K}\right) K' \left(\frac{-1}{K}\right) K' \left(\frac{-1}{K}\right) + \dots \\ &= \frac{-1}{K + K'}. \end{aligned} \quad (2.3.6)$$

We observe that with the choice of signs described above the full propagator of the ϕ field is the same in both approaches, demonstrating the internal consistency of the recipe.

The quark and the gluon propagators are obtained using the free piece \mathcal{L}_0 of the QCD Lagrangian given in eq. (2.2.1). Thus, for example, the inverse fermion propagator in momentum space can be obtained by making the identification $\partial^\alpha = -ip^\alpha$ for an incoming field. In momentum space the two point function of the quark field depends on a single momentum p . We have

$$\Gamma_{ab}^{(2)}(p) = -i\delta_{ab}(\not{p} - m), \quad (2.3.7)$$

which is the inverse of the propagator given in Fig. 2.1. The $i\epsilon$ prescription for the pole of the propagator is added to preserve causality, exactly the same

Figure 2.1. *Feynman rules for QCD in a covariant gauge for gluons (curly lines), fermions (solid lines) and ghosts (dotted lines) as given in Ref. [2].*

way as in QED. Similarly the inverse propagator of the gluon field is given by

$$\Gamma_{\{AB,\alpha\beta\}}^{(2)}(p) = i\delta_{AB} \left[p^2 g_{\alpha\beta} - (1 - \frac{1}{\lambda}) p_\alpha p_\beta \right]. \quad (2.3.8)$$

It is straightforward to check that without the gauge fixing term this function would have no inverse. The result for the gluon propagator Δ is

$$\Gamma_{\{AB,\alpha\beta\}}^{(2)}(p) \Delta^{(2) \{BC,\beta\gamma\}}(p) = \delta_A^C g_\alpha^\gamma \quad (2.3.9)$$

$$\Delta^{(2) \{BC,\beta\gamma\}}(p) = \delta_{BC} \frac{i}{p^2} \left[-g_{\beta\gamma} + (1 - \lambda) \frac{p_\beta p_\gamma}{p^2} \right]. \quad (2.3.10)$$

Replacing the derivatives with the appropriate momenta, eqs. (2.2.1), (2.3.1) and (2.3.2) can be used to derive all the rules in Fig. 2.1.

2.4 Running coupling

The QCD coupling constant is defined by

$$\alpha_s = \frac{g^2}{4\pi}, \quad (2.4.1)$$

that is the strong-interactions analogue of the fine-structure constant. When we compute Feynman diagrams divergences arise and we need to regularize them. The most commonly used regularization scheme is the *Modified Minimal Subtraction* ($\overline{\text{MS}}$). This involves continuing momentum integrals from 4 to $4 - 2\epsilon$ dimensions, and then subtracting off the resulting $1/\epsilon$ poles and also $\log 4\pi - \gamma_E$ with γ_E being the Euler-Mascheroni constant. To preserve the dimensionless nature of the coupling, a mass scale μ must also be introduced and $g \rightarrow \mu^\epsilon g$. While in QED the coupling constant is defined in a natural way by on-shell renormalization, in QCD, we would like to avoid discussing on-shell quarks, since these are strongly interacting particles that are significantly affected by non-perturbative forces. The use of an arbitrary renormalization point μ allows us to avoid this problem. We will define α_s by renormalization conditions imposed at a large momentum scale μ where the coupling constant is small; this value of α_s can then be used to predict the results of scattering processes with any large momentum transfer.

However, the use of renormalization at a scale μ in a computation involving momentum invariants of order p^2 involves some subtlety when p^2 and μ^2 are very different. In this circumstances, Feynman diagrams with n loops typically contain correction terms proportional to $(\alpha_s \log(p^2/\mu^2))^n$. Fortunately, we can absorb these corrections into the lowest order terms by using the renormalization group to replace the fixed renormalized coupling with a running coupling constant.

2.4.1 The β function

The running of the coupling constant α_s is defined to satisfy the renormalization group equation (RGE)

$$\frac{\partial}{\partial t} \alpha_s(t) = \beta(t), \quad t = \log \frac{Q^2}{\mu^2}, \quad (2.4.2)$$

where μ is the renormalization scale and Q the process energy. In QCD, the β function has the perturbative expansion

$$\beta(t) = -b\alpha_s^2(1 + b'\alpha_s + \dots), \quad (2.4.3)$$

with

$$b = \frac{11C_A - 2n_f}{12\pi} = \frac{33 - 2n_f}{12\pi}, \quad (2.4.4)$$

$$b' = \frac{17C_A^2 - 5C_A n_f - 3C_F n_f}{2\pi(11C_A - 2n_f)} = \frac{153 - 19n_f}{2\pi(33 - 2n_f)}, \quad (2.4.5)$$

where n_f is the number of active light flavors at the scale Q^2 .

In the perturbative region (α_s small), we have

$$t = \int \frac{dx}{\beta(x)} \quad (2.4.6)$$

$$\simeq \frac{1}{b\alpha_s(Q^2)} + \frac{b'}{b} \log \frac{\alpha_s(Q^2)}{\alpha_s(\mu^2)} - C,$$

where C is the integration constant. It follows that

$$\frac{1}{\alpha_s(Q^2)} = bt - b' \log \frac{\alpha_s(Q^2)}{\alpha_s(\mu^2)} + bC. \quad (2.4.7)$$

Neglecting the term b' , eq. (2.4.7) can be written as

$$\frac{1}{\alpha_s(Q^2)} = bt + bC. \quad (2.4.8)$$

The choice of the integration constant is arbitrary, and it is usually linked to the available scales of the energy. Historically, the first choice was done in the '60s where the experimental energies were of the order of MeV. With this choice we can now write the integration constant as function of the normalization scale and of a parameter Λ as

$$C = \log \frac{\mu^2}{\Lambda^2}. \quad (2.4.9)$$

With this definition Λ represents the scale at which the coupling would diverge, if extrapolated outside the perturbative domain. Then, at the Leading Logarithmic Approximation (LLA) we have

$$\alpha_s(Q^2) = \frac{1}{b \log \frac{Q^2}{\Lambda^2}}. \quad (2.4.10)$$

We will now include the b' term, too. In addition we will also let the integration constant be dependent on a scale close to the present experimental energies

$$C = \frac{1}{b\alpha_s(M_Z^2)}, \quad (2.4.11)$$

where M_Z is the mass of the Z boson. Eq. (2.4.7) thus gives

$$\frac{1}{\alpha_s(Q^2)} = \frac{1}{\alpha_0(Q^2)} - b' \log \frac{\alpha_s(Q^2)}{\alpha_s(M_Z^2)} \quad (2.4.12)$$

with $\alpha_0(Q^2)$ satisfying eq. (2.4.8). Finally,

$$\begin{aligned} \alpha_s(Q^2) &= \frac{\alpha_0(Q^2)}{1 - \alpha_0(Q^2)b' \log \frac{\alpha_s(Q^2)}{\alpha_s(M_Z^2)}} \\ &\simeq \alpha_0(Q^2) \left[1 + \alpha_0(Q^2)b' \log \frac{\alpha_0(Q^2)}{\alpha_s(M_Z^2)} + \mathcal{O}(\alpha_0^2(Q^2)) \right]. \end{aligned} \quad (2.4.13)$$

Since

$$\log \frac{\alpha_0(Q^2)}{\alpha_s(M_Z^2)} = -\log(1 + \alpha_s(M_Z^2)bt) \simeq -\log(1 + \alpha_0(M_Z^2)bt), \quad (2.4.14)$$

the expression we will use to fit $\alpha_s(M_Z^2)$ is given by

$$\begin{aligned} \alpha_s(Q^2) &= \frac{\alpha_s(M_Z^2)}{1 + b\alpha_s(M_Z^2) \log \frac{Q^2}{M_Z^2}} \\ &\times \left[1 - \frac{b'\alpha_s(M_Z^2)}{1 + b\alpha_s(M_Z^2) \log \frac{Q^2}{M_Z^2}} \log \left(1 + b\alpha_s(M_Z^2) \log \frac{Q^2}{M_Z^2} \right) \right]. \end{aligned} \quad (2.4.15)$$

For sake of completeness we give the Next-to-Logarithmic-Approximation (NLA) of α_s as a function of Λ

$$\alpha_s(Q^2) = \frac{1}{b \log \frac{Q^2}{\Lambda^2}} \left[1 - \frac{b' \log \log \frac{Q^2}{\Lambda^2}}{b \log \frac{Q^2}{\Lambda^2}} \right]. \quad (2.4.16)$$

Finally note that Λ depends on the logarithmic approximation used. We have

$$\frac{\Lambda_1}{\Lambda_2} = \left(\frac{b}{b'} \right)^{\frac{b'}{2b}}. \quad (2.4.17)$$

where Λ_1 and Λ_2 are defined at LLA and NLA respectively.

2.4.2 Asymptotic freedom and confinement

From eq. (2.4.2) and (2.4.3) we have that, if $b > 0$, *i.e.* $n_f < 16$ as follows from eq. (2.4.4), the coupling constant tends to zero at a logarithmic rate as

the momentum scale increases. Such theories are called *asymptotically free*. In theories of this class, the short distance behavior is completely solvable by Feynman diagram methods. Though ultraviolet divergences appear in every order of perturbation theory, from the renormalization group analysis follows that the sum of these divergences is completely harmless. If we interpret these theories in terms of a bare coupling and a finite cutoff Λ , eq. (2.4.10) indicates that there is a smooth limit in which α_s tends to zero as Λ tends to infinity.

To briefly describe the consequences of asymptotic freedom, we now consider an example coming from electrodynamics. The simplest phase of the electrodynamics is the Coulomb phase. It is characterized by massless photons which mediate a long range $1/R$ potential between external sources. When charged matter particles are present, electrodynamics can be in another phase, the superconducting or the Higgs phase. It is characterized by the condensation of a charged field

$$\langle \Phi \rangle \neq 0. \tag{2.4.18}$$

This condensation creates a gap in the spectrum by making the photon massive. This phenomenon was first described in the context of superconductivity, where Φ is the Cooper pair. The condensation of Φ makes electric currents superconducting. Its effect on magnetic fields is known as the Meissner effect. Magnetic fields cannot penetrate the superconductor except in thin flux tubes. Therefore, when two magnetic monopoles (*e.g.* the ends of a long magnet) are inserted in a superconductor, the flux lines are not spread. Instead, a thin flux tube is formed between them. The energy stored in the flux tube is linear in its length and therefore the potential between two external monopoles is linear (as opposed to the $1/R$ potential outside the superconductor). Such a linear potential is known as a *confining* potential. The same happens when we consider *quark confinement*. As a result we have that if one attempts to separate a color singlet state into colored components, *i.e.* to dissociate a meson into a quark and an antiquark, a tube of gauge field forms between the two sources. In a non-Abelian gauge theory with sufficiently strong coupling this tube has a fixed radius and energy density, so the energy cost of separating color sources grows proportionally to the separation. A force law of this type can consistently be weak at short distances and strong at long distances, accounting for the fact that isolated quarks are not observed. An interesting description of confinement from a topological point of view can be found in [6].

2.4.3 Thresholds at quark masses

We now consider the case of a heavy quark with mass m much greater than the relevant scale Q . In this case it can be shown that the effects of the heavy quark on cross sections are suppressed by inverse powers of m and can therefore be ignored for $m \ll Q$ [7].

In the $\overline{\text{MS}}$ renormalization scheme α_s depends only on the renormalization scale. As a consequence heavy quarks contributions to the running of α_s must be taken into account even when we compute a physical quantity at an energy lower than the heavy quark mass scale. However, logarithms of large masses induced by the renormalization group equations in the couplings are canceled against other logarithms that appear in the calculation of physical observables. This is obviously an inconvenient, since a lot of effort must be invested in intermediate stages of a calculation to compute terms that will cancel in physical quantities.

To remedy this problem the standard procedure has been the use of the effective field theory language. For example, in QCD with a heavy quark and $n_f - 1$ light quarks, one builds a theory with n_f quarks and an effective field theory with $n_f - 1$ quarks. Around the threshold of the heavy quark we require agreement of the two theories. This gives a set of matching equations that relate the couplings of the theory with n_f quarks with the couplings of the theory with $n_f - 1$ quarks. This way, below the heavy quark threshold one can work with the effective theory, but using effective couplings. Then, by construction, decoupling is trivial. This procedure is equivalent to other renormalization schemes and allows us to correctly obtain the asymptotic value of the coupling constant. The price one has to pay is that coupling constants might not be continuous at thresholds. However, the fact that one has to use appropriate matching conditions in passing thresholds has been frequently kept into account in the running of the QCD coupling constant by just taking a continuous coupling constant across thresholds. Then, the final results depend strongly on the exact scale one uses to connect the couplings. To solve this ambiguity we can vary the matching scale μ_{th} between 1/2 and 2 times the mass of the heavy quark. It can be shown [8] that when appropriate matching conditions are taken into account the final answer does not depend on the exact μ_{th} used to connect the couplings.

As an example, we take eq. (2.4.7) at LLA and we require that $\alpha_s(Q^2)$ should be continuous at $Q^2 = \mu_{th}^2 = k_{th} m^2$, with m the heavy quark mass

$$\frac{1}{\alpha_+(Q^2)} - b_+ t = \frac{1}{\alpha_-(Q^2)} - b_- t, \quad t = \log \frac{Q^2}{\mu_{th}^2} \quad (2.4.19)$$

where index $+$ and $-$ refers to variables above and below the threshold. It

follows that

$$\frac{1}{\alpha_+(Q^2)} = \frac{1}{\alpha_-(Q^2)} + (b_+ - b_-) t = \frac{1 + \alpha_-(Q^2)(b_+ - b_-) t}{\alpha_-(Q^2)}. \quad (2.4.20)$$

Finally, we get

$$\begin{aligned} \alpha_+(Q^2) &= \frac{\alpha_-(Q^2)}{1 + \alpha_-(Q^2)(b_+ - b_-) t} = \frac{\alpha_-(Q^2)}{1 - \frac{\alpha_-(Q^2)}{6\pi} \log \frac{Q^2}{\mu_{th}^2}} \\ &\simeq \alpha_-(Q^2) \left(1 + \frac{\alpha_-(Q^2)}{6\pi} \log \frac{Q^2}{\mu_{th}^2} \right). \end{aligned} \quad (2.4.21)$$

The generalized version can be written as

$$\alpha_+(Q^2) = \alpha_-(Q^2) + \sum_{k=1}^{\infty} C_k \left(\log \frac{Q^2}{\mu_{th}^2} \right) \alpha_-^{k+1}(Q^2) \quad (2.4.22)$$

where

$$C_1(x) = \frac{1}{6\pi} x \quad (2.4.23)$$

Let now $\alpha_s(Q^2, n_f)$ be the solution of eq. (2.4.7) at LLA with $\Lambda = \Lambda_5$ and fixed n_f and let $\alpha_{s(n_f)}$ be the value of the coupling constant at a given n_f . Eq. (2.4.21) can be written as (see *e.g.* [9])

$$\begin{aligned} \alpha_{s(6)}^{-1}(Q^2) &= \alpha_s^{-1}(Q^2, 6) + C_{65}, \\ \alpha_{s(5)}(Q^2) &= \alpha_s(Q^2, 5), \\ \alpha_{s(4)}^{-1}(Q^2) &= \alpha_s^{-1}(Q^2, 4) + C_{45}, \\ \alpha_{s(3)}^{-1}(Q^2) &= \alpha_s^{-1}(Q^2, 3) + C_{34} + C_{45}, \end{aligned} \quad (2.4.24)$$

where

$$\begin{aligned} C_{65} &= \alpha_s^{-1}(m_t^2, 5) - \alpha_s^{-1}(m_t^2, 6), \\ C_{45} &= \alpha_s^{-1}(m_b^2, 5) - \alpha_s^{-1}(m_b^2, 4), \\ C_{34} &= \alpha_s^{-1}(m_c^2, 4) - \alpha_s^{-1}(m_c^2, 3), \end{aligned} \quad (2.4.25)$$

and we have set $\mu_{qth} = m_q$ for simplicity. As an example, we consider

$$\begin{aligned} &\alpha_{s(5)}(Q^2) - \alpha_{s(4)}(Q^2) = \\ &= \alpha_{s(5)}(Q^2) - \frac{\alpha_s(Q^2, 4)}{1 + \alpha_s(Q^2, 4) \frac{\alpha_s(m_b^2, 5) - \alpha_s(m_b^2, 4)}{\alpha_s(m_b^2, 5)\alpha_s(m_b^2, 4)}} \\ &\simeq \alpha_s(Q^2, 5) - \alpha_s(Q^2, 4) + \alpha_s(Q^2, 4)\alpha_s(Q^2, 5) \frac{\alpha_s(m_b^2, 5) - \alpha_s(m_b^2, 4)}{\alpha_s(m_b^2, 5)\alpha_s(m_b^2, 4)} \\ &\simeq (b_5 - b_4)\alpha_s^2(Q^2, 4) \log \frac{Q^2}{m_b^2}. \end{aligned} \quad (2.4.26)$$

This expression coincides with eq. (2.4.21) with $\alpha_{s(5)}(Q^2) = \alpha_+(Q^2)$ and $\alpha_{s(4)}(Q^2) = \alpha_-(Q^2)$. Note that eqs. (2.4.24) and (2.4.25) hold even at NLA.

To conclude we observe that, at each threshold also Λ_{n_f} changes. We now fix $\Lambda = \Lambda_5$ and we will show how different values of Λ for different n_f are related to each other. If we consider the NLA definition of Λ , we have

$$\Lambda = \frac{Q}{t/2} = Q \exp \left[-\frac{1}{2} \left(\frac{1}{b\alpha_s(Q^2)} + \frac{b'}{b} \log b' \alpha_s(Q^2) \right) \right]. \quad (2.4.27)$$

If we require that $\alpha_s(Q^2)$ given by is continuous at a threshold (we consider as an example $Q = m_b$)

$$b_4 \log \frac{m_b^2}{\Lambda_4^2} + b'_4 \log \log \frac{m_b^2}{\Lambda_4^2} = b_5 \log \frac{m_b^2}{\Lambda_5^2} + b'_5 \log \log \frac{m_b^2}{\Lambda_5^2}, \quad (2.4.28)$$

we find

$$\log \left[\Lambda_5^{-2b_5} \Lambda_5^{2b_4} m_b^{2(b_5-b_4)} \right] = \log \left[\left(\log \frac{m_b^2}{\Lambda_5^2} \right)^{-b'_5} \left(\log \frac{m_b^2}{\Lambda_4^2} \right)^{b'_4} \right], \quad (2.4.29)$$

and

$$\begin{aligned} \Lambda_4^{2b_4} &= \Lambda_5^{2b_5} m_b^{-2(b_5-b_4)} \left(\log \frac{m_b^2}{\Lambda_5^2} \right)^{-b'_5} \left(\log \frac{m_b^2}{\Lambda_4^2} \right)^{b'_4} \\ &\simeq \Lambda_5^{2b_5} m_b^{-2(b_5-b_4)} \left(\log \frac{m_b^2}{\Lambda_5^2} \right)^{-b'_5+b'_4}; \end{aligned} \quad (2.4.30)$$

it follows that [10]

$$\begin{aligned} \Lambda_4 &= \Lambda_5 \left(\frac{\Lambda_5}{m_b} \right)^{\frac{b_5-b_4}{b_4}} \left[\log \frac{m_b^2}{\Lambda_5^2} \right]^{-\frac{b'_5-b'_4}{2b_4}} \\ &= \Lambda_5 \left(\frac{m_b}{\Lambda_5} \right)^{\frac{2}{25}} \left[\log \frac{m_b^2}{\Lambda_5^2} \right]^{\frac{963}{14375}}. \end{aligned} \quad (2.4.31)$$

3

QCD and the parton model

Deep inelastic scattering (DIS) has been the process that established the first evidence of partons, and it is the traditional testing ground of perturbative QCD. Nowadays, it is no longer the correctness of the theory which come into question. Rather, the focus is shifted on the precise determinations of the unknown parameters, and the development of reliable computational techniques. The parameters to be determined include not only the strong coupling α_s , but also all quantities determined from the non-perturbative low-energy dynamics, and that, even though in principle computable, must be treated as phenomenological input in the perturbative domain.

In this Chapter we will briefly discuss deep inelastic scattering and the “naive parton model”. Then we will show how QCD modifies the simple Bjorken scaling property of the parton model, and discuss how these scaling violations can be calculated in perturbation theory. We will also discuss issues useful for the following Chapters, as the factorization schemes.

3.1 Deep inelastic scattering and the parton model

We now consider the scattering of a high-energy charged lepton, say, an electron, off a hadron target as shown in Fig. 3.1. If we label the incoming and outgoing lepton four-momenta by k^μ and k'^μ respectively, the momentum of the target hadron (assumed henceforth to be a proton) by p^μ and the momentum transfer by $q^\mu = k^\mu - k'^\mu$, then the standard deep inelastic variables are defined by

$$\begin{aligned} Q^2 &= -q^2 \\ M^2 &= p^2 \\ \nu &= p \cdot q = M(E' - E) \\ x &= \frac{Q^2}{2\nu} = \frac{Q^2}{2M(E' - E)} \end{aligned} \tag{3.1.1}$$

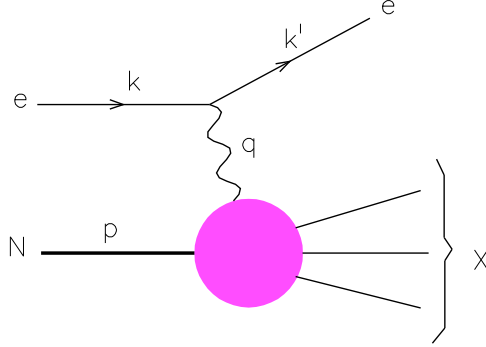


Figure 3.1. *Deep inelastic charged lepton-proton scattering.*

$$y = \frac{q \cdot p}{k \cdot p} = 1 - \frac{E'}{E},$$

where the energy variables refer to the target rest frame and M is the proton mass. Henceforth we will consider only charged lepton scattering, $lp \rightarrow lX$, for $Q^2 \ll M_Z^2$, where the scattering is mediated by the exchange of a virtual photon. A review on deep inelastic neutrino scattering can be found *e.g.* in Ref. [11].

The DIS cross section is given by

$$\begin{aligned} \frac{d^2\sigma}{dx dy} &= \frac{8\pi\alpha^2 ME}{Q^4} \left[\frac{1 + (1-y)^2}{2} 2xF_1 \right. \\ &\quad \left. + (1-y)(F_2 - 2xF_1) - \frac{M}{2E} xyF_2 \right], \end{aligned} \quad (3.1.2)$$

where $F_i(x, Q^2)$ are the nucleon structure functions which carry the information on the structure of the target as seen by the virtual photon. The *Bjorken limit* is defined as $Q^2, \nu \rightarrow \infty$ with x fixed. In this limit the structure functions are observed to obey an approximate *scaling law* [12, 13], *i.e.* they depend only on the dimensionless variable x :

$$F_i(x, Q^2) \rightarrow F_i(x). \quad (3.1.3)$$

Bjorken scaling implies that the virtual photon scatters off *point-like constituents*, since otherwise the dimensionless structure functions would depend on the ratio Q/Q_0 , with $1/Q_0$ some length scale characterizing the size of constituents. The parton model picture of deep inelastic scattering is most easily formulated in the “infinite momentum frame” in which the proton is moving very fast, $p^\mu \approx (P, 0, 0, P)$ with $P \gg M$. In this frame, we can consider a simple model where the photon scatters off a point-like quark constituent which is moving parallel with the proton and carrying a fraction ξ of

its momentum, *i.e.* $p_q^\mu = \xi p^\mu$. Neglecting the proton mass M , we can write eq. (3.1.2) as

$$\frac{d^2\sigma}{dx dQ^2} = \frac{4\pi\alpha^2}{Q^4} \left[[1 + (1-y)^2] F_1 + \frac{1-y}{x} (F_2 - 2xF_1) \right]. \quad (3.1.4)$$

In terms of the usual Mandelstam variables

$$\begin{aligned} \hat{s} &= (k + p_q)^2 = \frac{\xi Q^2}{xy}, \\ \hat{t} &= (k - k')^2 = -Q^2, \\ \hat{u} &= (p_q - k')^2 = \hat{s}(y-1), \end{aligned} \quad (3.1.5)$$

the matrix element squared for the amplitude of the process

$$l(k) + q(p_q) \rightarrow l(k') + q(p'_q) \quad (3.1.6)$$

is given by

$$\overline{\sum} |\mathcal{M}|^2 = 2e_q^2 e^4 \frac{\hat{s}^2 + \hat{u}^2}{\hat{t}^2}. \quad (3.1.7)$$

The notation $\overline{\sum}$ denotes the average (sum) over initial (final) colors and spins. Using the standard result for massless $2 \rightarrow 2$ scattering,

$$\frac{d\hat{\sigma}}{d\hat{t}} = \frac{1}{16\pi\hat{s}^2} \overline{\sum} |\mathcal{M}|^2, \quad (3.1.8)$$

and substituting for the kinematic variables in the matrix element squared, gives

$$\frac{d\hat{\sigma}}{dQ^2} = \frac{2\pi\alpha^2 e_q^2}{Q^4} [1 + (1-y)^2]. \quad (3.1.9)$$

The mass-shell constraint for the outgoing quark,

$$p'_q{}^2 = (p_q + q)^2 = q^2 + 2p_q \cdot q = -2p \cdot q(x - \xi) = 0, \quad (3.1.10)$$

implies $\xi = x$. By writing $\int_0^1 dx \delta(x - \xi) = 1$, we obtain the double differential cross section for the quark scattering process:

$$\frac{d\hat{\sigma}}{dx dQ^2} = \frac{4\pi\alpha^2}{Q^4} [1 + (1-y)^2] \frac{1}{2} e_q^2 \delta(x - \xi). \quad (3.1.11)$$

By comparing eqs. (3.1.4) and (3.1.11) we get that the structure functions in this simple model are

$$\hat{F}_2 = x e_q^2 \delta(x - \xi) = 2x \hat{F}_1. \quad (3.1.12)$$

This result suggests that the structure function $F_2(x)$ “probes” a quark constituent with momentum fraction $\xi = x$.

The above ideas are incorporated in what is known as the “naive parton model” [13]:

- $q(\xi)d\xi$ represents the probability that a quark q carries a momentum fraction between ξ and $\xi + d\xi$, where $0 \leq \xi \leq 1$;
- the virtual photon scatters incoherently off the quark constituents.

Thus the proton structure functions are obtained by weighting the quark structure functions with the probability distribution $q(\xi)$,

$$\begin{aligned}
 F_2 = 2xF_1 &= \sum_{q,\bar{q}} \int_0^1 d\xi q(\xi) x e_q^2 \delta(x - \xi) \\
 &= \sum_{q,\bar{q}} e_q^2 x q(x).
 \end{aligned}
 \tag{3.1.13}$$

The *l.h.s.* of eq. (3.1.13) is the *Callan-Gross relation* [14]) and it is a direct consequence of the spin- $\frac{1}{2}$ property of the quarks. Indeed, we observe that the two terms in the square brackets on the *r.h.s.* of eq. (3.1.4) correspond to the absorption of transversely (F_1) and longitudinally ($F_L \rightarrow F_2 - 2xF_1$ in the Bjorken limit) polarized virtual photon. The Callan-Gross relation follows from the fact that a spin- $\frac{1}{2}$ quark cannot absorb a longitudinally polarized vector boson. In contrast, spin-0 (scalar) quarks cannot absorb transversely polarized vector bosons and so would have $F_1 = 0$, *i.e.* $F_L = F_2$. Structure function measurements show that $F_L \ll F_2$, confirming that spin- $\frac{1}{2}$ property of quarks. Note that in the QCD-improved parton model F_L is only non-zero at leading order in perturbation theory, *i.e.* $F_L = O(\alpha_s)$.

3.2 Factorization

Factorization allows scattering amplitudes with incoming high-energy hadrons to be written as a product of a hard scattering piece and a reminder factor which carries the information on the physics at low-energies and momenta. The first term contains only high-energy and momentum components, and, because of asymptotic freedom, it is calculable in perturbation theory. The second term describes the non-perturbative physics, and it is given by a single process-independent function for each type of parton called the *parton distribution function* (PDF). Factorization is an essential tool as it ensures that a parton distribution measured in one process can be used in any other hard process. A detailed discussion of factorization is beyond the aim of this thesis, hence only a brief description will be given.

In the naive parton model, when terms down by powers of $1/Q^2$ are neglected, the DIS cross section eq. (3.1.4) can be obtained by the convolution of the distribution of a quark parton in the target, with fraction y of the target longitudinal momentum, with the point-like cross section for quark-current scattering

$$d\sigma_{eN} = \sum_{q=1}^{n_f} q_q^{(0)} \otimes d\sigma_{eq}^{(0)}, \quad (3.2.1)$$

where the index 0 stands for quantities calculated without taking into account strong interactions and the convolution with respect to x is defined as

$$(f \otimes g)(x) = \int_x^1 \frac{dy}{y} f(y) g\left(\frac{x}{y}\right). \quad (3.2.2)$$

The qualitative observation that hadrons emerge with a transverse momentum k_T different from zero can be explained with the presence of gluon emission. In a parton model without gluons, all final-state jets would be collinear with the virtual photon. Their hadron fragments will therefore be nearly collinear with the photon, that is, with a spread of k_T of about 300 MeV as required by the uncertainty principle for confined quarks. The data clearly establish an excess of large k_T hadrons which are the fragments of the quark and gluon jets recoiling against one another.

We will now we consider QCD corrections to eq. (3.2.1) at the first order of the perturbative expansion in α_s . In calculating these partonic cross sections we encounter divergences. These divergences are

- *collinear*, if a massless parton radiates a collinear massless parton whose momentum is proportional to that of the emitting parton;
- *soft*, if a parton emits or absorbs a massless parton with zero energy.

When we sum the virtual contributions to the cross section given by diagrams in Fig. 3.2 a,b and the real contributions given by diagrams in Fig. 3.2 c,d, we obtain that soft singularities are canceled. We are then left with the only contribution of collinear divergences that is proportional to

$$\frac{\alpha_s}{2\pi} \log \frac{Q^2}{\mu^2}, \quad (3.2.3)$$

where μ^2 is an arbitrary scale. If we take the initial parton, for instance, equal to a quark, the cross section can be written as

$$\begin{aligned} d\sigma &= q^{(0)} \otimes \left[d\sigma_q^{(0)} + \frac{\alpha_s}{2\pi} d\sigma_q^{(1)} \log \frac{Q^2}{\mu^2} + \frac{\alpha_s}{2\pi} d\hat{\sigma}_q^{(1)} \right] \\ &+ g^{(0)} \otimes \left[\frac{\alpha_s}{2\pi} d\sigma_g^{(1)} \log \frac{Q^2}{\mu^2} + \frac{\alpha_s}{2\pi} d\hat{\sigma}_g^{(1)} \right] \end{aligned} \quad (3.2.4)$$

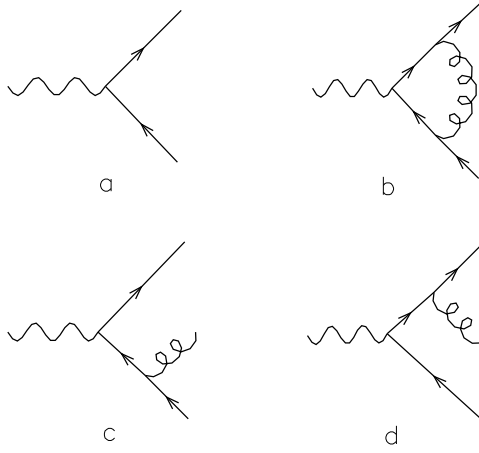


Figure 3.2. *Diagrams giving corrections of order α_s to the point-like quark-current cross sections.*

where we have neglected the sum over the flavors. It can be shown by direct calculation that

$$d\sigma_q^{(1)} = P_{qq} \otimes d\sigma_q^{(0)}, \tag{3.2.5}$$

$$d\sigma_g^{(1)} = P_{qg} \otimes d\sigma_g^{(0)}.$$

where $d\sigma_i^{(0)}$ are the Born cross sections and P_{ij} are process independent quantities that will be discussed in more detail later. The cross sections $d\hat{\sigma}_i$ are regular. Eq. (3.2.5) is very important as it allows to factorize the Born cross section $d\sigma^{(0)}$ and redefine the PDF including in this redefinition the contributions of the collinear divergences. We define

$$\begin{aligned} q(x, Q^2) &= q^{(0)} \otimes \left[\delta(1-x) + \frac{\alpha_s}{2\pi} P_{qq} \log \frac{Q^2}{\mu^2} \right] + g^{(0)} \otimes \frac{\alpha_s}{2\pi} P_{qg} \log \frac{Q^2}{\mu^2} \\ g(x, Q^2) &= g^{(0)}(x) + O(\alpha_s). \end{aligned} \tag{3.2.6}$$

We can proceed in the same way when we have a gluon in the initial state. Thus, we have

$$\begin{aligned} q(x, Q^2) &= \left[\delta(1-x) + \frac{\alpha_s}{2\pi} P_{qq} \log \frac{Q^2}{\mu^2} \right] \otimes q^{(0)} + \frac{\alpha_s}{2\pi} P_{qg} \log \frac{Q^2}{\mu^2} \otimes g^{(0)}, \\ g(x, Q^2) &= \frac{\alpha_s}{2\pi} P_{gq} \log \frac{Q^2}{\mu^2} \otimes q^{(0)} + \left[\delta(1-x) + \frac{\alpha_s}{2\pi} P_{gg} \log \frac{Q^2}{\mu^2} \right] \otimes g^{(0)}. \end{aligned} \tag{3.2.7}$$

In a matrix form we have

$$\begin{pmatrix} q^{(0)} \\ g^{(0)} \end{pmatrix} = Z \otimes \begin{pmatrix} q \\ g \end{pmatrix} \quad (3.2.8)$$

with

$$Z = I - \frac{\alpha_s}{2\pi} \log \frac{Q^2}{\mu^2} \begin{pmatrix} P_{qq} & P_{qg} \\ P_{gq} & P_{gg} \end{pmatrix} + O(\alpha_s^2), \quad (3.2.9)$$

where $q^{(0)}$ and $g^{(0)}$ are the divergent scale independent distributions, while q and g are the renormalized scale dependent distributions.

We can picture the redefinition of PDFs as follows. As Q^2 is increased to $Q^2 \sim Q_0^2$ where Q_0^2 is some scale characterizing the process, say, the photon starts to “see” evidence for the point-like valence quarks within the proton. If the quarks were non-interacting, no further structure would be resolved increasing Q^2 : scaling would set in, and the naive parton model would be satisfactory. However, QCD predicts that on increasing the resolution ($Q^2 \gg Q_0^2$), we should see that each quark is itself surrounded by a cloud of partons. The number of resolved partons which share the proton’s momentum increases with Q^2 .

The scale μ^2 is not physical, being introduced arbitrarily in the collinear divergences subtraction. Varying μ^2 we have a corresponding variation in the cross section at the order α_s . As a variation of α_s gives a contribution of order α_s^2 , these correction are negligible. If we had the whole series in α_s , all the terms proportional to μ^2 would cancel each other and we would not have any dependence on μ^2 . Thus, the μ^2 dependence is a consequence of the truncation of the perturbative expansion. Usually, we assign μ^2 a value of the order of the process energy scale, as to avoid large logarithm to appear. In the DIS case we choose $\mu^2 \simeq Q^2$.

3.2.1 Coefficient functions

With the redefinition of PDFs given in eq. (3.2.7), the cross section in eq. (3.2.4) can be written as

$$\begin{aligned} d\sigma(x, Q^2) &= q(x, Q^2) \otimes \left[d\sigma_q^{(0)} + \frac{\alpha_s}{2\pi} d\hat{\sigma}_q^{(1)} \right] + g(x, Q^2) \otimes \frac{\alpha_s}{2\pi} d\hat{\sigma}_g^{(1)} \\ &= \mathcal{C}^q(x) \otimes q(x, Q^2) + \mathcal{C}^g(x) \otimes g(x, Q^2), \end{aligned} \quad (3.2.10)$$

where $\mathcal{C}^{q,g}$ are the coefficient functions that contain the finite part of the partonic cross section. The structure function F_2 is given by

$$\begin{aligned} F_2(x, Q^2) &= x \int_x^1 \frac{dy}{y} \left\{ \sum_{q=1}^{n_f} e_q^2 q_q(y, Q^2) \left[\delta \left(\frac{x}{y} - 1 \right) + \frac{\alpha_s}{2\pi} d\hat{\sigma}_q^{(1)}(x) \right] \right. \\ &\quad \left. + 2n_f g(y, Q^2) \frac{\alpha_s}{2\pi} d\hat{\sigma}_g^{(1)}(x) \right\} \end{aligned} \quad (3.2.11)$$

where we have used the fact that $d\sigma_q^{(0)}(x) = \delta(1-x)$. In the $\overline{\text{MS}}$ scheme the NLO contributions to the coefficient functions are given by [15]

$$\begin{aligned} d\hat{\sigma}_q^{(1)}(x) &= C^q(x) & (3.2.12) \\ &= C_F \left[2 \left(\frac{\log(1-x)}{1-x} \right)_+ - \frac{3}{2} \left(\frac{1}{1-x} \right)_+ - (1+x) \log(1-x) \right. \\ &\quad \left. - \frac{1+x^2}{1-x} \log x + 3 + 2x - \left(\frac{\pi^2}{3} + \frac{9}{2} \right) \delta(1-x) \right], \end{aligned}$$

$$\begin{aligned} d\hat{\sigma}_g^{(1)}(x) &= C^g(x) & (3.2.13) \\ &= T_R \left[((1-x^2) + x^2) \log \frac{1-x}{x} - 8x^2 + 8x - 1 \right]. \end{aligned}$$

The next-to-next-to-leading order (NNLO) contribution to coefficient functions have been calculated in [16]. The coefficient functions are process dependent quantities and can be computed from the Renormalization Group Equation approach to the Operator Product Expansion of two currents. They describe the deviation from the canonical behavior of free field theory.

3.3 Evolution equations

3.3.1 Scaling violations and the Altarelli-Parisi equations

The redefinition of parton distributions given in eq. (3.2.8), introduces a scale dependence, and the redefinition of parton distribution means that we have substituted the bare quarks and gluons with clouds of partons. This is right what it happens when we renormalize a coupling constant. We will now derive the analogue of the RGE for parton distribution. Thus we require the invariance of eq. (3.2.8) from the scale μ^2 ; we get

$$\frac{d}{dt} \begin{pmatrix} q \\ g \end{pmatrix} = \frac{\alpha_s}{2\pi} \begin{pmatrix} P_{qq} & P_{qg} \\ P_{gq} & P_{gg} \end{pmatrix} \otimes \begin{pmatrix} q \\ g \end{pmatrix} + O(\alpha_s^2) \quad (3.3.1)$$

where $t = \log \frac{Q^2}{\mu^2}$, which is the Altarelli-Parisi equation for the unpolarized case [17]. We can interpret this equation saying that a quark with momentum fraction x can be produced by another quark with a larger momentum fraction y which has emitted a gluon. The functions P_{ij} are the Altarelli-Parisi splitting functions. They are calculated perturbatively as power series in α_s . At the leading-order they have an attractive physical interpretation as the probabilities of finding a parton of type i in a parton of type j with a fraction x of the longitudinal momentum of the parent parton and a transverse

momentum squared much less than μ^2 . The interpretation as probabilities implies that the splitting functions are positive definite for $x < 1$, and satisfy the sum rules

$$\begin{aligned} \int_0^1 dx P_{qq}(x) &= 0, \\ \int_0^1 dx x [P_{qq}(x) + P_{gq}(x)] &= 0, \\ \int_0^1 dx x [2n_f P_{qg}(x) + P_{gg}(x)] &= 0. \end{aligned} \tag{3.3.2}$$

The leading-order [17] and the next-to-leading-order [18] contribution to the Altarelli-Parisi splitting functions have been calculated. Here we show only the LO contributions:

$$\begin{aligned} P_{qq}^{(0)}(x) &= C_F \left[\frac{(1+x^2)}{(1-x)_+} + \frac{3}{2} \delta(1-x) \right], \\ P_{qg}^{(0)}(x) &= T_R [x^2 + (1-x)^2], \end{aligned} \tag{3.3.3}$$

$$\begin{aligned} P_{gq}^{(0)}(x) &= C_F \left[\frac{1+(1-x)^2}{x} \right], \\ P_{gg}^{(0)}(x) &= 2N \left[\frac{x}{(1-x)_+} + \frac{1-x}{x} + x(1-x) \right] + \delta(1-x) \frac{(11N - 4n_f T_R)}{6}, \end{aligned}$$

where $1/(1-x)_+$ means:

$$\int_0^1 dx \frac{f(x)}{(1-x)_+} = \int_0^1 \frac{f(x) - f(1)}{1-x}. \tag{3.3.4}$$

In the general case in the Altarelli-Parisi equations we have a $(2n_f + 1)$ -dimension matrix in the space of quarks and gluons. However, not all parton distributions evolve independently and we can restrict ourselves to two case. We define the non-singlet and the singlet parton distributions as

$$q^{(NS)}(x, Q^2) = \sum_{i \neq j=1}^{n_f} (q_i(x, Q^2) - q_j(x, Q^2)), \tag{3.3.5}$$

$$\Sigma(x, Q^2) = \sum_{i=1}^{n_f} (q_i(x, Q^2) + \bar{q}_i(x, Q^2)), \tag{3.3.6}$$

where in the non-singlet distribution definition q_j may coincide with \bar{q}_i . Thus the analysis of the evolution is simplified. As the gluon emission is flavor independent, in the difference between two distributions the gluonic terms

cancel and the evolution of the non-singlet term is independent from the gluon term. We have

$$\frac{d}{dt}q^{(NS)} = \frac{\alpha_s(t)}{2\pi} [P_{qq} \otimes q^{(NS)}]. \quad (3.3.7)$$

In the singlet case we have a mixing between quarks and gluon in the evolution and the Altarelli-Parisi equation is given by

$$\frac{d}{dt} \begin{pmatrix} \Sigma \\ g \end{pmatrix} = \frac{\alpha_s(t)}{2\pi} \begin{pmatrix} P_{qq} & 2n_f P_{qg} \\ P_{gq} & P_{gg} \end{pmatrix} \otimes \begin{pmatrix} \Sigma \\ g \end{pmatrix}. \quad (3.3.8)$$

Note that the parton evolution is causal, *i.e.* known the parton distributions at an initial scale Q_0^2 , we know their values at an arbitrary value Q^2 . This provides to be an essential tool to fit experimental data.

3.3.2 Solution of the Altarelli-Parisi equations

There are different techniques to solve the Altarelli-Parisi equations. One can solve them by performing numerically the convolution integrals starting from input distributions obtained from data. This is particularly convenient if a simultaneous solution of all $2n_f + 1$ parton distributions is required, given a set of starting functions $q(x, Q_0^2)$ at some reference scale Q_0^2 . This approach is adopted *e.g.* in Monte Carlo simulations for parton branching processes [2]. A second way is the analytical solution of the evolution equations in the Mellin moment space, where the convolution products turn into ordinary ones. Mellin moments are defined by

$$f_n = \int_0^1 dx x^{n-1} f(x). \quad (3.3.9)$$

In this section, we find the general solution of the equation

$$\frac{d}{d\tau} q = C q, \quad (3.3.10)$$

where q is a vector with M components, and C is a generic $M \times M$ matrix. The usual QCD evolution equations are special cases of this equation in which $M \leq 2$. We will assume that C has a perturbative expansion in powers of a parameter $a(\tau)$:

$$C = C_0 + a(\tau)C_1 + \dots, \quad (3.3.11)$$

where

$$\frac{da(\tau)}{d\tau} = -b_0 a (1 + b_1 a + \dots), \quad (3.3.12)$$

and $b_0 = 2\pi b$ and $b_1 = 2\pi b_1$, with b and b' given in eqs. (2.4.4) and (2.4.5). For QCD applications

$$a = \frac{\alpha_s}{2\pi}; \quad \tau = \frac{1}{2\pi} \int_{t_0}^t dt' \alpha_s(t'), \quad (3.3.13)$$

with $t = \log(Q^2/\Lambda_{QCD}^2)$.

The solution of eq. (3.3.10) can be obtained perturbatively. Expanding q to order a ,

$$q = q^{(0)} + a q^{(1)}, \quad (3.3.14)$$

we find

$$\frac{d}{d\tau} q^{(0)} = C_0 q^{(0)}, \quad (3.3.15)$$

$$\frac{d}{d\tau} q^{(1)} = (C_0 + b_0) q^{(1)} + C_1 q^{(0)}. \quad (3.3.16)$$

The solutions of eqs. (3.3.15) and (3.3.16) are

$$q^{(0)}(\tau) = R^{-1} e^{\gamma\tau} R q^{(0)}(0), \quad (3.3.17)$$

$$\begin{aligned} q^{(1)}(\tau) &= R^{-1} e^{(\gamma+b_0)\tau} R q^{(1)}(0) \\ &+ R^{-1} e^{(\gamma+b_0)\tau} \int_0^\tau d\sigma e^{-(\gamma+b_0)\sigma} \hat{C}_1 e^{\gamma\sigma} R q^{(0)}(0), \end{aligned} \quad (3.3.18)$$

where the matrix R diagonalizes C_0 ,

$$RC_0R^{-1} = \text{diag}(\gamma_1, \dots, \gamma_M) \equiv \gamma, \quad (3.3.19)$$

and

$$\hat{C}_1 = RC_1R^{-1}. \quad (3.3.20)$$

Collecting these results, and noting that $a \exp(b_0\tau) = a(0)$, up to terms of order a^2 , we can write the solution as

$$q(\tau) \equiv U(C, \tau)q(0) = R^{-1} \left[e^{\gamma\tau} + a e^{(\gamma+b_0)\tau} \int_0^\tau d\sigma e^{-(\gamma+b_0)\sigma} \hat{C}_1 e^{\gamma\sigma} \right] R q(0), \quad (3.3.21)$$

with the initial condition

$$q(0) = q^{(0)}(0) + a(0)q^{(1)}(0). \quad (3.3.22)$$

The explicit expression of $U(C, \tau)$ is

$$U_{ij}(C, \tau) = R_{im}^{-1} \left[\delta_{mn} e^{\gamma^n \tau} + a(\tau) \hat{C}_1^{mn} \frac{e^{\gamma^n \tau} - e^{(\gamma^m + b_0)\tau}}{\gamma^n - \gamma^m - b_0} \right] R_{nj}, \quad (3.3.23)$$

which, expanded to next-to-leading order reduces to

$$\begin{aligned}
 U_{ij}(C, \tau) &= R_{im}^{-1} \left\{ \delta_{mn} \left(\frac{a(0)}{a(\tau)} \right)^{\gamma_m/b_0} + \frac{\hat{C}_1^{mn} - b_1 \gamma_n \delta_{mn}}{\gamma^m - \gamma^n + b_0} \right. \\
 &\quad \left. \times \left[a(0) \left(\frac{a(0)}{a(\tau)} \right)^{\gamma_m/b_0} - a(\tau) \left(\frac{a(0)}{a(\tau)} \right)^{\gamma_m/b_0} \right] \right\} R_{nj} .
 \end{aligned} \tag{3.3.24}$$

In the case of standard QCD evolution equations the matrix C_0 is at most 2×2 and is easily diagonalized.

3.4 Factorization schemes

The way we subtract divergences is arbitrary. We may add a finite term of order α_s to Z defined in eq. (3.2.9), obtaining an infinity of choices, all equivalent to each other as it happens for ultraviolet renormalization schemes. Once we fix the finite term, a collinear subtraction scheme is defined.

If we sum over the number of flavors eq. (3.2.8) in the Mellin space, we can write the column vector as (here the index n is omitted to simplify the notation)

$$q^{(0)} = \begin{pmatrix} \Sigma^{(0)} \\ g^{(0)} \end{pmatrix}. \tag{3.4.1}$$

As the matrix Z is not uniquely defined up to term of order α_s , we can consider two transformations:

$$q^{(0)} = Zq = Z'q' \tag{3.4.2}$$

$$q' = Wq, \quad W = I + \frac{\alpha_s}{2\pi} E \tag{3.4.3}$$

where Z and Z' are 2×2 matrices. As q_0 is independent of the factorization scale μ we get

$$\frac{d}{dt} q^{(0)} = 0. \tag{3.4.4}$$

From the Altarelli-Parisi evolution equations we obtain

$$\frac{d}{dt} Zq + Z \frac{d}{dt} q = 0 \quad \rightarrow \quad \frac{d}{dt} q = \frac{\alpha_s}{2\pi} P = -Z^{-1} \frac{d}{dt} Zq \tag{3.4.5}$$

$$\frac{d}{dt} Z'q' + Z' \frac{d}{dt} q' = 0 \quad \rightarrow \quad \frac{d}{dt} q' = \frac{\alpha_s}{2\pi} P' = -Z'^{-1} \frac{d}{dt} Z'q' \tag{3.4.6}$$

If we perform a dimensional regularization, the Z -matrices can be written as

$$Z = I + \frac{\alpha_s}{2\pi} \frac{1}{\epsilon} \mathcal{Z} + O(\alpha_s^2) \quad (3.4.7)$$

$$Z' = I + \frac{\alpha_s}{2\pi} \frac{1}{\epsilon} \mathcal{Z}' + O(\alpha_s^2) = ZW^{-1} + O(\alpha_s^2). \quad (3.4.8)$$

We have

$$\frac{d}{dt} q' = -W Z^{-1} \left[\left(\frac{d}{dt} Z \right) W^{-1} + Z \left(\frac{d}{dt} W^{-1} \right) \right] q', \quad (3.4.9)$$

and

$$\frac{\alpha_s}{2\pi} P' = \frac{\alpha_s}{2\pi} W P W^{-1} - W \frac{d}{dt} W^{-1}, \quad (3.4.10)$$

with

$$\frac{d}{dt} W^{-1} = \frac{\alpha_s^2}{2\pi} b E + O(\alpha_s^2). \quad (3.4.11)$$

We obtain

$$P' = W P W^{-1} - \alpha_s b E + O(\alpha_s^2). \quad (3.4.12)$$

The substitution of W with its expansion (3.4.3) yields

$$\begin{aligned} P' &= \left(I + \frac{\alpha_s}{2\pi} E \right) P \left(I - \frac{\alpha_s}{2\pi} E \right) - b \alpha_s E \\ &= P + \frac{\alpha_s}{2\pi} [E, P] - \frac{\alpha_s}{2\pi} b_0 E. \end{aligned} \quad (3.4.13)$$

Expanding P in powers of α_s at NLO and comparing terms proportional to same powers of α_s , we finally obtain

$$P'^{(0)} = P^{(0)} \quad (3.4.14)$$

$$P'^{(1)} = P^{(1)} + [E, P^{(0)}] - b_0 E \quad (3.4.15)$$

3.4.1 The unpolarized case: $\overline{\text{MS}} \rightarrow \text{DIS}$

We will apply the results of the previous Section to the particular case in which the starting scheme is the $\overline{\text{MS}}$ and the final scheme is the DIS. We will write the $(n-1)^{\text{th}}$ moment of F_2 in both the schemes. Since F_2 is independent of the factorization scheme, comparing the two expressions we will find a transformation between the schemes.

In the $\overline{\text{MS}}$ scheme, the Mellin moment of eq. (3.2.11) with the definition of non-singlet and singlet PDFs given in eqs. (3.3.5) and (3.3.6), yields

$$\left(\frac{F_2}{x}\right)_n = C_n^q q_n^{NS} + \langle e^2 \rangle (C_n^q \Sigma_n + 2n_f C_n^g g_n), \quad (3.4.16)$$

where

$$C_n^q = I + \frac{\alpha_s}{2\pi} C_n^q \quad (3.4.17)$$

$$C_n^g = \frac{\alpha_s}{2\pi} C_n^g.$$

are the Mellin moments of the coefficient functions eqs. (3.2.12) and (3.2.13) and $\langle e^2 \rangle = \sum_{i=q,\bar{q}} e_i^2 / (2n_f)$. In a partonic scheme [19] we impose that the quark distribution is identified with F_2 (as it is in the parton model at LO) at any order in α_s

$$\left(\frac{F_2}{x}\right)_n = \sum_{q=1}^{nf} e_q^2 q'_{qn} = q_n'^{NS} + \langle e^2 \rangle \Sigma'_n. \quad (3.4.18)$$

If we take

$$E = \begin{bmatrix} E_{qq}(x) & 2n_f E_{qg}(x) \\ E_{gq}(x) & E_{gg}(x) \end{bmatrix}, \quad (3.4.19)$$

comparing the two expression of F_2 , we get

$$\begin{aligned} \left(I + \frac{\alpha_s}{2\pi} E_{NS}\right) q_n^{NS} + \left(I + \frac{\alpha_s}{2\pi} E_{qq}\right) \Sigma_n + 2n_f \frac{\alpha_s}{2\pi} E_{qg} g_n = \\ \left(I + \frac{\alpha_s}{2\pi} C_n^q\right) q_n^{NS} + \left(I + \frac{\alpha_s}{2\pi} C_n^q\right) \Sigma_n + 2n_f \frac{\alpha_s}{2\pi} C_n^g g_n. \end{aligned} \quad (3.4.20)$$

It follows

$$E = \begin{bmatrix} C_n^q & 2n_f C_n^g \\ E_{gq} & E_{gg} \end{bmatrix}. \quad (3.4.21)$$

and

$$E_{NS} = C_n^q. \quad (3.4.22)$$

The two other matrix elements of E specify completely the scheme. Here we will fix the scheme by assuming that all moments satisfy the relations between the parton-scheme gluon and the $\overline{\text{MS}}$ quark and gluons imposed by

momentum conservation on second moments [20, 21]¹. This is the prescription used in common parton sets, and usually referred to as DIS scheme. For $n = 2$ we have

$$\begin{aligned}
 & \int_0^1 dx x [P'_{qq}(1)(x) + P'_{gg}(1)(x)] = \\
 & \int_0^1 dx x [-b_0(E_{qq} + E_{gq}) - E_{gq}(2n_f P_{qq}^{(0)}(x) + P_{gg}^{(0)}(x)) + P_{gg}^{(0)}(x)(E_{gg} + \\
 & 2n_f E_{qg}) + E_{gq} P_{qq}^{(0)}(x) - E_{qq} P_{gq}^{(0)}(x) + P_{qq}^{(1)}(x) + P_{gq}^{(1)}(x)] = 0,
 \end{aligned} \tag{3.4.23}$$

$$\begin{aligned}
 & \int_0^1 dx x [2n_f P'_{qg}(1)(x) + P'_{gg}(1)(x)] = \\
 & \int_0^1 dx x [-b_0(2n_f E_{qg} + E_{gg}) - 2n_f E_{qg}(P_{qq}^{(0)}(x) + P_{gg}^{(0)}(x)) + \\
 & 2n_f E_{qg} P_{gg}^{(0)}(x) - 2n_f E_{gg} P_{qg}^{(0)}(x) + 2n_f P_{qg}^{(0)}(x)(E_{gq} + E_{qq}) \\
 & + 2n_f P_{qg}^{(1)}(x) + P_{gg}^{(1)}(x)] = 0,
 \end{aligned}$$

From eq. (3.3.3) we get

$$E_{gq} = -E_{qq} = -C_q^n \quad E_{gg} = -2n_f E_{qg} = -2n_f C_g^n. \tag{3.4.24}$$

Thus, generalizing for all n , we have

$$E^n = \begin{bmatrix} C_n^q & 2n_f C_n^g \\ -C_n^q & -2n_f C_n^g \end{bmatrix}. \tag{3.4.25}$$

¹ This condition is verified by the second moments of the NLO splitting functions in the $\overline{\text{MS}}$ scheme and fix their behavior at $x = 1$

4

Truncated Moments of parton distributions

In the previous Chapter we have introduced the Altarelli-Parisi equations which describe the evolution of parton distributions. As we have seen, we can solve the evolution equations analytically by taking their Mellin transform, which turns convolution products into ordinary ones, and therefore the x -space integro-differential equation into a set of independent ordinary first order differential equations. Usually, a parametrization of the parton distributions is assigned at some initial scale, and the parameters are then determined by fitting to data the evolved distributions. Mellin moments of structure functions, however, cannot be measured even indirectly, since they are defined as integrals over the whole range $0 \leq x \leq 1$, and thus require knowledge of the structure functions for arbitrarily small x , *i.e.* arbitrarily large energy $W^2 = \frac{Q^2(1-x)}{x}$.

We can solve this problem using the Altarelli-Parisi equation to evolve parton distributions directly: the scale dependence of any parton distribution at x_0 is then determined by knowledge of parton distributions for all $x > x_0$, *i.e.*, parton evolution is causal. In fact, through a judicious choice of factorization scheme [19, 21] all parton distributions can be identified with physical observables, and it is then possible to use the Altarelli-Parisi equations to express the scaling violations of structure functions entirely in terms of physically observable quantities. It is, however, hard to measure local scaling violations of structure functions in all the relevant processes: in practice, a detailed comparison with the data requires the solution of the evolution equations.

The frequently-adopted input on the x dependence of the parton distributions at the initial scale is for example [22]

$$q(x, Q_0^2) = a_0 x^{a_1} (1-x)^{a_2} P(x; , a_3, \dots),$$

where Q_0^2 is a reference scale. The parameter a_1 is associated with the small- x behavior while a_2 is associated with the large- x valence counting rules. The term $P(x; , a_3, \dots)$ is a suitably chosen smooth function, depending on one or more parameters, that adds more flexibility to the parton distributions parametrization. It has however become increasingly clear that in practice this procedure introduces a potentially large theoretical bias, whose size is very hard to assess [23]. In Ref. [24] it was proposed to adopt a functional method to keep this theoretical error under control. Another suitable way to minimize the bias introduced by the parton distributions parametrization is to project the parton distributions on an optimized basis of orthogonal functions. Different methods have been suggested with suitable families of orthogonal polynomials (*e.g.* Bernstein [25], Jacobi [26] or Laguerre polynomials [27]) as basis of function. A different approach has been suggested in Ref. [28], which makes use of truncated moments of parton distributions.

In this Chapter the technique of truncated moments will be extended from its original formulation for the non-singlet parton distributions to all flavor combinations, and we will show its numerical implementation.

In the following we will introduce the relevant evolution equations for truncated moments, and the corresponding solution. We will assess the accuracy of the method, and discuss techniques for phenomenological applications [29]. In the last Section, we will show how a numerical technique to increase the numerical efficiency of the method will provide to be a useful tool to solve the Altarelli-Parisi equation [30].

4.1 Evolution equations for truncated moments and their solutions

In Sect. 3.3.2 it has been described the solution of the Altarelli-Parisi equations eq. (3.3.1) by taking ordinary Mellin moments. Here, we are interested in the evolution of truncated moments, defined for a generic function $f(x)$ by

$$f_n(x_0) = \int_{x_0}^1 dx x^{n-1} f(x). \quad (4.1.1)$$

One finds immediately that the truncated moments of $q(x, Q^2)$ obey the equation

$$\frac{d}{d\tau} q_n(x_0, Q^2) = \int_{x_0}^1 dy y^{n-1} G_n \left(\frac{x_0}{y} \right) q(y, Q^2), \quad (4.1.2)$$

with τ given by eq. (3.3.13) and where

$$G_n(x) = \int_x^1 dz z^{n-1} P(z) \quad (4.1.3)$$

is perturbatively calculable as a power series in α_s .

Expanding $G_n(x_0/y)$ in powers of y around $y = 1$,

$$G_n\left(\frac{x_0}{y}\right) = \sum_{p=0}^{\infty} \frac{g_p^n(x_0)}{p!} (y-1)^p; \quad g_p^n(x_0) = \left[\frac{\partial^p}{\partial y^p} G_n\left(\frac{x_0}{y}\right) \right]_{y=1}, \quad (4.1.4)$$

one obtains

$$\frac{d}{d\tau} q_n(x_0, Q^2) = \sum_{p=0}^{\infty} \sum_{k=0}^p \frac{(-1)^{k+p} g_p^n(x_0)}{k!(p-k)!} q_{n+k}(x_0, Q^2). \quad (4.1.5)$$

The key step in the derivation of eq. (4.1.5) is the term-by-term integration of the series expansion. This is allowed, despite the fact that the radius of convergence of the series in eq. (4.1.4) is $1 - x_0$, because the singularity of $G_n(x_0/y)$ at $y = x_0$ is integrable (this can be proved [31] using the Lebesgue definition of the integral). One can then express each power of $(y - 1)$ using the binomial expansion, which leads to eq. (4.1.5).

Equation (4.1.5) expresses the fact that, while full moments of parton distributions evolve independently of each other, truncated moments obey a system of coupled evolution equations. In particular, the evolution of the n^{th} moment is determined by all the moments q_j , with $j \geq n$. In practice, the expansion in eq. (4.1.4), because of its convergence, can be truncated to a finite order $p = M$. The error associated with this procedure will be discussed in Sect. 4.2. In this case, eq. (4.1.5) can be rewritten as

$$\frac{d}{d\tau} q_n(x_0, Q^2) = \sum_{k=0}^M c_{nk}^{(M)}(x_0) q_{n+k}(x_0, Q^2), \quad (4.1.6)$$

where

$$c_{nk}^{(M)}(x_0) = \sum_{p=k}^M \frac{(-1)^{p+k} g_p^n(x_0)}{k!(p-k)!}. \quad (4.1.7)$$

To solve the system of equations (4.1.6), it is necessary to include a decreasing number of terms (M , $M - 1$, and so on) in the evolution equations for higher moments ($n + 1$, $n + 2$, ...), obtaining $M + 1$ equations for the $M + 1$ truncated moments $\{q_n, \dots, q_{n+M}\}$. We will see in the next Section that this approximation is fully justified. In this case, the coupled system of evolution equations takes the form

$$\frac{d}{d\tau} q_k = \sum_{l=n}^{n+M} C_{kl} q_l; \quad n \leq k \leq n + M, \quad (4.1.8)$$

where C is now a triangular matrix:

$$\begin{cases} C_{kl} = c_{k,l-k}^{(M-k+n)} & (l \geq k) , \\ C_{kl} = 0 & (l < k) . \end{cases} \quad (4.1.9)$$

In the non-singlet case, discussed in Ref. [28], the matrix elements C_{kl} are just numbers, and the matrix C in eq. (4.1.9) is triangular, which makes it easy to solve eq. (4.1.8) perturbatively. In the singlet case, each entry C_{kl} is a 2×2 matrix. As a consequence, the matrix C , which is given in terms of partial moments of the evolution kernels, is no longer triangular, but has non-vanishing 2×2 blocks along the diagonal.

Here, we will show how to solve the singlet case that easily reduce to the non-singlet case. By writing the perturbative expansion of C , we get

$$C = C_0 + aC_1 + \dots = (A_0 + B_0) + a(A_1 + B_1) + \dots, \quad (4.1.10)$$

where $A = A_0 + aA_1$ is block-diagonal, with 2×2 blocks on its diagonal,

$$A_{kl} = C_{kk}\delta_{kl}, \quad (4.1.11)$$

while $B = B_0 + aB_1$, considered as a matrix of 2×2 blocks, is upper-triangular with vanishing diagonal entries. Now one can define a matrix S that diagonalizes A_0 ,

$$SA_0S^{-1} = \text{diag}(\gamma_1, \dots, \gamma_{2M}). \quad (4.1.12)$$

Clearly, S is τ -independent, block-diagonal, and easily computed. Equation (4.1.8) can then be rewritten as

$$\frac{d}{d\tau} \tilde{q} = T \tilde{q}, \quad (4.1.13)$$

where $\tilde{q} = Sq$ and $T = SCS^{-1}$.

The new evolution matrix T is triangular at leading order (with the same eigenvalues as A_0). This is enough to solve the evolution equation to next-to-leading order. The general solution has been worked out in detail in Sect. 3.3.2; the result is

$$\tilde{q}(\tau) = U(T, \tau) \tilde{q}(0), \quad (4.1.14)$$

where

$$\begin{aligned} U_{ij}(T, \tau) &= R_{ik}^{-1} \left\{ \delta_{kl} \left(\frac{a(0)}{a(\tau)} \right)^{\gamma_l/b_0} \right. \\ &\quad \left. + \frac{\hat{T}_1^{kl} - b_1 \gamma_l \delta_{kl}}{\gamma_k - \gamma_l + b_0} \left[a(0) \left(\frac{a(0)}{a(\tau)} \right)^{\gamma_k/b_0} - a(\tau) \left(\frac{a(0)}{a(\tau)} \right)^{\gamma_l/b_0} \right] \right\} R_{lj}. \end{aligned} \quad (4.1.15)$$

In eqs. (4.1.14) and (4.1.15), T is expanded as $T = T_0 + aT_1$; R is the matrix which diagonalizes T_0 , $RT_0R^{-1} = \text{diag}(\gamma_1, \dots, \gamma_{2M})$; finally, $\hat{T}_1 = RT_1R^{-1}$.

The matrix R can be computed recursively, using the technique applied in Refs. [28, 29] and proved in Appendix A. One finds

$$R_{ij} = \frac{1}{\gamma_i - \gamma_j} \sum_{p=i}^{j-1} R_{ip} T_0^{pj}, \quad (4.1.16)$$

$$R_{ij}^{-1} = \frac{1}{\gamma_j - \gamma_i} \sum_{p=i+1}^j T_0^{ip} R_{pj}^{-1}, \quad (4.1.17)$$

which, together with the conditions $R_{ii} = 1$ and $R_{ij} = 0$ when $i > j$, determine the matrix R completely.

The general solution for the parton distributions is then

$$q(\tau) = U(C, \tau) q(0), \quad (4.1.18)$$

where

$$U(C, \tau) = S^{-1} U(T, \tau) S. \quad (4.1.19)$$

We have calculated the splitting functions and partial moment integrals which should be used in eq. (4.1.15) in order to compute this solution explicitly, and they are listed in Appendices C and D of Ref. [29].

For the sake of completeness, we describe a different method to solve eq. (4.1.6). It is immediate to check that the matrix

$$U(C, \tau) = I + \sum_{n=1}^{\infty} \int_0^{\tau} d\tau_1 \dots \int_0^{\tau_{n-1}} d\tau_n C(\tau_1) \dots C(\tau_n) \quad (4.1.20)$$

obeys the differential equation

$$\frac{d}{d\tau} U(C, \tau) = CU(C, \tau), \quad (4.1.21)$$

with the initial condition $U(C, 0) = I$. In general, eq. (4.1.20) is not very useful, since it involves an infinite sum. In the present case, however, the infinite sum collapses to a finite sum. To see this, consider again the decomposition $C = A + B$, where A is block-diagonal and B is upper-triangular. It is easy to prove that

$$U(C, \tau) = U(A, \tau) U(\tilde{B}, \tau), \quad (4.1.22)$$

where

$$\tilde{B} = U^{-1}(A, \tau) B U(A, \tau). \quad (4.1.23)$$

Since A is block diagonal, $U(A, \tau)$ is also block-diagonal, and it can be computed perturbatively using the procedure described in Sect. 3.3.2. Furthermore, once $U(A)$ is known, the upper-triangular matrix \tilde{B} can be computed through eq. (4.1.23). Now one can use the fact that upper-triangular matrices have the property that their M^{th} power vanishes. Hence, the solution can be expressed as the finite sum

$$U(\tilde{B}, \tau) = I + \sum_{n=1}^{M-1} \int_0^\tau d\tau_1 \dots \int_0^{\tau_{n-1}} d\tau_n \tilde{B}(\tau_1) \dots \tilde{B}(\tau_n), \quad (4.1.24)$$

and from the knowledge of $U(\tilde{B})$ and $U(A)$ one can determine the solution to the evolution equations explicitly.

4.2 Numerical methods and their accuracy

In this Section we will assess the accuracy of our method when the series of contributions to the right-hand side of the evolution equation (4.1.5) is approximated by retaining a finite number M of terms. The loss of accuracy due to this truncation is the price to pay for eliminating the dependence on parton parametrizations and extrapolations in the unmeasured region. However, unlike the latter uncertainties, which are difficult to estimate, the truncation uncertainty can be simply assessed by studying the convergence of the series. A reasonable goal, suitable for state-of-the-art phenomenology, is to reproduce the evolution equations to about 5% accuracy: indeed, we expect the uncertainties related to the parametrization of parton distributions in the conventional approach to be somewhat larger ($\sim 10\%$)¹. Notice that there is no obstacle to achieve a higher level of precision when necessary, by simply including more terms in the relevant expansions. To this level of accuracy it is enough to study the behavior of the leading order contribution to the evolution equation: indeed, next-to-leading corrections to the anomalous dimension are themselves of order 10%. We have verified explicitly that the inclusion of the next-to-leading corrections does not affect our conclusions.

We can compare the exact evolution equation (4.1.5) with its approximate form, eq. (4.1.6), by defining the percentage error on the right-hand side of the evolution equations for the quark non-singlet, singlet and gluon:

$$\mathcal{R}_{n,M}^{NS} = \frac{1}{\mathcal{N}_{NS}} \int_{x_0}^1 dy y^{n-1} \left[G_n^{NS} \left(\frac{x_0}{y} \right) - \sum_{k=0}^M y^k c_{nk}^{NS} \right] q^{NS}(y, Q^2), \quad (4.2.1)$$

¹Notice that this is *not* the uncertainty associated with evolution of a *given* parametrization with, say, an x -space code; rather, it is the uncertainty associated with the *choice* of the parametrization, and with the bias it introduces in the shape of the distribution.

$$\mathcal{R}_{n,M}^{\Sigma} = \frac{1}{\mathcal{N}_{\Sigma}} \int_{x_0}^1 dy y^{n-1} \left\{ \left[G_n^{qq} \left(\frac{x_0}{y} \right) - \sum_{k=0}^M y^k c_{nk}^{qq} \right] \Sigma(y, Q^2) \right. \\ \left. + \left[G_n^{gg} \left(\frac{x_0}{y} \right) - \sum_{k=0}^M y^k c_{nk}^{gg} \right] g(y, Q^2) \right\}, \quad (4.2.2)$$

$$\mathcal{R}_{n,M}^g = \frac{1}{\mathcal{N}_g} \int_{x_0}^1 dy y^{n-1} \left\{ \left[G_n^{gq} \left(\frac{x_0}{y} \right) - \sum_{k=0}^M y^k c_{nk}^{gq} \right] \Sigma(y, Q^2) \right. \\ \left. + \left[G_n^{gg} \left(\frac{x_0}{y} \right) - \sum_{k=0}^M y^k c_{nk}^{gg} \right] g(y, Q^2) \right\}, \quad (4.2.3)$$

where $\mathcal{N}_{NS,\Sigma,g}$ are the exact right-hand sides of the evolution equation (4.1.5). We study the dependence of the percentage error on the value of M for typical values of the cutoff x_0 and for representative choices of test parton distributions. In particular, we parametrize parton distributions as

$$q(x, Q^2) = a_0 x^{-a_1} (1-x)^{a_2}. \quad (4.2.4)$$

We begin by choosing, as a representative case, $a_2 = 4$ and $a_1 = 1$ for the singlet distributions and $a_1 = 0$ for the non-singlet. The non-singlet is assumed to behave qualitatively as $q_{NS} \sim xg \sim x\Sigma$, in accordance with the behavior of the respective splitting functions. Furthermore, the normalization factors a_0 for the singlet and gluon are fixed by requiring that the second moments of $\Sigma(x, Q^2)$ and $g(x, Q^2)$ are in the ratio 0.6/0.4, which is the approximate relative size of the quark and gluon momentum fractions at a scale of a few GeV². We will then show that changing the values of a_1 and a_2 within a physically reasonable range does not affect the qualitative features of our results.

The accuracy of the truncation of the evolution equation is determined by the convergence of the expansion in eq. (4.1.4). Because this expansion is centered at $y = 1$, and diverges at $y = x_0$, the small y region of the integration range in eq. (4.1.2) is poorly reproduced by the expansion. Hence, even though the series in eq. (4.1.5) converges, as discussed in Sect. 4.1, the convergence will be slower for low moments, which receive a larger contribution from the region of integration $y \sim x_0$. In fact, for low enough values of n , the convolution integral on the right-hand side of the evolution equation (4.1.2) does not exist: this happens for the same value for which the full moment of the structure function does not exist, *i.e.* $n \leq 1$ in the unpolarized singlet and $n \leq 0$ in the unpolarized non-singlet and in the polarized case. Therefore, we concentrate on the lowest existing integer moments of unpolarized distributions, *i.e.* the cases $n = 2, 3$ for the singlet distributions, and correspondingly $n = 1, 2$ for the non-singlet, which are the cases in which the accuracy of the truncation will be worse.

$x_0 = 0.1$						
M	$\mathcal{R}_{1,M}^{NS}$	$\mathcal{R}_{2,M}^{\Sigma}$	$\mathcal{R}_{2,M}^g$	$\mathcal{R}_{2,M}^{NS}$	$\mathcal{R}_{3,M}^{\Sigma}$	$\mathcal{R}_{3,M}^g$
5	0.63	0.43	0.55	0.16	0.12	0.16
10	0.49	0.36	0.38	0.13	0.10	0.12
20	0.34	0.27	0.26	0.10	0.08	0.08
40	0.20	0.17	0.17	0.06	0.05	0.05
70	0.12	0.10	0.10	0.04	0.03	0.03
100	0.09	0.07	0.07	0.03	0.02	0.02
150	0.06	0.05	0.05	0.02	0.01	0.01

Table 4.1. Values of $\mathcal{R}_{n,M}^{NS,\Sigma,g}$ for $x_0 = 0.1$ and different values of n and M .

$x_0 = 0.01$						
M	$\mathcal{R}_{1,M}^{NS}$	$\mathcal{R}_{2,M}^{\Sigma}$	$\mathcal{R}_{2,M}^g$	$\mathcal{R}_{2,M}^{NS}$	$\mathcal{R}_{3,M}^{\Sigma}$	$\mathcal{R}_{3,M}^g$
5	0.80	0.12	-42.81	0.0050	0.0024	0.0080
10	0.71	0.12	-34.67	0.0047	0.0024	0.0071
15	0.64	0.11	-29.23	0.0044	0.0024	0.0064
20	0.59	0.11	-25.28	0.0042	0.0023	0.0059

Table 4.2. Values of $\mathcal{R}_{N,M}^{\Sigma}$ and $\mathcal{R}_{N,M}^g$ for $x_0 = 0.01$ and different values of N and M .

The values of $\mathcal{R}_{n,M}^{NS,\Sigma,g}$, computed at leading order with $x_0 = 0.1$, are shown in Table 4.1.

The table shows that non-singlet moments of order n behave as singlet moments of order $n - 1$. This is a consequence of the fact that, as discussed above, the convergence of the expansion is determined by the singularity of the integrand $G_n(x_0/y)q(y)$ of eq. (4.1.2) as $y \rightarrow x_0$; near $y = x_0$, the function $G_n(x_0/y)$ is well approximated by the singular contribution $\log(1 - x_0/y)$, while parton distributions carry an extra power of y^{-1} in the singlet case in comparison to the non-singlet. We also observe in Table 4.1 that, as expected, the convergence is slower for the lowest moments, and rapidly improves as the order of the moment increases. This rapid improvement is a consequence of the fact that the convergence of the expansion of $G(x_0/y)$ is only slow in the immediate vicinity of the point $y = x_0$, and the contribution of this region to the n^{th} moment is suppressed by a factor of x_0^{n-1} . Due to this fast improvement, the approximation introduced by including one less term in the expansion as the order of the moment is increased by one, which is necessary to obtain the closed system of evolution equations (4.1.8), is certainly justified.

The 5% accuracy goal which we set to ourselves requires the inclusion of more than 100 terms for the lowest moment, but only about 40 terms for

the next-to-lowest. The computation of series with such a large number of contributions does not present any problem, since the splitting functions are known and their truncated moments are easily determined numerically. The implications of this requirement for phenomenology will be discussed in the next Section. We can now study the dependence of these results on the value of the truncation point x_0 by plotting the exact and approximate right-hand side of the evolution equations as a function of x_0 , as shown in Fig. 4.1.

The figures show that the case $x_0 = 0.1$ studied in Table 4.1 is a generic one between the two limiting (and physically uninteresting) cases $x_0 = 0$ and $x_0 = 1$, where the approximation is exact. In fact, with this particular choice of parton distributions, $x_0 = 0.1$ is essentially a worst case and the error estimates of Table 4.1 are therefore conservative.

An interesting feature of these plots is the presence of zeroes of the lowest moment evolution at $x_0 = 0$ in the non-singlet and around $x_0 \approx 10^{-2}$ in the gluon case. The physical origin of these zeroes is clear. At leading order, the first non-singlet full moment does not evolve. On the other hand, the second gluon full moment grows with Q^2 , while higher gluon full moments decrease, *i.e.* the gluon distribution decreases at large x ; this implies that the second truncated moment of the gluon must decrease for a high enough value of the cutoff x_0 , while it must increase for very small x_0 ; its derivative is thus bound to vanish at some intermediate point. Of course, the phenomenology of scaling violations (such as a determination of α_s) cannot be performed at or close to these zeroes, where there is no evolution. From the point of view of a truncated moment analysis, this means that the value of x_0 should be chosen with care in order to avoid these regions.

In Table 4.2 we show for sake of completeness values of $\mathcal{R}_{n,M}^{NS,\Sigma,g}$ for $x_0 = 0.01$. The large percentage errors on the first moment of the gluon are due to its zero value as it has been discussed above.

Finally, in Table 4.3 we study the dependence of our results on the form of the parton distributions, by varying the parameters a_1 and a_2 within a reasonable range. Of course, parton distributions which are more concentrated at small y give rise to slower convergence. However, we can safely conclude that the effect of varying the shape of parton distributions is generally rather small. We have also verified that varying the relative normalization of the quark and gluon distributions has a negligible effect on the convergence of the series, even though it may change by a moderate amount the position of the zeroes in gluon evolution discussed above.

4.3 Techniques for phenomenological applications

So far we have discussed scaling violations of parton distributions. In a generic factorization scheme, the measured structure functions are convo-

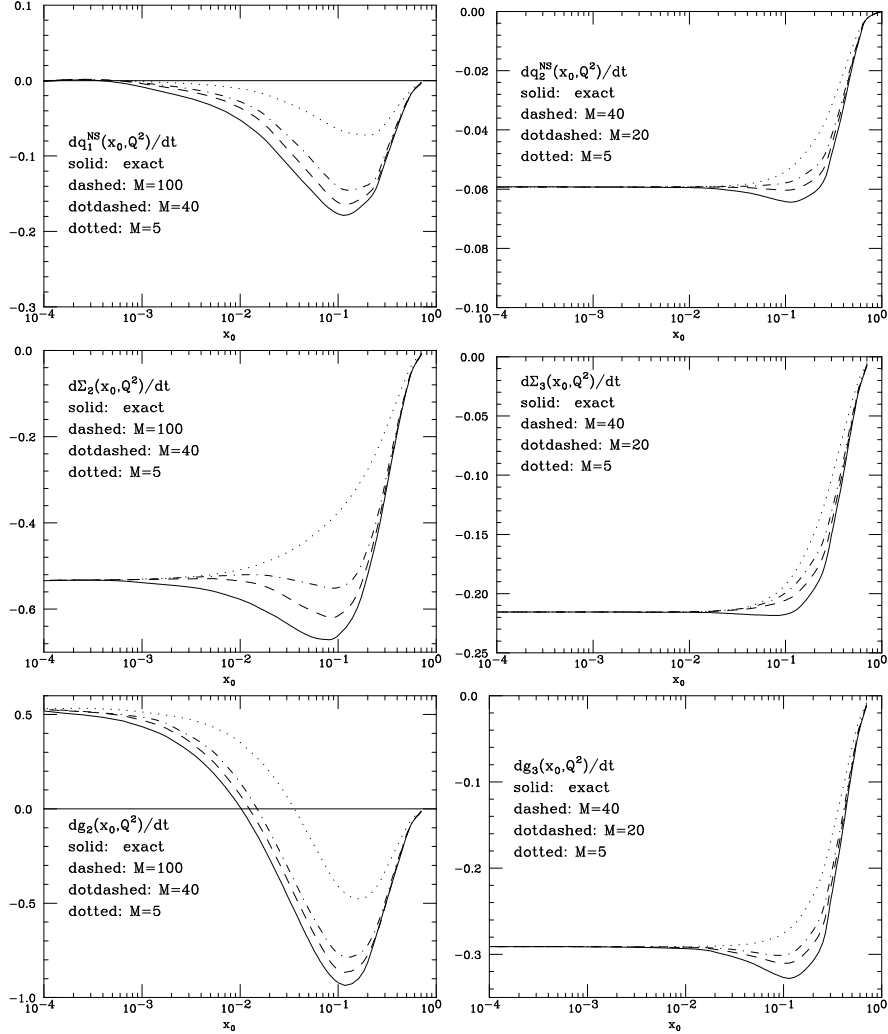


Figure 4.1. *Right-hand sides of the evolution equations for the first and second truncated moments of the non-singlet distribution, and for the second and third moments of singlet distributions. The overall scale is set by $\alpha_s(2\text{GeV}^2)$.*

lutions of parton distributions and coefficient functions. When taking moments, convolutions turn into ordinary products and moments of coefficient functions are identified with Wilson coefficients. In the present case, however, as shown in eqs. (4.1.2-4.1.5), truncated moments turn convolutions into products of triangular matrices. Hence, in a generic factorization scheme, truncated moments of parton distributions are related to truncated moments of structure functions by a further triangular matrix of truncated moments of coefficient functions.

This complication can be avoided by working in a parton scheme [19], where the quark distribution is identified with the structure function F_2 . This

$n = 2, x_0 = 0.1$					
a_1	a_2	$\mathcal{R}_{n,20}^\Sigma$	$\mathcal{R}_{n,70}^\Sigma$	$\mathcal{R}_{n,20}^g$	$\mathcal{R}_{n,70}^g$
1.5	2.0	0.26	0.10	0.27	0.11
1.0	2.0	0.20	0.07	0.23	0.09
0.5	2.0	0.14	0.05	0.18	0.07
1.5	4.0	0.32	0.12	0.30	0.12
1.0	4.0	0.27	0.10	0.26	0.10
0.5	4.0	0.22	0.08	0.22	0.09
1.5	6.0	0.36	0.14	0.32	0.14
1.0	6.0	0.32	0.12	0.29	0.12
0.5	6.0	0.27	0.10	0.26	0.10
$n = 3, x_0 = 0.1$					
1.5	2.0	0.07	0.03	0.07	0.03
1.0	2.0	0.04	0.02	0.04	0.02
0.5	2.0	0.02	0.01	0.02	0.01
1.5	4.0	0.12	0.05	0.11	0.05
1.0	4.0	0.08	0.03	0.08	0.03
0.5	4.0	0.05	0.02	0.05	0.02
1.5	6.0	0.16	0.07	0.15	0.06
1.0	6.0	0.12	0.05	0.12	0.05
0.5	6.0	0.09	0.03	0.08	0.03

Table 4.3. Values of $\mathcal{R}_{n,M}^\Sigma$ and $\mathcal{R}_{n,M}^g$ for $x_0 = 0.1$ and different choices of parton distribution parameters.

still does not fix the factorization scheme completely in the gluon sector. One way of fixing it is to use a “physical” scheme, where all parton distributions are identified with physical observables [21]. This may eventually prove the most convenient choice for the sake of precision phenomenology, once accurate data on all the relevant physical observables are available. At present, however, the gluon distribution is mostly determined from scaling violations of F_2 , so within the parton family of schemes the choice of gluon factorization is immaterial. Here we will fix the scheme by assuming that all moments satisfy the relations between the parton–scheme gluon and the $\overline{\text{MS}}$ quark and gluons imposed by momentum conservation on second moments [20]. This is the prescription used in common parton sets, and usually referred to as DIS scheme. The explicit expressions of Altarelli-Parisi kernels in the DIS scheme that we have evaluated are given in Appendix D of Ref. [29].

With this prescription, the phenomenology of scaling violations can be studied by computing a sufficiently large number of truncated moments of structure functions, so as to guarantee the required accuracy. If the aim is, for instance, a determination of α_s from non-singlet scaling violations, all

we need is a large enough number of truncated moments of the non-singlet structure function. Once an interpolation of the data in the measured region is available, the determination of such truncated moments is straightforward. This interpolation can be performed in an unbiased way using neural networks, as we will see in the following. One may wonder, however, whether the need to use the values of very high moments would not be a problem. Indeed, very high moments depend strongly on the behavior of the structure function at large y , which is experimentally known very poorly. Furthermore, it seems contradictory that scaling violations of the lowest moments should be most dependent on the structure function at large y .

This dependence is only apparent, however. Indeed, eq. (4.1.5) for, say, the non-singlet first moment can be rewritten as

$$\frac{d}{d\tau}q_1(x_0, Q^2) = \sum_{p=0}^{\infty} \frac{g_p^1(x_0)}{p!} \hat{q}_1^p(x_0, Q^2) , \quad (4.3.1)$$

where

$$\hat{q}_k^p(x_0, Q^2) = \int_{x_0}^1 dy y^{k-1} (y-1)^p q(y, Q^2) . \quad (4.3.2)$$

The need to include high orders in the expansion in eq. (4.1.6) is due to the slow convergence of the series in eq. (4.3.1), in turn determined by the fact that $G_n(x_0/y)$ diverges logarithmically at $y = x_0$. Correspondingly, the right-hand side of the evolution equation depends significantly on \hat{q}_1^p for large values of p , which signal a sensitivity to the value of $q(y, Q^2)$ in the neighborhood of the point $y = x_0$. The dependence on high truncated moments q_n is introduced when \hat{q}_1^p is re-expressed in terms of q_n , by expanding the binomial series for $(y-1)^p$. Since this re-expansion is exact, it cannot introduce a dependence on the large y region which is not there in the original expression. The high orders of the expansion do instead introduce a significant dependence on the value of the structure function in the neighborhood of x_0 , which can be kept under control provided x_0 is not too small, *i.e.* well into the measured region. There is therefore no obstacle even in practice in performing an accurate determination of α_s from scaling violations of truncated moments.

Let us now consider a second typical application of our method, namely the determination of truncated moments of the gluon distribution. In particular, the physically interesting case is the lowest integer moment, *i.e.* the momentum fraction in the unpolarized case or the spin fraction in the polarized case. The need to include a large number of terms in the expansion of the evolution equations seems to imply the need to introduce an equally large number of parameters, one for each gluon truncated moment. This would be problematic since it appears unrealistic to fit a very large number of parameters of the gluon from currently available data on scaling violations. We

may, however, take advantage of the fact that the dependence on high order truncated moments is fictitious, as we have just seen, and it rather indicates an enhanced sensitivity to the value of $q(y, Q^2)$ as $y \rightarrow x_0$. This suggests that a natural set of parameters to describe the gluon distribution should include the first several truncated moments, as well as further information on the behavior of the distribution around the truncation point x_0 , such as the value of the distribution (and possibly of some of its derivatives) at the point x_0 .

To understand how such a parametrization might work, notice that if $q(y, Q^2)$ is regular around $y = x_0$, then it is easy to prove that

$$\lim_{p \rightarrow \infty} \frac{\int_{x_0}^1 dy (y-1)^p q(y, Q^2)}{q(x_0, Q^2) \int_{x_0}^1 dy (y-1)^p} = 1, \quad (4.3.3)$$

by Taylor expanding $q(y)$ about $y = x_0$. We may therefore approximate the series which appears on the *r.h.s.* of eq. (4.3.1) by

$$\begin{aligned} S(x_0, n_0) &= \sum_{p=0}^{n_0-1} \frac{g_p^1(x_0)}{p!} \int_{x_0}^1 dy (y-1)^p q(y, Q^2) \\ &+ \sum_{p=n_0}^{\infty} \frac{g_p^1(x_0)}{p!} q(x_0, Q^2) \int_{x_0}^1 dy (y-1)^p. \end{aligned} \quad (4.3.4)$$

Equation (4.3.4) describes the evolution of the first truncated moment of $q(y, Q^2)$ in terms of the first n_0 truncated moments and of the value of $q(y)$ at the truncation point x_0 . Of course, the approximation gets better if n_0 increases. It is easy to check that when $x_0 = 0.1$ the accuracy is already better than 10% when $n_0 \sim 7$. This means that a parametrization of the distribution in terms of less than ten parameters is fully adequate. It is easy to convince oneself that this estimate is reliable, and essentially independent of the shape of the distribution $q(y, Q^2)$. In fact, because slow convergence arises due to the logarithmic singularity in $G_n(x_0/y)$, we can estimate the error of the approximation in eq. (4.3.4) by replacing the functions $g_p^1(x_0)/p!$ with the coefficients of the Taylor expansion of $\log(1 - x_0/y)$ in powers of $y - 1$, which we may denote by $\hat{g}_p^1(x_0)/p!$. The error is then

$$\begin{aligned} &\left| \sum_{p=n_0}^{\infty} \frac{\hat{g}_p^1(x_0)}{p!} \int_{x_0}^1 dy (y-1)^p (q(y, Q^2) - q(x_0, Q^2)) \right| \\ &\leq \int_{x_0}^1 dy \left| \log(1 - x_0/y) - \sum_{p=0}^{n_0-1} \frac{\hat{g}_p^1(x_0)}{p!} (y-1)^p \right| |q(y, Q^2) - q(x_0, Q^2)|. \end{aligned} \quad (4.3.5)$$

The expression inside the first absolute value on the *r.h.s.* of eq. (4.3.5) is just the error made in approximating the logarithm with its Taylor expansion

around $y = 1$; thus, it is a slowly decreasing function of n_0 , it is integrable, and the integral receives the largest contribution from the region $y \sim x_0$; the second absolute value, on the other hand, is a bounded function of y in the range $x_0 \leq y \leq 1$, which vanishes as $y \rightarrow x_0$ for any choice of $q(y, Q^2)$. These two facts combine to limit the size of the error. One can check directly that, choosing for example $q(y, Q^2) = (1 - y)^4$ as in the previous Section, the accuracy is better than 10% with $n_0 \sim 10$ and $x_0 = 0.1$, in agreement with the previous estimate. One may also verify that, as expected, changing the shape of $q(y, Q^2)$ does not significantly affect the result.

4.4 Solving the Altarelli-Parisi equation with truncated moments

The number M of truncated moments needed to achieve a precision on the evolution of the lowest moment comparable to that of other techniques is rather large ($M \sim 150$), and in some cases it may lead to problems in the numerical implementation of the method, even if in practice, it is sufficient to parametrize the parton distributions using the first few (between 7 and 10) truncated moments, plus the value of the parton distributions at $x = x_0$. In this Section we present a different way to improve the numerical efficiency of the method of truncated moments. We begin by studying the unpolarized non-singlet case at leading order, leaving at the end the extension to next-to-leading order.

We now integrate by parts the *r.h.s.* of eq. (4.1.2). We get

$$\begin{aligned} & \int_{x_0}^1 dy y^{n-1} q(y, Q^2) G_n \left(\frac{x_0}{y} \right) \\ &= \left[\tilde{G}_n(x_0, y) y^{n-1} q(y, Q^2) \right]_{x_0}^1 - \int_{x_0}^1 dy \tilde{G}_n(x_0, y) \frac{d}{dy} (y^{n-1} q(y, Q^2)) \end{aligned} \quad (4.4.1)$$

where

$$\tilde{G}_n(x_0, y) = \int_{x_0}^y dz G_n \left(\frac{x_0}{z} \right) \quad (4.4.2)$$

(the lower integration bound is irrelevant here; it has been chosen equal to x_0 for later convenience). Using the definition of $\tilde{G}_n(x_0, y)$ and eq. (4.1.3), we get

$$\begin{aligned} \tilde{G}_n(x_0, y) &= \int_{x_0}^y dz \int_{x_0/z}^1 dx x^{n-1} P(x) = \int_{x_0/y}^1 dx x^{n-1} P(x) \int_{x_0/x}^y dz \\ &= y G_n \left(\frac{x_0}{y} \right) - x_0 G_{n-1} \left(\frac{x_0}{y} \right). \end{aligned} \quad (4.4.3)$$

By taking the Taylor expansion of $\tilde{G}_n(x_0, y)$ around $y = 1$, we obtain

$$\begin{aligned} \frac{d}{d\tau} q_n(x_0, Q^2) &= \left[\tilde{G}_n(x_0, y) y^{n-1} q(y, Q^2) \right]_{x_0}^1 \\ &- \sum_{p=0}^{\infty} \frac{\tilde{g}_n^p(x_0)}{p!} \int_{x_0}^1 dy (y-1)^p \frac{d}{dy} (y^{n-1} q(y, Q^2)) \end{aligned} \quad (4.4.4)$$

where

$$\tilde{g}_n^p(x_0) = \left[\frac{d^p}{dy^p} \tilde{G}_n(x_0, y) \right]_{y=1} = \left[\frac{d^{p-1}}{dy^{p-1}} \frac{d}{dy} \tilde{G}_n(x_0, y) \right]_{y=1} = g_n^{p-1}(x_0). \quad (4.4.5)$$

The functions $\tilde{G}_n(x_0, y)$ are regular in the whole interval $[x_0, 1]$. In fact, the $G_n(x_0/y)$ are regular for all values of y except $y = x_0$, as they contain singular terms proportional to $\log(1 - x_0/y)$. However, these terms are integrable, and independent of n . Thus, $\tilde{G}_n(x_0, y)$ is regular in the limit $y \rightarrow x_0$ and tends to zero. Furthermore, we observe that the Taylor coefficient of order p of $\tilde{G}_n(x_0, y)$ is equal to that of $G_n(x_0/y)$, times a factor $1/p$ (see eq. (4.4.5)). For this reason, the convergence of the expansion of $\tilde{G}_n(x_0, y)$ is faster than that of $G_n(x_0/y)$.

Integrating by parts the second term of the *r.h.s.* of eq. (4.4.5), we have:

$$\begin{aligned} \frac{d}{d\tau} q_n(x_0, Q^2) &= \left[\tilde{G}_n(x_0, y) y^{n-1} q(y, Q^2) \right]_{x_0}^1 \\ &- \left[\sum_{p=0}^{\infty} \frac{\tilde{g}_n^p(x_0)}{p!} (y-1)^p y^{n-1} q(y, Q^2) \right]_{x_0}^1 \\ &+ \sum_{p=1}^{\infty} \frac{g_n^{p-1}(x_0)}{(p-1)!} \int_{x_0}^1 dy y^{n-1} (y-1)^{p-1} q(y, Q^2) \end{aligned} \quad (4.4.6)$$

Truncating the series, expanding the binomial $(y-1)^{p-1}$ with $q(1, Q^2) = 0$ (this is our only assumption on the behavior of the parton distributions), we get

$$\begin{aligned} \frac{d}{d\tau} q_n(x_0, Q^2) &= x_0^{n-1} q(x_0, Q^2) \sum_{p=0}^M \frac{\tilde{g}_n^p(x_0)}{p!} (x_0-1)^p \\ &+ \sum_{k=0}^{M-1} c_{nk}^{(M-1)}(x_0) q_{n+k}(x_0, Q^2) \end{aligned} \quad (4.4.7)$$

where $c_{nk}^{(M)}(x_0)$ are defined as in eq. (4.1.7). Defining the triangular matrix as in eq. (4.1.9) we can finally write the truncated evolution equation as

$$\frac{d}{d\tau} q_n(x_0, Q^2) =$$

$$x_0^{n-1}q(x_0, Q^2) \sum_{p=0}^M \frac{\tilde{g}_n^p(x_0)}{p!} (x_0 - 1)^p + \sum_{l=1}^M C_{nl} q_l(x_0, Q^2). \quad (4.4.8)$$

Notice that the first term in the *r.h.s.* of eq. (4.4.8) vanishes in the limit $M \rightarrow \infty$ and the original expression given in eq. (4.1.8) with $n_0 = 1$ is recovered. However, for finite values of M this term must be taken into account (in a sense, it is the price we have to pay for the better convergence of the expansion after the integration by parts). This term poses special problems because it depends on the value of the parton distributions at $x = x_0$. In the following we will show how to obtain an approximated expression of $q(x_0, Q^2)$ in terms of a finite number N (not necessarily equal to M) of truncated moments. The evolution equation (4.4.8) will then be solved with a technique similar to that presented in Sect. 4.1.

We begin by taking the Taylor expansion of $q(x, Q^2)$ around $x = y_0$:

$$q(x, Q^2) = \sum_{k=1}^{\infty} \eta_k(Q^2) (x - y_0)^{k-1}, \quad (4.4.9)$$

The initial point of the expansion, y_0 , must be carefully chosen. Parton distributions parametrized as in eq. (4.2.4) are non-analytical in $x = 1$ when the exponent a_2 is not an integer; and even in that case, an essential singularity in $x = 1$ is generated by perturbative evolution. One should therefore choose $y_0 \leq (1 + x_0)/2$, so that the expansion (4.4.9) is convergent everywhere in $[x_0, 1)$. The series will not be convergent in $x = 1$, no matter what y_0 is; however, the singularity in $x = 1$ is integrable, and the term-by-term integration is allowed using the Lebesgue definition of the integral as we did in Sect. 4.1. We have therefore

$$q_j(x_0, Q^2) = \int_{x_0}^1 dx x^{j-1} q(x, Q^2) = \sum_{k=1}^{\infty} \beta_{jk}(x_0, y_0) \eta_k(Q^2), \quad (4.4.10)$$

where

$$\beta_{jk}(x_0, y_0) = \int_{x_0}^1 dx x^{j-1} (x - y_0)^{k-1}. \quad (4.4.11)$$

Our task is now to find a way of inverting eq. (4.4.10), in order to express the coefficients $\eta_k(Q^2)$ in terms of the truncated moments $q_j(x_0, Q^2)$. This can be done in the following way. Define a matrix $\tilde{\beta}^{-1}$ by

$$\tilde{\beta}_{kj}^{-1} = \begin{cases} (\beta^{(N)})_{kj}^{-1} & k, j \leq N \\ 0 & \text{otherwise} \end{cases} \quad (4.4.12)$$

where $\beta^{(N)}$ is the $N \times N$ upper left sub-matrix of β . For example, in the case $N = 2$ the matrix $\tilde{\beta}^{-1}$ is such that

$$\tilde{\beta}^{-1} \cdot \beta = \begin{pmatrix} 1 & 0 & \frac{\beta_{13}\beta_{22}-\beta_{23}\beta_{12}}{\det \beta^{(2)}} & \cdots \\ 0 & 1 & \frac{\beta_{23}\beta_{11}-\beta_{13}\beta_{21}}{\det \beta^{(2)}} & \cdots \\ 0 & 0 & 0 & \cdots \\ \vdots & \vdots & \vdots & \ddots \end{pmatrix} \quad (4.4.13)$$

Multiplying eq. (4.4.10) by $\tilde{\beta}^{-1}$ on the right, we obtain

$$\sum_{j=1}^N \tilde{\beta}_{ij}^{-1} q_j(x_0, Q^2) = \sum_{k=1}^{\infty} \sum_{j=1}^N \tilde{\beta}_{ij}^{-1} \beta_{jk} \eta_k(Q^2), \quad (4.4.14)$$

where for simplicity we have not shown the dependence on x_0, y_0 . Using the definition of $\tilde{\beta}^{-1}$ we get

$$\sum_{j=1}^N \tilde{\beta}_{ij}^{-1} q_j(x_0, Q^2) \equiv \eta_i(Q^2) + \sum_{k=N+1}^{\infty} \sum_{j=1}^N \tilde{\beta}_{ij}^{-1} \beta_{jk} \eta_k(Q^2) \quad (4.4.15)$$

for $i \leq N$. Substituting eq. (4.4.15) in eq. (4.4.9) gives

$$q(x_0, Q^2) = \sum_{k=1}^N \sum_{j=1}^N \tilde{\beta}_{kj}^{-1} q_j(x_0, Q^2) (x_0 - y_0)^{k-1} + R(x_0, y_0, Q^2), \quad (4.4.16)$$

where

$$\begin{aligned} R(x_0, y_0, Q^2) &= \sum_{k=N+1}^{\infty} \eta_k(Q^2) \left[(x_0 - y_0)^{k-1} \right. \\ &\quad \left. - \sum_{i=1}^N (x_0 - y_0)^{i-1} \sum_{j=1}^N \tilde{\beta}_{ij}^{-1} \beta_{jk} \right]. \end{aligned} \quad (4.4.17)$$

We have thus obtained an approximate expression of $q(x_0, Q^2)$ as a function of the first N truncated moments of q , eq. (4.4.16); the quantity R in eq. (4.4.17) represents the error on this reconstruction. The quantity in square brackets in eq. (4.4.17) is independent of the parton distributions, and can be computed for any N and k starting from the coefficients β_{ij} , given by eq. (4.4.11). The analytic expression of this quantity is very complicated. We have checked that, for $y_0 = (1 + x_0)/2$, it decreases as $[(x_0 - 1)/2]^{k-1}$, for any value of N . Therefore, $R(x_0, y_0, Q^2)$ vanishes, for $N \rightarrow \infty$, at least as fast as the remainder of order N of the Taylor expansion in eq. (4.4.9).

In order to assess the accuracy of our approximation, we have computed the percentage error given by ratio $|R/q(x_0, Q^2)|$ for some representative choices of the parton density, namely $q(x, Q^2) = (1 - x)^{a_2}$ with $a_2 =$

$x_0 = 0.1$			
N	$a_2 = 2.5$	$a_2 = 3.5$	$a_2 = 4.5$
5	3.3×10^{-4}	3.2×10^{-4}	1.4×10^{-3}
10	3.8×10^{-6}	5.4×10^{-7}	1.4×10^{-7}
15	3.2×10^{-7}	1.8×10^{-8}	1.8×10^{-9}

Table 4.4. Precision in the reconstruction of $q(x_0, Q^2) = (1 - x_0)^{a_2}$ in terms of a finite number N of truncated moments, for different values of N and for three different choices of a_2 .

2.5, 3.5, 4.5. We have fixed $x_0 = 0.1$ and $y_0 = (1 + x_0)/2$. The results are shown in Table 4.4. We see that an excellent approximation is achieved already with $N = 5$, independently of the value of the large- x exponent a_2 . The accuracy increases with increasing N ; however, it should be noted that a numerical evaluation of the matrix $\tilde{\beta}^{-1}$ requires a numerical precision which also rapidly increases with N . Therefore, for a practical implementation of the method, N cannot be very large. We see from Table 4.4 that for $5 \leq N \leq 10$ the accuracy is already better than 10^{-3} in the cases we have studied. We conclude that

$$q(x_0, Q^2) \simeq \sum_{j=1}^N \left[\sum_{k=1}^N \tilde{\beta}_{kj}^{-1}(x_0, y_0) (x_0 - y_0)^{k-1} \right] q_j(x_0, Q^2) \quad (4.4.18)$$

to an accuracy of about 10^{-3} for $N = 5$, independent of the detailed shape of $q(x, Q^2)$, and rapidly increasing with N .

We are now ready to re-write the original evolution equation (4.4.8) using our result eq. (4.4.18). We get

$$\frac{d}{d\tau} q_n(x_0, Q^2) = \sum_{l=1}^M C_{nl} q_l(x_0, Q^2) + \sum_{l=1}^M D_{nl}^{(N)} q_l(x_0, Q^2), \quad (4.4.19)$$

where C_{nl} is defined in eq. (4.1.9), and

$$D_{nl}^{(N)} = x_0^{n-1} \left[\sum_{p=0}^M \frac{\tilde{g}_n^p(x_0)}{p!} (x_0 - 1)^p \right] \left[\sum_{k=1}^N \tilde{\beta}_{kl}^{-1}(x_0, y_0) (x_0 - y_0)^{k-1} \right]. \quad (4.4.20)$$

We now turn to a test of the accuracy of the evolution equation. We will also compare the accuracy achieved with the method presented in this Section, and that of Sect. 4.1. The original evolution equation (4.1.2) and its truncated version, eq. (4.1.6), can be written schematically as

$$\frac{d}{d\tau} q_n(x_0, Q^2) = S_n \qquad \frac{d}{d\tau} q_n(x_0, Q^2) = S_n^{(M)} \quad (4.4.21)$$

$x_0 = 0.1$				
M	$\mathcal{R}_{1,M}^a$	$\mathcal{R}_{1,M,6}^b$	$\mathcal{R}_{2,M}^a$	$\mathcal{R}_{2,M,6}^b$
5	0.62	0.14	0.14	0.020
10	0.48	0.07	0.12	0.016
20	0.33	0.03	0.09	0.009
40	0.20	0.01	0.05	0.004

Table 4.5. Comparison between percentage errors for the first and the second truncated moment at LO with $N = 6$, $x_0 = 0.1$, $y_0 = (1 + x_0)/2$ and $q(x, Q^2) = (1 - x)^{3.5}$.

respectively. Therefore, the quantity

$$\mathcal{R}_{n,M}^a = 1 - \frac{S_n^{(M)}}{S_n} \quad (4.4.22)$$

is the same measure of the accuracy of the method given by eq. (4.2.1). Similarly, we write eqs. (4.4.19) in the form

$$\frac{d}{d\tau} q_n(x_0, Q^2) = S_n^{(M-1)} + T_n^{(M,N)}, \quad (4.4.23)$$

and define

$$\mathcal{R}_{n,M,N}^b = 1 - \frac{S_n^{(M-1)} + T_n^{(M,N)}}{S_n} \quad (4.4.24)$$

to test the error of the method presented above. The values of $\mathcal{R}_{n,M}^{a,b}$, computed at leading order with $x_0 = 0.1$ for $n = 1$ and $n = 2$, are shown in Table 4.5 for different values of M and $N = 6$. We observe that the error $\mathcal{R}_{n,M,N}^b$ computed with the technique presented here is always much smaller than the corresponding error presented in Sect. 4.1, $\mathcal{R}_{n,M}^a$. An accuracy of less than 10% can be achieved with a relatively small value of M . In Table 4.6 we show also the comparison between percentage errors with $x_0 = 0.01$. We observe that, accordingly to what we have discussed in Sect. 4.2, the percentage error on the second truncated moment is smaller for $x_0 = 0.01$ than for $x_0 = 0.1$, while it is larger for the first truncated moment.

Finally, in Fig. 4.2, we show the x_0 dependence of the *r.h.s.* of the evolution equation for the first and the second truncated moments. In both cases, we note that the approximation of the exact case is very good.

The complete solution of the evolution equation, LO and NLO terms, can be written as

$$q_n(x_0, Q^2) = R^{-1} \left[e^{\gamma\tau} + a e^{(\gamma+b_0)\tau} \int_0^\tau d\sigma e^{-(\gamma+b_0)\sigma} (\widehat{C}_1 + \widehat{D}_1) e^{\gamma\sigma} \right] R q_n(x_0, Q_0^2), \quad (4.4.25)$$

$x_0 = 0.01$				
M	$\mathcal{R}_{1,M}^a$	$\mathcal{R}_{1,M,6}^b$	$\mathcal{R}_{2,M}^a$	$\mathcal{R}_{2,M,6}^b$
5	0.78	0.11	0.0042	0.0019
10	0.70	0.06	0.0039	0.0017
20	0.58	0.03	0.0035	0.0014
40	0.46	0.01	0.0030	0.0009

Table 4.6. Comparison between percentage errors for the first and the second truncated moment at LO with $N = 6$, $x_0 = 0.1$, $y_0 = (1 + x_0)/2$ and $q(x, Q^2) = (1 - x)^{3.5}$.

with the initial condition

$$q_n(x_0, Q_0^2) = q_n^{(0)}(x_0, Q_0^2) + a(0)q_n^{(1)}(x_0, Q_0^2), \quad (4.4.26)$$

and

$$\begin{aligned} R(C_0 + D_0)R^{-1} &= \text{diag}(\gamma_1, \dots, \gamma_M) \equiv \gamma, \\ \widehat{C}_1 + \widehat{D}_1 &= R(C_1 + D_1)R^{-1}. \end{aligned} \quad (4.4.27)$$

The matrix R that diagonalizes $C_0 + D_0$ must be computed numerically. This is not a problem, since, as we have seen, its dimension M does not need to be too large.

The improvement of the numerical efficiency presented here can be extended straightforwardly to the unpolarized singlet case, and to polarized partons as well. The tests we presented are only for the LO equations. We have checked that the inclusion of NLO terms does not modify our conclusions. The technique of truncated moments can now be easily implemented numerically for phenomenological purposes.

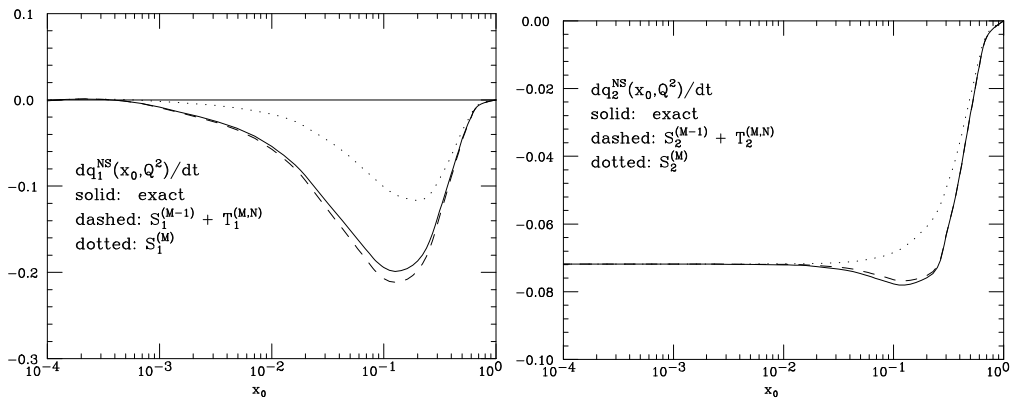


Figure 4.2. Right-hand side of the evolution equations for the first and the second truncated moments of the non-singlet distribution with $M = 10$ and $N = 6$. The overall scale is set by $\alpha_s(2\text{GeV}^2)$.

5

Introduction to Neural Networks

In the present times *artificial neural networks* constitute one of the most successful and multidisciplinary subjects. People with very different formation, ranging from physicists to philosophers, and from biologists to engineers, are working on them trying to understand better and better how they work. Applications of artificial neural networks are widely used from images reconstruction to financial markets predictions. Artificial neural network methods are well established techniques for high energy physics too, where they are used for event reconstruction in particle accelerators. Quark-gluon separation, heavy quark jet tagging, mass reconstruction, and track finding procedures make use of artificial neural networks [32].

Here we will give a very brief and general introduction to artificial neural networks (henceforth simply neural networks). Our main interest is to describe the very basic algorithms of neural networks, and some useful practical issues in order to better understand the fits presented in the following Chapter.

5.1 From biology to artificial neural networks

The structure of biological nervous system started to be understood in 1888, when Dr. Santiago Ramón y Cajal succeeded in seeing the *synapses* between individual nervous cells, the *neurons*. This discovery was quite impressive as it proved that all the capabilities of the human brain rest not so much in the complexity of its constituents as in the enormous number of neurons and connections between them. To give an idea of these magnitudes, the usual estimate of the total number of neurons in the human central nervous system is 10^{11} , with an average of 10000 synapses per neuron. The combination of both numbers yields a total of 10^{15} synaptic connections in a single human

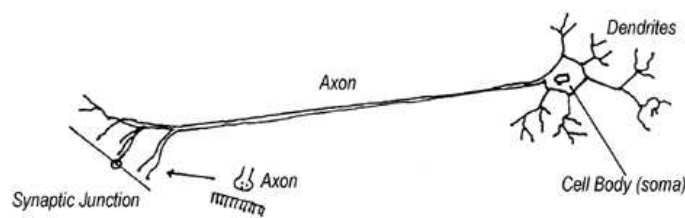


Figure 5.1. Schematic structure of a neuron.

brain. All the neurons share the common structure schematized in Fig. 5.1. There is a *cell body* or *soma* where the *cell nucleus* is located, a tree-like set of fibres called *dendrites* and a single long tabular fibre called the *axon* which arborize as its end. Neurons establish connections either to sensory organs (input signals), to muscle fibres (output signals) or to other neurons (both input and output). The output junctions are called *synapses*. The inter-neuron synapses are placed between the axon of a neuron and the soma or the dendrites of the next one.

The way the neuron works is basically the following: a potential difference of chemical nature appears in the dendrites or soma of the neuron, and if its value reaches a certain threshold then an electrical signal is created in the cell body, which immediately propagates through the axon without decaying in intensity. When it reaches its end, this signal is able to induce a new potential difference in the post-synaptic cells, whose answer may or may not be another *firing* of a neuron or a contraction of a muscle fibre, and so on. Of course a much more detailed overview could be given, but this suffices for our purposes.

In 1943 W. S. McCulloch and W. Pitts [33] suggested a mathematical model for capturing some of the above characteristics of the brain. First, an *artificial neuron* (or simply a *neuron*) is defined as a processing element whose state ξ at time t can take two different values only: $\xi(t) = 1$, if it is firing, or $\xi(t) = 0$, if it is at rest. The state of, say, the i^{th} unit, $\xi_i(t)$, depends on the inputs from the rest of the N neurons through the discrete dynamical equation

$$\xi_i(t) = \Theta \left(\sum_{j=1}^N \omega_{ij} \xi_j(t-1) - \theta_i \right), \quad (5.1.1)$$

where the *weights* ω_{ij} represent the strength of the synaptic coupling between the j^{th} and the i^{th} neurons, θ_i is the *threshold* which points out the limit

Figure 5.2. A three-layer perceptron consisting of input, hidden and output layers.

between firing and rest, and Θ is the unit step *activation function* defined as

$$\Theta(h) \equiv \begin{cases} 0 & \text{if } h \leq 0, \\ 1 & \text{if } h > 0. \end{cases} \quad (5.1.2)$$

Then, a set of mutually connected McCulloch-Pitts units is what is called an *artificial neural network*.

In spite of the simplicity of their model, McCulloch and Pitts were able to prove that artificial neural networks could be used to any desired computation, once the weights ω_{ij} and the thresholds θ_i were chosen properly. This fact made that the interest toward artificial neural networks was not limited to the description of the collective behavior of the brain, but also as a new paradigm of computing.

5.2 Multilayer Neural Networks

Among the different types of neural networks, those in which we have concentrated our interest are Rosenblatt's *perceptrons*, also known as *multilayer feed-forward neural networks* [34]. In these networks there is a layer of input units whose only role is to feed input patterns into the rest of the networks. Next, there are one or more intermediate or hidden layers of neurons evaluating the same kind of function of the weighted sum of inputs, which, in turn, send it forward to units in the following layer. This process goes on until the output level is reached, thus making it possible to read off the computation.

In the class of networks one usually deals with, there are no connections leading from a neuron to units in the previous layers, nor to neurons further than the next contiguous level, *i.e.* every unit feeds only the ones contained in the next layer. Once we have updated all the neurons in the right order, they will not change their states. For these architectures time plays no role.

In Fig. 5.2 we have represented a three-layer perceptron with n_1 input units, n_2 hidden units in a single hidden layer, and n_3 outputs. When an input vector ξ is introduced to the network, the states of the hidden neurons acquire the values

$$\sigma_i = g \left(\sum_{k=1}^{n_1} \omega_{ik}^{(2)} \xi_k - \theta_i^{(2)} \right), i = 1, \dots, n_2; \quad (5.2.1)$$

the output of the network is the vector ζ whose components are given by

$$\zeta_i = g \left(\sum_{j=1}^{n_2} \omega_{ij}^{(3)} \sigma_j - \theta_i^{(3)} \right), i = 1, \dots, n_3. \quad (5.2.2)$$

Here we have supposed that the *activation function* can be any arbitrary function g , though it is customary to work only with bounded ones either in the interval $[0, 1]$ or $[-1, 1]$. If this transfer function is of the form of the Θ step function it is said that the activation is *discrete*, since the states of the neurons are forced to be in one of a finite number of different possible values. Otherwise, continuous functions commonly used are the *sigmoids* or *Fermi functions*

$$g(h) \equiv \frac{1}{1 + e^{-\beta h}}, \quad (5.2.3)$$

which satisfy

$$\lim_{\beta \rightarrow \infty} g(h) = \Theta(h). \quad (5.2.4)$$

In the terminology of statistical mechanics the parameter β is regarded as the inverse of a temperature. However, for our practical applications we will set $\beta = 1$.

Generally, if we have L layers with n_1, \dots, n_L units respectively, the state of the multilayer perceptron is established by recursive relations

$$\xi_i^{(l)} = g \left(\sum_{j=1}^{n_{l-1}} \omega_{ij}^{(l-1)} \xi_j^{(l-1)} - \theta_i^{(l)} \right), i = 1, \dots, n_l, l = 2, \dots, L, \quad (5.2.5)$$

where $\xi^{(l)}$ represents the state of the neurons in the l^{th} layer, $\omega_{ij}^{(l)}$ the weights between units in the $(l-1)^{th}$ and the l^{th} layers, and $\theta_i^{(l)}$ the threshold of the i^{th} unit in the l^{th} layer. Then the input is the vector $\xi^{(1)}$ and the output the vector $\xi^{(L)}$.

By *simple perceptron* one refers to networks with just two layers, the input one and the output one, without internal units, in the sense that there are

no intermediate layers. These devices have been seen to have limitations, such as the XOR problem, which do not show up in feed-forward networks with hidden layers present. Actually, it has been proved that a network with just one hidden layer can represent any Boolean function [35]. Any continuous function can be uniformly approximated by a continuous neural network having only one internal layer, and with an arbitrary continuous sigmoid non-linearity [36].

5.3 Learning process of Neural Networks

Connecting neurons together may well produce networks that can do something, but we need to be able to *train* them in order to make them do anything useful. We also want to find the simplest learning rule that we can, in order to keep our model understandable. As is often the case in neural computing, inspiration comes from looking at real neural systems.

Dogs are given tit-bits to encourage them to come when called. Generally, good behavior is reinforced, while bad behavior is reprimanded. We can transfer this idea to our network. The guiding principle is to allow neurons to learn from mistakes. If they produce an incorrect output, we want to reduce the chances of that happening again; if they come up with correct output, then we need do nothing. The learning paradigm can be summarized as follows:

- set the weights and thresholds randomly;
- present an input;
- calculate the actual output by taking the thresholded value of the weighted sum of the inputs;
- alter the weights to reinforce correct decisions and discourage incorrect ones, *i.e.* reduce the error;
- present the input next time, etc.

5.3.1 A simple perceptron learning algorithm

Let us consider the set

$$\{(\mathbf{x}^\mu, \mathbf{z}^\mu) \in \mathbb{R}^n \times \mathbb{R}^m, \mu = 1, \dots, p\} \quad (5.3.1)$$

of pairs input-output and a simple perceptron, *i.e.* a neural network with only two layers. The equations governing the state of the network are given by

$$\xi_i^{(2)} = g(h_i), i = 1, \dots, m, \quad (5.3.2)$$

where the fields are given by

$$h_i = \sum_{j=1}^n \omega_{ij} \xi_j^{(1)} - \theta_i. \quad (5.3.3)$$

We shall use the notation for the input and output patterns:

$$\begin{cases} \mathbf{x} &= \boldsymbol{\xi}^{(1)}, \\ \mathbf{o}(\mathbf{x}) &= \boldsymbol{\xi}^{(2)}. \end{cases} \quad (5.3.4)$$

For any given values of the weights and thresholds it is possible to calculate the *quadratic error* between the actual and the desired output of the network, measured over the training set:

$$E[\mathbf{o}] \equiv \frac{1}{2} \sum_{\mu=1}^p \sum_{i=1}^m (o_i(\mathbf{x}^\mu) - z_i^\mu)^2. \quad (5.3.5)$$

Therefore, the last squares estimate minimizes $E[\mathbf{o}]$. Applying the *gradient descent minimization* procedure, what we have to do is just to look for the direction (in the space of weights and thresholds) to steepest descent of the error function (which coincides with minus the gradient), and then modify the parameters in that direction so as to decrease the actual error:

$$\delta\omega_{ij} = -\eta \frac{\partial E}{\partial \omega_{ij}} = -\eta (o_i(\mathbf{x}^\mu) - z_i^\mu) g'(\boldsymbol{\omega}_i \cdot \mathbf{x}) x_j, \quad (5.3.6)$$

$$\delta\theta_i = -\eta \frac{\partial E}{\partial \theta_i} = -\eta (o_i(\mathbf{x}^\mu) - z_i^\mu) g'(\boldsymbol{\omega}_i \cdot \mathbf{x})$$

where $\boldsymbol{\omega}_i \cdot \mathbf{x} = \sum_{j=0} \omega_{ij} x_j$, with the updating rule

$$\begin{aligned} \omega_{ij}(t+1) &\longrightarrow \omega_{ij}(t) + \delta\omega_{ij}, \\ \theta_i(t+1) &\longrightarrow \theta_i(t) + \delta\theta_i. \end{aligned} \quad (5.3.7)$$

The appearance of the derivative g' of the activation function explains why we have supposed in advance that it has to be continuous and differentiable. The intensity of the change is controlled by the *learning rate* parameter η . When no more changes (within some accuracy) occurs, *i.e.* $\delta\omega_{ij} \sim 0$, the weights are frozen and the network is ready to use for data it has never “seen”. The procedure is summarized as follows:

1. initialize ω_{ij} with \pm random values;
2. pick pattern p from the training set;
3. feed input \mathbf{x} to network and calculate the output \mathbf{o} ;
4. update the weights according to eq. (5.3.7) and eq. (5.3.6);
5. repeat from 2 until $\omega_{ij}(t+1) \sim \omega_{ij}(t)$.

5.3.2 Learning by error back-propagation

We now consider a multilayer neural network and generalize the *delta rule* or *gradient descent procedure* that we have seen in the perceptron case, eq. (5.3.6) [37]. The equations that describes the multilayer neural network are given by

$$\xi_i^{(l)} = g(h_i^{(l)}), i = 1, \dots, m, \quad (5.3.8)$$

$$h_i^{(l)} = \sum_{j=1}^{n_{l-1}} \omega_{ij}^{(l-1)} \xi_j^{(l-1)} - \theta_i^{(l)}. \quad (5.3.9)$$

$$\delta\omega_{ij}^{(l)} = -\eta \frac{\partial E}{\partial \omega_{ij}^{(l)}}, \quad (5.3.10)$$

$$\delta\theta_i^{(l)} = -\eta \frac{\partial E}{\partial \theta_i^{(l)}}$$

Substituting the first two equations in eq. (5.3.5), and taking the derivatives, it is easy to get

$$\delta\omega_{ij}^{(l)} = -\eta \sum_{\mu=1}^p \Delta_i^{(l)\mu} \xi_j^{(l-1)\mu}, \quad i = 1, \dots, n_l, \quad j = 1, \dots, n_{l-1}, \quad (5.3.11)$$

$$\delta\theta_i^{(l)} = \eta \sum_{\mu=1}^p \Delta_i^{(l)\mu}, \quad i = 1, \dots, n_l,$$

where the error is introduced in the units of the last layer through

$$\Delta_i^{(L)\mu} = g'(h_i^{(L)\mu}) [o_i(\mathbf{x}^\mu) - z_i^\mu] \quad (5.3.12)$$

and then is *back-propagated* to the rest of the network by

$$\Delta_j^{(l-1)\mu} = g'(h_j^{(l-1)\mu}) \sum_{i=1}^{n_l} \Delta_i^{(l)\mu} \omega_{ij}^{(l)}. \quad (5.3.13)$$

This result can be easily derived by taking a neural network with only one hidden layer. Summarizing the *batched back-propagation* algorithm for the learning of the training set (5.3.1) consists in the following steps

1. initialize all the weights and thresholds randomly, and choose a small value for the learning rate η ;

- run a pattern \mathbf{x}^μ of the training set and store the activations of all the units (*i.e.* $\{\xi_i^{(l)\mu}, \forall l \forall i\}$);
- calculate the $\Delta_i^{(L)\mu}$ and then back-propagate the error using eq.(5.3.13);
- compute contributions to $\delta\omega_{ij}^{(l)}$ and $\delta\theta_i^{(l)}$, induced by this input-output pair $(\mathbf{x}^\mu, \mathbf{z}^\mu)$;
- update weights and thresholds;
- go to the second step unless enough training epochs have been carried out.

The adjective “batched” refers to the fact that the update of the weights and thresholds is done after all patterns have been presented to the network. Nevertheless, simulations show that, in order to speed up the learning, it is usually preferable to perform this update each time a new pattern is processed, choosing them in random order: this is known as *non-batched* or *on-line back-propagation*. Generally, we choose the on-line mode if the number of patterns is small (*i.e.* $\sim 10^3$), and the batched one if it is large.

It is clear that back-propagation seeks minima of the error function given in eq. (5.3.5), but it cannot ensure that it ends in a global one, since the procedure may get stucked in a *local minimum*. Several modifications have been proposed to improve the algorithm so as to avoid local minima and to accelerate its convergence. One of the most successful, simple and commonly used variants is the introduction of a *momentum term* to the updating rule, either in the batched or the on-line schemes. It consists in the substitution of eq. (5.3.10) by

$$\begin{aligned}\delta\omega_{ij}^{(l)} &= -\eta \frac{\partial E}{\partial \omega_{ij}^{(l)}} + \alpha \delta\omega_{ij}^{(l)}(\text{last}), \\ \delta\theta_i^{(l)} &= -\eta \frac{\partial E}{\partial \theta_i^{(l)}} + \alpha \delta\theta_i^{(l)}(\text{last})\end{aligned}\tag{5.3.14}$$

where the “last” means the values of the $\delta\omega_{ij}^{(l)}$ and $\delta\theta_i^{(l)}$ used in the previous updating of the weights and thresholds. The parameter α is called momentum of the learning, and it has to be a positive number smaller than 1.

5.4 Practical issues

5.4.1 Rules of thumb

Number of layers

The number of layers issue depends on the specific task one wants the networks to perform, but a general statement is that no more than two hidden layers are needed, even though very many units might be needed in these layers.

Any function, no matter how complex, can be represented by a multilayer neural network of no more than three layers; the inputs are fed through an input layer, a middle hidden layer, and an output layer. This is an important result in that it proves that whatever is done in four or more layers could also be done in three. However, we note that with only one hidden layer one may need a very large number of units in the hidden layer. Thus, it could be more useful to have two hidden layers and a smaller number of neurons on each. Notice also that, as the sigmoid is very close to a step function, if we have a neural network with two hidden layers and a small number of units it could be useful to adopt a linear activation function between the last two layers to have a smoother output.

Number of hidden units

The number of hidden units needed to approximate a given function \mathcal{F} is related to how many terms are needed in an expansion of \mathcal{F} in the function $g()$. There are several techniques to determine the optimal number of units. We can reduce a large number units by the *weight decay* approach, where weights which are rarely updated are allowed to decay according to

$$\delta_{ij} = -\eta \frac{\partial E}{\partial \omega_{ij}} - \epsilon \omega_{ij}, \quad (5.4.1)$$

where ϵ is the decay parameter, typically a very small number, $\mathcal{O}(10^{-4})$. This corresponds to adding an extra complexity term to the energy function [38]

$$E \rightarrow E + \frac{\epsilon}{2\eta} \sum_{i,j} \omega_{ij} \quad (5.4.2)$$

imposing a “cost” for large weights. A more advanced complexity term [38] is

$$E \rightarrow E + \lambda \sum_{i,j} \frac{\omega_{ij}^2/\omega_0^2}{1 + \omega_{ij}^2/\omega_0^2}, \quad (5.4.3)$$

where the sum extends over all weights. For large $|\omega_{ij}|$ the cost is λ , whereas for small weights it is zero. The scale of weights is set by ω_0 . In this way the

cost reflects the number of weights, instead of the size, hence the network gets *pruned* to only contain weights that are really needed to represent the problem. One can also begin with a small number of units, and then increases it one by one by *trial-and-error* till a stability of the error function or of a given indicator is reached.

Learning parameters

If the activation $\langle \xi_i \rangle$ of output node i is large, the optimal η for weights connecting to that unit will be small. The natural thing is to rescale the input data such that $\langle \xi_i \rangle \sim \mathcal{O}(1)$ for all i , in which case they will have approximately the same optimal η (even the thresholds). This also simplifies for the case of the hidden units where $\langle h_i \rangle \sim \mathcal{O}(1)$ for sigmoidal units, and the same learning rate can be used for all weight layers.

The momentum term α controls the “averaging” of the updatings and it is closely connected to the learning rate. An increase of α means an increase of the “effective” learning rate. The optimum α depends on the updating procedure used. For the batched method α is very useful and should be a number close to unity ($0.5 < \alpha < 1$). For the on-line updating, on the other hand, α is often (but not always) useless.

Time dependence

One can choose a learning parameter that varies with time. In this way after the region of the minimum is reached with a large η , the learning rate is reduced as to avoid to get out of there and to refine the research of the minimum. Notice however that if a local minimum is reached in this way one can not get out of there.

Choosing patterns

If patterns are shown sequentially, there may result a bias, *e.g.* due to a regularity of some sequential input patterns in giving a positive variations of weights. This is the reason why it is a good rule to choose patterns randomly. It is also a good rule to show a pattern as an input at least 10^4 times, in order to allow compensations of different variations.

5.4.2 Generalization

One of the major features of neural networks is their ability to generalize, *i.e.* to classify successfully patterns that have not been previously presented. Multilayer neural networks generalize by detecting features of the input pattern that have been learned to be significant, and so coded into the internal

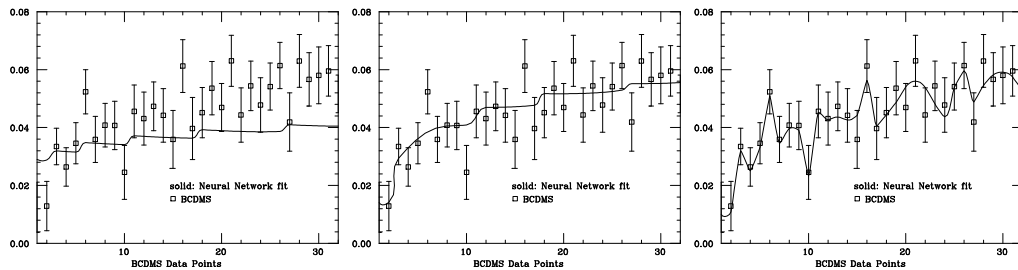


Figure 5.3. *Different trainings for a fit of the non-singlet structure function $F_2^p - F_2^d$ for a subset of BCDMS data points.*

units. Thus an unknown pattern is classified with others that share the same distinguishing features. This means that learning by example is a feasible proposition, since only a representative set of patterns have to be taught the network, and the generalization properties will allow similar inputs to be classified as well. It also means that noisy inputs will be classified, by virtue of their similarity with the pure input. It is generalization ability that allows multilayer neural networks to perform more successfully on real-world problems than other pattern recognition or expert systems.

Generally, neural networks are good at interpolation, but not so good at extrapolation. They are able to detect the patterns that exist in the inputs they are given, and allow for intermediate states that have not been seen. However, inputs that are extensions of the range patterns are less well classified, since there is little which compare them with. Put another way, given an unseen pattern that is an intermediate mixture of two previously taught patterns, the net will classify it as an example of the predominant pattern. If the pattern does not correspond to anything similar to what the neural network has seen before, then the classification will be much poorer. Notice also that the generalization performance is usually lower than its performance on the training set, although for very large data sets the performance can be approximately equal. For a feed-forward network with one hidden layer, the generalization error is of order $\mathcal{O}(N_\omega/N_p)$ where N_ω is the number of weights and N_p the number of training patterns [39].

In Fig. 5.3 we show, as an example, a plot with three different trainings of the structure function $F_2^p - F_2^d$ (details will be given in the next chapter). We have chosen the architecture (4,5,3,1) that will be used in the following, and we have trained the neural network on a very small arbitrary chosen subset of data, *i.e.* 30 experimental points from the BCDMS data (see later).

In the first plot we can see a very smooth almost constant function which corresponds to a very short training. Here we see that the neural network strongly correlates data points, but since there has been no enough training it does not reproduce the behavior of data. The second plot corresponds to a

longer training. Here we see that the neural network has found an underlying law from data; also in this case it strongly correlates data points, but now it reproduce their behavior. The last plot shows the result of a very long training. Here the neural network goes on top of many data point loosing its generalization ability. This is what is called *over-learning*. If the number of weights of the neural network is equal to the number of data points we can have over-learning for a large enough number of training epochs. If the number of weights is less than the number of points and the number of training epochs is large enough we can have only partial over-learning.

6

Neural Network fit of F_2

The DIS cross section is expressed in terms of the nucleon structure function F_2 , that carries informations about the inner structure of the nucleon. If we were able to solve QCD in the non-perturbative domain, we could calculate F_2 with quark masses and Λ_{QCD} as the only inputs. Unfortunately this is not the case at present times. However, we need a more and more detailed knowledge of the structure of nucleons as they are essential ingredients for present and future hadron colliders [40]. Note that the unpolarized structure function is necessary also to determine the polarized structure function from the spin asymmetry in polarized deep inelastic scattering. Although the accuracy of such experiments is not yet very high, it could be anyway useful for future tasks to minimize the sources of errors. We have thus to extract as much precise information as possible from experiments. For this purpose we present here an alternative approach to extract F_2 from data. Results will also be published in Ref. [41].

The Chapter is organized as follows. First we will describe the experimental data used in our fit with details on correlated systematic uncertainties. Then, we will discuss techniques to calculate errors and correlations from the fitted F_2 , and we will show how we can minimize theoretical assumptions on the shape of the structure functions with the help of neural networks. A detailed description of the behavior of neural networks will be given. Finally, we will show our results for the non-singlet structure function $F_2^p - F_2^d$, and preliminary results on the proton and the deuteron structure functions.

6.1 Experimental data

We have used experimental data given by the New Muon Collaboration (NMC) [42] and the BCDMS (Bologna-CERN-Dubna-Munich-Saclay) Collaboration [43] as they measure both the proton and the deuteron structure functions. We have not considered data given by the E665 Collaboration

[44]. E665 data cover a kinematic range with small x and Q^2 , that is almost entirely excluded in the analysis performed in Chapter 7. The inclusion of these data would have implied a further effort, and would not have been very significant to our purpose. A future analysis may consider these data as well. Note, however, that since some of these data cover a kinematic range similar to that of NMC, we could use them to test the prediction ability of our neural networks ¹. Details on errors of both the experiments are given below. In Fig. 6.1 we show the kinematic region explored by the experiments.

6.1.1 NMC

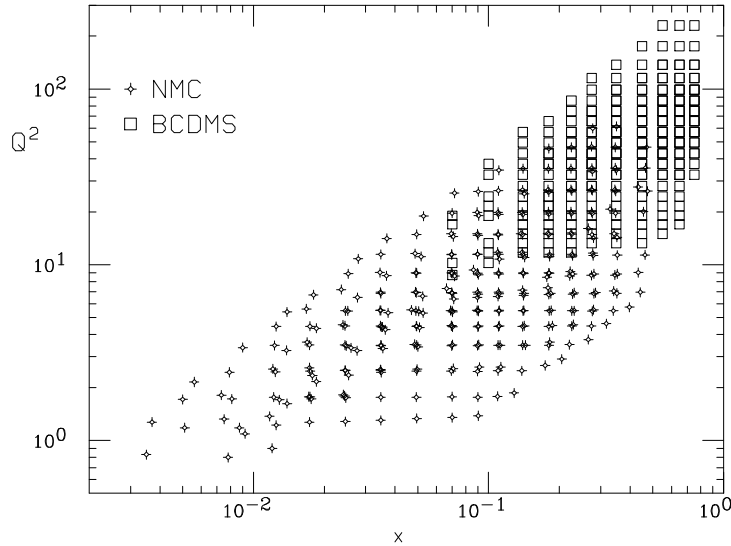
We have used data and data tables given in [42]. NMC data consist of four data sets for the proton and the deuteron structure functions corresponding to beam energies of 90, 120, 200 and 280 GeV, covering the kinematic range $0.002 \leq x \leq 0.60$ and $0.5 \text{ GeV}^2 \leq Q^2 \leq 75 \text{ GeV}^2$. The systematic errors are:

- the incoming (E) and outgoing beam (E') energies, fully correlated between the proton and the deuteron data, but independent for the data taken at different beam energies;
- the radiative correction (RC), fully correlated between all energies, but independent for the proton and the deuteron;
- the acceptance (AC) and the reconstruction efficiency (RE) fully correlated for all data sets;
- the normalization uncertainty (2%), correlated between the proton and the deuteron data, but independent for data taken at different beam energies.

The uncertainties due to acceptance range from 0.1 to 2.5% and reach at most 5% at large x and Q^2 . The uncertainty due to radiative corrections is highest at small x and large Q^2 and is at most 2%. The uncertainty due to reconstruction efficiency is estimated to be 4% at most. The uncertainties due to the incoming and the scattered muon energies contribute to the systematic error by at most 2.5%.

Finally note that each bin of data has larger statistical errors in the extremes and lower in the middle. In particular the worse points are those of larger Q^2 . The experimental reason for this effect is related to the details of the geometry of the detector and to the explored kinematic region. As one pushes the detection to some areas at the limit of the acceptance region many points are lost and the statistics goes down significantly.

¹Remember that neural networks are good in interpolation, but their are not in extrapolation. Thus, it is reasonable to test them on a kinematic range similar to the one they have been trained on.

Figure 6.1. *NMC and BCDMS kinematic range.*

6.1.2 BCDMS

We have used data given in [43] and data tables given in [45]. BCDMS data consist of four data sets for the proton structure function corresponding to beam energies of 100, 120, 200 and 280 GeV and three data sets for the deuteron structure function corresponding to beam energies of 120, 200 and 280 GeV covering the kinematic range $0.06 \leq x \leq 0.80$ and $7 \text{ GeV}^2 \leq Q^2 \leq 280 \text{ GeV}^2$. The systematic errors are:

- $f_N = 3\%$, the absolute normalization error totally correlated for all energies and the two targets;
- $f_b < 0.15\%$, the calibration of the incident beam energy;
- $f_s < 0.15\%$, the calibration of the spectrometer magnetic field;
- $f_r < 1\%$, the calibration of the outgoing muon energy;
- f_d , inefficiencies of the detector (negligible).

The first two systematic errors sources have large effects at large x and small Q^2 . Even if the experiments for the two targets were done at different times, the systematic errors are fully correlated for all targets and for all beam energies [46]:

- the calibration of the incoming beam energy E was realized in a magnet on the beam line, and it was dominated by a systematic uncertainty

due to scintillators that measured the muon beam. This position was more stable in time than the precision of measurements;

- the calibration of the outgoing muon energy was reproducible with a relative value of about 0.02%. This remained the same in the four years of the experiment, and thus remained independent of the used target or the beam energy. On the other hand the absolute calibration had an uncertainty at a level of 0.1-0.2%;
- the resolution of the spectrometer depended on the constituent material, which had not changed in the four years, thus same detector, same magnet and same positions. It could have depended on the hadronic production absorbed in the magnet, as these particles perturbed the recognition of the scattered muon. However, the hadronic productions from proton and deuteron are so similar that this effect is negligible.

BCDMS data have a further source of uncertainty due to the relative normalization of data between different beam energies and different targets. Specifically, there is a 2% cross section normalization of data taken with different targets, a 1% relative cross section normalization of data taken at different beam energies for the proton, a 1% relative cross section normalization between data taken at 120 GeV and 200 GeV and 1.5% between data taken at 200 GeV and 280 GeV for the deuteron.

6.2 Fitting procedure

We consider the case where we have M measurements of a nucleon structure function F_2 . The central problem is to determine F_2 based on observations $F_2^{(1)}, \dots, F_2^{(M)}$. Specifically, we can introduce a hypothesis for the structure function F_2 which depends on unknown parameters $\boldsymbol{\theta} = (\theta_1, \dots, \theta_m)$. The goal is then to estimate parameters by comparing the hypothesis with experimental data.

We first discuss as an example a functional parametrization of F_2 (see [47] and references therein). A QCD inspired parametrization of F_2 can be constructed by observing that the evolution equations (3.3.1) introduce a logarithmic dependence on Q^2 , while a polynomial function could fit the dependence on x . Moreover, from the parton model we have a further constraint on the x behavior for $x = 1$. We can then take

$$F_2(x, Q^2) = x^{a_1} f(x, Q^2), \quad (6.2.1)$$

where

$$f(x, Q^2) = A(x) \left[\frac{\log Q^2 / \Lambda^2}{\log Q_0^2 / \Lambda^2} \right]^{B(x)} \left[1 + \frac{C(x)}{Q^2} \right], \quad (6.2.2)$$

and

$$\begin{aligned}
 A(x) &= (1-x)^{a_2} [a_3 + a_4(1-x) + a_5(1-x)^2 \\
 &\quad + a_6(1-x)^3 + a_7(1-x)^4], \\
 B(x) &= b_1 + b_2 x + \frac{b_3}{x + b_4}, \\
 C(x) &= c_1 x + c_2 x^2 + c_3 x^3 + c_4 x^4.
 \end{aligned}
 \tag{6.2.3}$$

The small x behavior of the function is described by the a_1 parameter, while the a_2 term carries most of the information on the large x behavior. The reference scale is fixed arbitrarily at $Q_0^2 = 20 \text{ GeV}^2$, while the value $\Lambda = 0.250 \text{ GeV}$ is extracted from α_s measurements at different Q^2 [48]. The last term of eq. (6.2.2) takes account of *higher twist* effects (see the next Chapter for details).

The total number of parameters in eq. (6.2.1) is 15, and they can be estimated by minimizing the χ^2 on a given set of experimental data. Once the parameters are known we can evaluate any quantity that depends on F_2 , *e.g.* the asymmetry A_1 or a Mellin moment. Since parameters are themselves stochastic variables, they are determined with an error and with a correlation matrix. In this way a value of the structure function is given with an error that is the combination of the parameter errors. Note that because of the non-linearity of F_2 some linearization is necessary to determine the structure function error, and this may be a source of uncertainty. With this approach it may be non-trivial to obtain the errors on two given data points and especially their correlations given by

$$\begin{aligned}
 \text{cov}[F_2(x_1, Q_1^2), F_2(x_2, Q_2^2)] = \\
 \sum_{i,j=1}^m \frac{\partial F_2(x, Q^2)}{\partial \theta_i} \frac{\partial F_2(x, Q^2)}{\partial \theta_j} \Big|_{(x_1, Q_1^2), (x_2, Q_2^2)} \text{cov}[\theta_i, \theta_j].
 \end{aligned}
 \tag{6.2.4}$$

Even more complications arise if we would like to calculate functions of F_2 , as for example a Mellin moment, while it would be a very hard task to evaluate the correlation between two Mellin moments. A possible way to overcome this problem was given in [47]. Indeed, since F_2 is provided with an “estimated error band” one might hope to get a qualitative idea of the error by taking the integrals of the upper and lower curves of the band as estimates of the error on a Mellin moment. This procedure is however meaningless. In fact, if we use the fitted F_2 to extract, as an example, α_s , we note that the error on α_s could be made arbitrarily small by increasing the number of values of Q^2 at which the moment is evaluated (even within a fixed range in Q^2) [28]. This apparently paradoxical result is of course due to the fact that the procedure neglects correlations between the values of the moment extracted from the fit at two different scales, which tend to one as the scales get closer.

The Monte Carlo method is an alternative approach for calculating errors and correlations by using sequences of random numbers. A sequence of Monte Carlo generated values of F_2 may be used to evaluate estimators for errors and correlations of the values of the parameters of F_2 . Techniques for constructing estimators are discussed in Appendix B.3. An important feature of properly constructed estimators is that their statistical accuracy improves as the number of values N in the data sample increases. A question which we will address is how large N must be to achieve an accuracy at the percent level on estimators.

A functional parametrization as the one given in eq. (6.2.1) introduces an uncertainty due to the imposed dependence on x and Q^2 . However, nobody knows which is the real behavior of F_2 , and any assumption on its functional form may be a source of uncertainty, whose exact size is very hard to assess. For this purpose we will consider a fit with a neural network. Indeed, a neural network with a given architecture can describe a structure function as well as, say, a demographic distribution having very different behaviors: the difference only depends on the input and the output data which it is trained with. In this case however we will have a larger number of parameters than with the functional parametrization. The number of parameters included in a fit corresponds more or less at the number of terms included in a Taylor expansion of F_2 . As nobody knows the exact expression of F_2 , nobody also knows how many terms we have to include in its Taylor expansion or the exact number of parameter that we need to fit it. The space of parameters is an infinite dimensional space, and the arbitrary choice of a fixed number of parameters corresponds to an arbitrary reduction of this space without assessing the uncertainty with which this reduction is done. As we have seen in Section 5.4.1 the number of neurons, and then of the parameters, in a neural network is chosen only by looking at the stability of the error function without making any theoretical assumption on their number. We also observe that once the stability of a neural network is reached, information is maintained even in the case a neuron dies. In this way a neural networks guarantees a more robust and less arbitrary parametrization of a structure function. The only request is to determine the most stable and economic architecture for the problem at hand. Thus, a neural network fit of F_2 will avoid both theoretical assumptions on the functional behavior of the structure function and an arbitrary choice of the number of parameters used in the fit.

Specifically, we will proceed as follows. First, we will generate N replicas of artificial data with the given experimental statistical and systematic correlated errors starting from the original ones. Then, we will perform a neural network fit of each replica. Finally, we will take the average over the number of neural networks, reproducing central values, errors and correla-

tions of the original data with an uncertainty that depends on the number of generated replicas N . In this way errors and correlations between two quantities depending on the structure functions (*e.g.* both two values of the A_1 asymmetry or two Mellin moments) can be calculated keeping under control all the theoretical biases.

6.3 Generation of artificial data

Artificial data for the NMC experiment are generated with

$$F_i^{(art)} = (1 + r_7 \sigma_N) \left[F_i^{(exp)} + \frac{r_1 E + r_2 E' + r_3 AC + r_4 RC + r_5 RE}{100} F_i^{(exp)} + r_6 \sigma_{stat} \right], \quad (6.3.1)$$

where the systematic errors have been discussed in the previous section and r_i are random Gaussian numbers. In order to reproduce the correct correlations we choose r_3 and r_5 equal for different energies and target, r_4 equal for data of the same target, r_1 , r_2 and r_7 equal for different targets. Gaussian random numbers are generated with the `gasdev` routine given in [49] and reported in Appendix C.

Artificial data for the BCDMS experiment are generated with

$$F_i^{(art)} = (1 + r_5 \sigma_N) \sqrt{1 + r_6 \sigma_{N_t}} \sqrt{1 + r_7 \sigma_{N_b}} \left[F_i^{(exp)} + \frac{r_1 f_b + r_2 f_s + r_3 f_r}{100} F_i^{(exp)} + r_4 \sigma_{stat} \right], \quad (6.3.2)$$

where the systematic errors have been discussed in the previous section, σ_N is the absolute normalization, σ_{N_t} is the relative normalization between different targets, σ_{N_b} is the relative normalization between different beam energies, r_i are random Gaussian numbers as above. In particular, r_1, r_2, r_3 and r_5 are equal for different energies and different targets, r_6 is the same for data of a given target, r_7 is the same for data of a given energy.

A relative normalization uncertainty σ_{N_m} between two measurements m_1 and m_2 is taken into account by multiplying one measure by $\sqrt{1 + \sigma_{N_m} r}$ and the other by $1/\sqrt{1 + \sigma_{N_m} r}$, where r is a random Gaussian number. In this way the product $m_1 m_2$ is equal to one, while their ratio gives $1 + \sigma_{N_m}$. Thus, when the normalization of m_1 increases, that of m_2 decreases. The same result is obtained by multiplying the two measurements by $\sqrt{1 + \sigma_{N_m} r}$ and $\sqrt{1 - \sigma_{N_m} r}$ respectively. If we generalize to many measurements having a relative normalization uncertainty with each other, we obtain as an averaged effect an additional uncertainty on the measurements, see eq. (6.3.2). The

Figure 6.2. $\langle F_i \rangle_{rep}$ vs F_i and $r^{(art)}$ vs. $r^{(exp)}$ for the different structure functions with $N_{rep} = 10, 100$ and 1000 .

error introduced by the relative normalization uncertainties is $\sqrt{1 + \sigma_{N_m}} - 1 \sim \frac{1}{2}\sigma_{N_m}$.

We now address the problem of understanding how the central values, errors, and point-to-point correlations computed from the artificially generated data compare to the corresponding input experimental values, as a function of the number of generated replicas. A qualitative answer can be obtained from Fig. 6.2, where we show the scatter plots for mean values and correlations for the proton, the deuteron and the non-singlet structure functions. The reason why we take into account also the non-singlet structure function will be explained in the next section.

A more detailed description can be obtained by defining the following quantities:

- average over the number of replicas for each experimental point i (*i.e.* a pair of values of x and Q^2)

$$\langle F_i \rangle_{rep} = \frac{1}{N_{rep}} \sum_{k=1}^{N_{rep}} F_i^{(k)}. \quad (6.3.3)$$

The error on $\langle F_i \rangle_{rep}$ is given by

$$\sigma_i = \sqrt{\langle F_i^2 \rangle_{rep} - \langle F_i \rangle_{rep}^2}; \quad (6.3.4)$$

	F_2^p		
N_{rep}	10	100	1000
$\langle V \left[\langle F \rangle_{rep} \right] \rangle_{points}$	1.2×10^{-5}	1.4×10^{-6}	2.5×10^{-7}
$\langle PE \left[\langle F \rangle_{rep} \right] \rangle_{points}$	0.9%	0.3%	0.1%
$\tilde{r}[F]$	0.99966	0.99996	0.99999
$\langle V[\sigma] \rangle_{points}$	8.0×10^{-5}	2.4×10^{-5}	8.3×10^{-6}
$\langle PE[\sigma] \rangle_{points}$	41%	12%	4%
$\langle \sigma^{(art)} \rangle_{points}$	0.0114	0.0122	0.0122
$\tilde{r}[\sigma]$	0.859	0.988	0.999
$\langle V[r] \rangle_{points}$	0.0904	0.0072	0.0007
$\langle r^{(art)} \rangle_{points}$	0.364	0.321	0.319
$\tilde{r}[r]$	0.723	0.952	0.995
$\langle V[\text{cov}] \rangle_{points}$	5.4×10^{-9}	6.7×10^{-10}	5.6×10^{-11}
$\langle \text{cov}^{(art)} \rangle_{points}$	4.0×10^{-5}	4.0×10^{-5}	3.8×10^{-5}
$\tilde{r}[\text{cov}]$	0.529	0.891	0.987

Table 6.1. Comparison between experimental and generated artificial data for the proton structure function. Experimental data yield: $\langle \sigma^{exp} \rangle_{points} = 0.0123$, $\langle r^{exp} \rangle_{points} = 0.323$ and $\langle \text{cov}^{exp} \rangle_{points} = 3.9 \times 10^{-5}$.

the mean correlation between two points is given by

$$r_{ij} = \frac{\langle F_i F_j \rangle_{rep} - \langle F_i \rangle_{rep} \langle F_j \rangle_{rep}}{\sigma_i \sigma_j}; \quad (6.3.5)$$

- mean variance and mean percentage error on central values over the number of points N_{points}

$$\langle V \left[\langle F \rangle_{rep} \right] \rangle_{points} = \frac{1}{N_{points}} \sum_{i=1}^{N_{points}} \left(\langle F_i \rangle_{rep} - F_i \right)^2 \quad (6.3.6)$$

$$\langle PE \left[\langle F \rangle_{rep} \right] \rangle_{points} = \frac{1}{N_{points}} \sum_{i=1}^{N_{points}} \left| \frac{\langle F_i \rangle_{rep} - F_i}{F_i} \right|. \quad (6.3.7)$$

N_{rep}	F_2^d		
	10	100	1000
$\langle V \left[\langle F \rangle_{rep} \right] \rangle_{points}$	9.2×10^{-6}	9.1×10^{-7}	9.7×10^{-8}
$\langle PE \left[\langle F \rangle_{rep} \right] \rangle_{points}$	1.1%	0.3%	0.1%
$\tilde{r}[F]$	0.99976	0.99998	0.99999
$\langle V[\sigma] \rangle_{points}$	5.3×10^{-5}	1.5×10^{-5}	4.0×10^{-6}
$\langle PE[\sigma] \rangle_{points}$	39%	11%	3%
$\langle \sigma^{(art)} \rangle_{points}$	0.0095	0.0102	0.0102
$\tilde{r}[\sigma]$	0.857	0.990	0.999
$\langle V[r] \rangle_{points}$	0.0923	0.0075	0.0007
$\langle r^{(art)} \rangle_{points}$	0.374	0.310	0.310
$\tilde{r}[r]$	0.641	0.934	0.993
$\langle V[\text{cov}] \rangle_{points}$	2.6×10^{-9}	2.5×10^{-10}	2.3×10^{-11}
$\langle \text{cov}^{(art)} \rangle_{points}$	3.3×10^{-5}	3.3×10^{-5}	3.2×10^{-5}
$\tilde{r}[\text{cov}]$	0.568	0.932	0.992

Table 6.2. Comparison between experimental and generated artificial data for the deuteron structure function. Experimental data yield: $\langle \sigma^{exp} \rangle_{points} = 0.0102$, $\langle r^{exp} \rangle_{points} = 0.313$ and $\langle \text{cov}^{exp} \rangle_{points} = 3.3 \times 10^{-5}$.

$\langle V[\sigma] \rangle_{points}$, $\langle PE[\sigma] \rangle_{points}$, $\langle V[r] \rangle_{points}$ and $\langle V[\text{cov}] \rangle_{points}$ are defined in a similar way. These estimators indicate how close the averages over generated data are to the experimental values. Specifically, they will indicate if and how the slopes of the scatter plots in Fig. 6.2 differ from one;

- averaged correlation:

$$\tilde{r}[F] = \frac{\langle F \langle F \rangle_{rep} \rangle_{points} - \langle F \rangle_{points} \langle \langle F \rangle_{rep} \rangle_{points}}{\sigma^{(exp)} \sigma^{(art)}}. \quad (6.3.8)$$

Similarly we define $\tilde{r}[\sigma]$, $\tilde{r}[r]$ and $\tilde{r}[\text{cov}]$. This estimator indicates which is the spread of data around the *art. vs. exp.* line in the scatter plots of Fig. 6.2.

N_{rep}	$F_2^p - F_2^d$		
	10	100	1000
$\langle V \left[\langle F \rangle_{rep} \right] \rangle_{points}$	1.4×10^{-5}	1.8×10^{-6}	2.7×10^{-7}
$\langle PE \left[\langle F \rangle_{rep} \right] \rangle_{points}$	35%	11%	4%
$\tilde{r}[F]$	0.980	0.998	0.999
$\langle V[\sigma] \rangle_{points}$	6.6×10^{-5}	2.19×10^{-5}	7.8×10^{-6}
$\langle PE[\sigma] \rangle_{points}$	35%	12%	4%
$\langle \sigma^{(art)} \rangle_{points}$	0.0101	0.0114	0.0114
$\tilde{r}[\sigma]$	0.927	0.991	0.999
$\langle V[r] \rangle_{points}$	0.1133	0.0094	0.0010
$\langle r^{(art)} \rangle_{points}$	0.1112	0.0990	0.0946
$\tilde{r}[r]$	0.405	0.816	0.971
$\langle V[\text{cov}] \rangle_{points}$	5.1×10^{-9}	5.8×10^{-10}	6.0×10^{-11}
$\langle \text{cov}^{(art)} \rangle_{points}$	7.3×10^{-6}	9.0×10^{-6}	8.7×10^{-6}
$\tilde{r}[\text{cov}]$	0.346	0.791	0.972

Table 6.3. Comparison between experimental and generated artificial data for the non-singlet structure function. Experimental data yield: $\langle \sigma^{exp} \rangle_{points} = 0.0114$, $\langle r^{exp} \rangle_{points} = 0.090$ and $\langle \text{cov}^{exp} \rangle_{points} = 8.4 \times 10^{-5}$.

We expect *e.g.* the variance on central values to scale as $1/N_{rep}$, while the variance on the errors should scale as $1/\sqrt{N_{rep}}$ (see Appendix B.3). From Tables 6.1, 6.2 and 6.3 we see that this is approximately the case. Note that the exact scaling behavior is observed for $N_{rep} \sim 10^5$. We see also that one needs about 100 artificial data to get an accuracy at the percent level on central values, and about 1000 to get the same accuracy on errors and correlations.

6.4 Building and Training Neural Networks

We decided to fit separately F_2^p , F_2^d and $F_2^p - F_2^d$. Fitting the difference $F_2^p - F_2^d$ is safer than taking the difference of F_2^p and F_2^d after they have been fitted separately. Indeed, if we want a precision on $F_2^p - F_2^d$ of 10^{-2} , we must have a precision of at least 10^{-3} on F_2^p and F_2^d separately. However,

since the precision on F_2^p and F_2^d is 10^{-2} , in this way we would have a very poor precision, 10^{-1} , on $F_2^p - F_2^d$. The fit of $F_2^p - F_2^d$ is also delicate, as the non-singlet combination is very close to zero on a wide range of x , and errors are summed in quadrature; thus, lots of care must be taken to avoid fitting noise. The problem does not arise for the singlet combination $F_2^p + F_2^d$. In the following we outline the common features of the different fits, and then we will focus on details for each case.

We have constructed a neural network with the architecture (4,5,3,1), and we have used as inputs $x, Q^2, \log x$ and $\log Q^2$. The choice of taking $\log x$ and $\log Q^2$ as inputs does not introduce a theoretical bias, as the neural networks could “decide” to ignore these inputs if they are useless. One could even take as an input, say, a temperature, and if this variable is useless for fitting the given function the neural networks would have zero weights on the paths corresponding to this variable.

We have used sigmoid activation functions between the first three layers, while for the last layer we have chosen a linear activation function. As explained in the previous Chapter, this guarantees a smoother behavior of the neural network.

The number of units per layer has been chosen by trial-and-error, *i.e.* by adding a unit to a layer and looking for the stability of the output. In particular, we looked for the stability of correlation between central values by asking that it was more than 80%.

We have adopted the on-line training since the number of data is reasonably small. As we pointed out in the previous Chapter, it is worth pre-processing data in order to avoid fitting biases. In particular, we should not take data in the sequential given order, but it is better to pick them randomly. For this purpose we have used the `idirty` random number generator of Numerical Recipes [49] reported in Appendix C. Such a generator has a periodicity that may cause oscillations in the sampling of data. However, we have checked that oscillations due to the periodicity of the random number generator do not sensibly affect the fit.

The only theoretical assumption on the shape of F_2 has been the kinematic request $F_2(x = 1, Q^2) = 0$. This has been done by artificially adding 10 points at $x = 1$ with equally spaced values of Q^2 . The choice of the error on these points is very delicate, because if it is too small the neural networks would spend a lot of their training time in learning these points. One would obtain a very precise fit of the kinematical constraint $F_2(x = 1, Q^2) = 0$, and a worse fit of the experimental data. We have thus taken an error of the same order of the smallest experimental error. In particular, we have taken 10^{-3} for F_2^p and F_2^d where data are very different from zero within errors. For $F_2^p - F_2^d$ since the structure function is very close to zero, we have asked a higher precision on these points by setting the error equal to $\sqrt{2} 10^{-4}$.

As explained in Appendix B.4, the quantity we want to minimize in a fit is the *Covariance Matrix Estimator* (CME) given by

$$E[\mathbf{o}] \equiv \frac{1}{2} \sum_{\mu=1}^p \sum_{i,j=1}^m (o_i(\mathbf{x}^\mu) - z_i^\mu) V_{ij}^{-1} (o_j(\mathbf{x}^\mu) - z_j^\mu), \quad (6.4.1)$$

as in this way not only statistical errors, but also correlated systematic uncertainties are taken into account. The updating rules given in eq. (5.3.10) that govern the neural network learning, show that the variations on a single data point very weakly affect a given weight. Thus, to have a stronger effect we can switch to the batched training mode in which all the weights are updated after all patterns have been presented to enhance the effect of variations. However, the energy definition given in eq. (6.4.1) makes a sum over all patterns appears on the *r.h.s.* of the updating rule eq. (5.3.10) and its evaluation deeply affects the rapidity of the training. We can then minimize the simpler case where the energy is defined as the *Simplest χ^2 Estimator* (SCE),

$$E[\mathbf{o}] = \frac{1}{2} \sum_{\mu=1}^p \sum_{i=1}^m \left(\frac{o_i(\mathbf{x}^\mu) - z_i^\mu}{\sigma_i} \right)^2. \quad (6.4.2)$$

If systematic errors are not predominant with respect to the statistical ones, eq. (6.4.2) can be a good estimator of eq. (6.4.1) (see Appendix B.4). We will not take care of correlations when we fit each neural network to a replica of artificial data, since they are produced anyway by the Monte Carlo. In order to increase the efficiency of the training we can perform it in two cycles. First we minimize the error function eq. (5.3.5), and then we minimize eq. (6.4.2). This procedure corresponds to starting with a coarse search for the minimum, and then refining it once its neighborhood has been located. In the first example, for the first cycle we have used $\eta = 0.004$ and a number of epochs of 2×10^6 . For the second cycle we have taken $\eta = 4 \times 10^{-8}$ and a number of epochs of 4×10^6 . For every cycle the value of the momentum term was $\alpha = 0.9$. As the number of epochs is larger than 6×10^6 , every pattern may be seen at least 10^4 times. Henceforth we will label a training by a shorthand for the number of epochs of the second cycle; in the present case it is 4M.

As we have seen in the previous chapter, we expect neural networks to produce lower errors because they interpolate smoothly. Actually we expect them to reduce more the statistical errors than the systematic ones. An example is the problem of interpolating data randomly distributed around a horizontal line. If we fit these data with, say, a parabola, the result of the fit will be a parabola and not a horizontal line. If we instead take a set of neural networks, that do not have a definite functional behavior, we expect

that all distributions will have fits very similar and close to the horizontal line. Average over fits will give smaller errors to each point. If on top of the statistical error a global shift is added, then the fits will follow this shift. It is clear that infinite training will make the fit to go on top of each point and then all errors would be reproduced. But then the neural network is no longer assuming continuity or capacity of generalization. For that purpose a cubic spline fit would do the job.

The question which now we address is how the central values, errors, and point-to-point correlations computed from the neural networks compare to the corresponding data (experimental and artificial), both as a function of the number of replicas and of the length of the training, and both when comparing neural networks one by one, or their average. We then define the following quantities ($N_{rep} = N_{net}$):

- we define an averaged χ^2 over the number of points for practical reasons. As the number of points is of order 500 and the number of parameters is of order 50, this quantity differs for a 10% from the $\chi_{d.o.f.}^2$. In the last section we will show results also for $\chi_{d.o.f.}^2$. We thus define:

$$\chi_i^{2(net-art)} = \frac{1}{N_{net}} \sum_{k=1}^{N_{net}} \left(\frac{F_i^{(k,net)} - F_i^{(k,art)}}{\sigma_i} \right)^2, \quad (6.4.3)$$

$$\chi_i^{2(net-exp)} = \frac{1}{N_{net}} \sum_{k=1}^{N_{net}} \left(\frac{F_i^{(k,net)} - F_i^{(exp)}}{\sigma_i} \right)^2, \quad (6.4.4)$$

and

$$\chi_{SCE}^{2(net-art)} = \frac{1}{N_{points}} \sum_{i=1}^{N_{points}} \left(\frac{\langle F_i^{(net)} \rangle_{net} - \langle F_i^{(art)} \rangle_{net}}{\sigma_i} \right)^2 \quad (6.4.5)$$

$$\chi_{SCE}^{2(net-exp)} = \frac{1}{N_{points}} \sum_{i=1}^{N_{points}} \left(\frac{\langle F_i^{(net)} \rangle_{net} - F_i^{(exp)}}{\sigma_i} \right)^2, \quad (6.4.6)$$

where σ_i is the experimental statistical error; χ_{CME}^2 is defined in an analogous way with the inverse of the covariance matrix. In the following we will use always χ_{SCE}^2 , unless otherwise explicitly stated. The reason why we have given two different definition of χ^2 will become clear in the following. Note that the average of $\chi_i^{2(net-art,exp)}$ over the number of points gives a result different from $\chi^{2(net-art,exp)}$, *i.e.* the averages are not commutative. Specifically, $\chi_i^{2(net-art,exp)}$ indicate how each neural network fits the corresponding replica, while $\chi^{2(net-art,exp)}$ reflect the quality of the fit of experimental data or the average over the replicas as obtained from the average over the neural networks;

- *averaged correlation:*

$$\begin{aligned} \tilde{r}[F^{(net-art)}] &= \frac{1}{\sigma^{(net)} \sigma^{(art)}} \left[\left\langle \left\langle F^{(net)} \right\rangle_{net} \left\langle F^{(art)} \right\rangle_{net} \right\rangle_{points} \right. \\ &\quad \left. - \left\langle \left\langle F^{(net)} \right\rangle_{net} \right\rangle_{points} \left\langle \left\langle F^{(art)} \right\rangle_{net} \right\rangle_{points} \right]. \end{aligned} \quad (6.4.7)$$

Similarly we define $\tilde{r}[\sigma^{(net-art)}]$, $\tilde{r}[r^{(net-art)}]$ and $\tilde{r}[\text{cov}^{(net-art)}]$.

- variance and percentage error are defined as in the previous section with obvious replacements

As an example we first consider a training of 1000 neural networks on non-singlet data with the learning parameters discussed above. Results are collected in Table 6.4. First, we observe that one can reach a $\chi^2^{(net-exp)} \sim \chi^2^{(net-art)} \sim 1$ with an 80% correlation between neural networks and data (experimental or artificially generated), but the mean percentage error on the errors remains about 90%. The errors and correlations are only correlated to about 40%. Furthermore neural networks errors are systematically lower and correlations systematically higher by about a factor 4-5 than the experimental ones. Neural networks are producing a statistically good fit, but they are smoothing.

In order to understand whether the smoothing reproduces an underlying law or not, we will describe a toy model. Let us first consider a measured value m_i of F_2 where i represents a pair of values (x, Q^2) ; we have

$$m_i = t_i + \sigma_i s_i \quad (6.4.8)$$

where s_i is a univariate Gaussian number, t_i is the true value of F_2 , and σ_i its error. The k^{th} replica of generated data gives

$$g_i^{(k)} = m_i + r_k \sigma_i = t_i + (s_i + r_k) \sigma_i, \quad (6.4.9)$$

where r_k is a univariate Gaussian random number. If the neural networks succeed in finding the true value t_i with an error $\hat{\sigma}_i$ smaller than the experimental one, for the k^{th} neural network we have

$$n_i^{(k)} = t_i + r'_k \hat{\sigma}_i. \quad (6.4.10)$$

The variance between the neural networks values and the experimental data or the replicas is given by

$$\frac{1}{N_{rep}} \sum_{k=1}^{N_{rep}} \left(m_i - n_i^{(k)} \right)^2 = s_i^2 \sigma_i^2 + \hat{\sigma}_i^2. \quad (6.4.11)$$

$$\frac{1}{N_{rep}} \sum_{k=1}^{N_{rep}} \left(g_i^{(k)} - n_i^{(k)} \right)^2 = (1 + s_i^2) \sigma_i^2 + \hat{\sigma}_i^2, \quad (6.4.12)$$

N_{net}	$F_2^p - F_2^d$		
	NMC+BCDMS	NMC	BCDMS
$\chi_{SCE}^{2(net-exp)}$	0.97	0.57	1.41
$\left\langle \chi^{2(net-art)} \right\rangle_{points}$	2.05	1.64	2.50
$\left\langle \chi^{2(net-exp)} \right\rangle_{points}$	1.22	0.73	1.74
\mathcal{R}	0.60	0.45	0.70
$\tilde{r}[F^{(net-exp)}]$	0.85	0.74	0.96
$\left\langle PE[\sigma^{(net-exp)}] \right\rangle_{points}$	94%	95%	93%
$\left\langle \sigma^{(exp)} \right\rangle_{points}$	0.011	0.016	0.006
$\left\langle \sigma^{(net)} \right\rangle_{points}$	0.003	0.004	0.002
$\tilde{r}[\sigma^{(net-exp)}]$	0.33	0.16	0.49
$\left\langle r^{(exp)} \right\rangle_{points}$	0.09	0.04	0.16
$\left\langle r^{(net)} \right\rangle_{points}$	0.59	0.45	0.77
$\tilde{r}[r^{(net-exp)}]$	0.42	0.28	0.48
$\left\langle COV^{(exp)} \right\rangle_{points}$	8.4×10^{-6}	9.7×10^{-6}	6.8×10^{-6}
$\left\langle COV^{(net)} \right\rangle_{points}$	6.5×10^{-6}	7.6×10^{-6}	5.1×10^{-6}
$\tilde{r}[COV^{(net-exp)}]$	0.30	0.24	0.62

Table 6.4. Comparison between neural networks and experimental data for the non-singlet structure function with a 4M training.

If we now take the χ^2 divided by the number of points, we get

$$\left\langle \chi^{2(net-exp)} \right\rangle_{points} = \left\langle \left(\frac{m - n^{(k)}}{\sigma} \right)^2 \right\rangle_{points} = \langle \sigma^2 \rangle + \langle \hat{\sigma}^2 \rangle, \quad (6.4.13)$$

$$\left\langle \chi^{2(net-art)} \right\rangle_{points} = \left\langle \left(\frac{g^{(k)} - n^{(k)}}{\sigma} \right)^2 \right\rangle_{points} = 2\langle \sigma^2 \rangle + \langle \hat{\sigma}^2 \rangle.$$

The ratio yields

$$\mathcal{R} = \frac{1 + \frac{\langle \hat{\sigma}^2 \rangle}{\langle \sigma^2 \rangle}}{2 + \frac{\langle \hat{\sigma}^2 \rangle}{\langle \sigma^2 \rangle}}, \quad (6.4.14)$$

thus, $\mathcal{R} \approx \frac{1}{2}$ if $\langle \hat{\sigma} \rangle \ll \langle \sigma \rangle$. From Table 6.4 we have that $\langle \hat{\sigma} \rangle / \langle \sigma \rangle \approx 0.4$, and

$\mathcal{R} \approx 0.54$. As a consequence

$$\left\langle \chi^2(\text{net-exp}) \right\rangle_{\text{points}} \sim 2 \left\langle \chi^2(\text{net-art}) \right\rangle_{\text{points}}. \quad (6.4.15)$$

If we first take the average over the replicas and then the variance between the neural networks values and the replicas ones or the experimental data, we find

$$(m_i - \langle n_i \rangle_{\text{rep}})^2 = \sigma_i^2 s_i^2, \quad (\langle g_i \rangle_{\text{rep}} - \langle n_i \rangle_{\text{rep}})^2 = \sigma_i^2 s_i^2, \quad (6.4.16)$$

and

$$\chi^2(\text{net-exp}) = \chi^2(\text{net-art}) = 1. \quad (6.4.17)$$

Table 6.4 beautifully shows this behavior.

To understand why the error of neural networks can be smaller than the experimental one, and how we can recover this loss of information, as a toy model let us assume that the experimental data on F_2 satisfy an underlying linear law as a function of, say, the Bjorken variable x ,

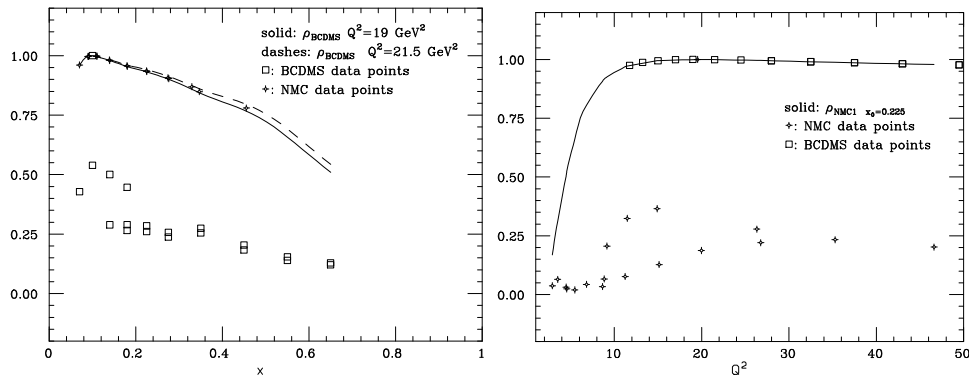
$$m_i = Cx_i + D. \quad (6.4.18)$$

Given $M + 2$ data points, two points will be sufficient to determine the linear parameters C and D , whose error is $\langle \sigma \rangle$. All the other points will only play the role of reducing the error on C and D by a factor $\frac{1}{\sqrt{M}}$ since they are all measurements of the same quantities C and D . If we take $\langle \hat{\sigma} \rangle = \frac{1}{\sqrt{M}} \langle \sigma \rangle$, from eq. (6.4.14) we have

$$\mathcal{R} = \frac{M+1}{M} \frac{M}{2M+1} = \frac{M+1}{2M+1} \geq \frac{1}{2}. \quad (6.4.19)$$

If $M = 0$, the neural networks obviously correlate a point only with itself, giving $\mathcal{R} = 1$ and an undefined uncertainty; if $M \rightarrow \infty$, the neural networks correlate all points giving a null error and $\mathcal{R} = 1/2$.

Obviously F_2 is neither a function of x only nor is it linear. Anyway the neural networks exhibit a finite correlation length $\sim \frac{1}{\sqrt{M}}$ and reduce the error on each point. Indeed, as $\langle \hat{\sigma} \rangle / \langle \sigma \rangle \approx 0.4$, we have that the neural networks correlate at about 10 points lowering their error at about by a factor 1/3. From Fig. 6.3 we see the way the neural networks behave. We have that BCDMS points coming from data sets with different beam energies, but with the same values of x and Q^2 are seen as the same point. On the other hand we see also that points of NMC and BCMDS that should have zero correlation between each other, are strongly correlated with all the points with similar values of x and Q^2 independently of the experiment.

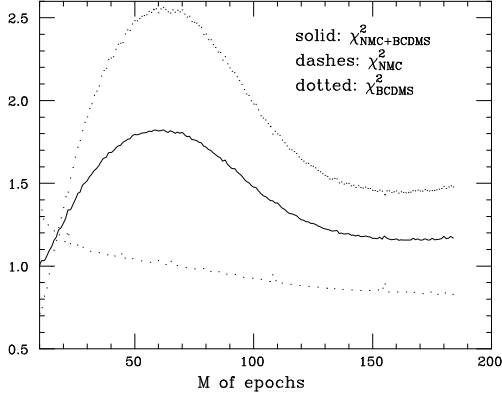
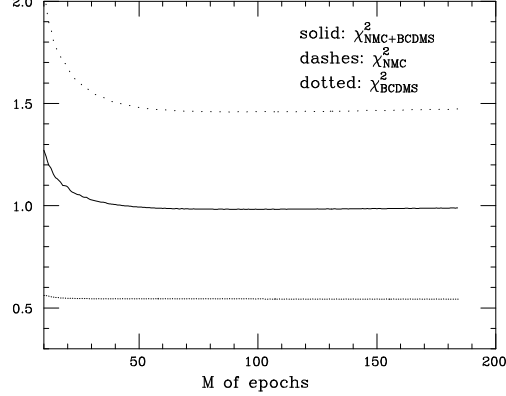

 Figure 6.3. Neural network correlation length for x and Q^2 .

6.4.1 Non-singlet

We now turn to specific details on the fit of the non-singlet structure function. From the short training example given in Table 6.4 we see that $\chi^2(\text{net-exp})$ for NMC is excellent (~ 0.6), but correlations and errors are very poorly reproduced, while $\chi^2(\text{net-exp})$ for BCDMS is good (~ 1.4), but not as good as for NMC, and correlations and errors are well reproduced. In order to better explain the neural networks behavior we will study the relative impact of the two experiments on the training of the neural networks. Here we will consider the training of only one neural network on the experimental data.

First we find that the length of the training on NMC does not improve errors and correlations for NMC. Then increasing the training for BCDMS one would expect to improve $\chi^2(\text{net-exp})$ for BCDMS while deteriorating $\chi^2(\text{net-exp})$ for NMC. However, while BCDMS does improve, NMC does not deteriorate. If we now fit the neural networks to BCDMS only plus the points at $x = 1$, we find that $\chi^2(\text{net-exp})$ for NMC is just as good as before. We conclude that the NMC points have essentially no impact on these fits: the corresponding central values are “predicted” by the neural networks fitted to BCDMS. Thus neural networks errors and correlations for NMC have nothing to do with their experimental values. The neural networks trained on both experiments only exploit the BCDMS data, while the NMC data have little or no impact on them.

We then address the problem of reducing $\chi^2(\text{net-exp})$ for BCDMS where the mediocre quality of the BCDMS fit is mostly due to the large x region that is not very well reproduced. Notice that if we increase the error on the points at $x = 1$, this does not help in making the fit of the remaining points easier (*i.e.* the $\chi^2(\text{net-exp})$ for the remaining points remains more or less the same). If we now increase the training, say at 40M, and keep fitting to


 Figure 6.4. *Training with BCDMS data.*

 Figure 6.5. *Training with NMC data.*

BCDMS only, the ability of the neural networks to predict NMC deteriorates very fast as $\chi^{2(net-exp)}$ for BCDMS improves. Roughly, when BCDMS is down to $\chi^{2(net-exp)} = 1$, NMC is already at $\chi^{2(net-exp)} = 2.6$.

However, it turns out that we could get an equally good fit for the two experiments by not excluding the NMC data completely, but also not showing them the same number of times as the BCDMS points (Fig. 6.6). We find that a rather long training (of order 150M) is required in order to get a good $\chi^{2(net-exp)}$ for BCDMS. We obtain a good equilibrium between the two experiments by showing the NMC data 10% of times. Specifically, with 180M training cycles, we get

$$\chi_{BCDMS}^{2(net-exp)} = \chi_{NMC}^{2(net-exp)} = \chi_{BCDMS+NMC}^{2(net-exp)} = 0.88. \quad (6.4.20)$$

In order to further understand the relative impact of the two experiments we can show some more fits. Specifically, to the fit training the neural network only on BCDMS data (Fig. 6.4), we add a fit training the neural network to NMC data only (plus the 10 points at $x = 1$), see Fig. 6.5. The interesting result is that in both cases the neural network trained on one data set successfully predicts the other data set. The $\chi^{2(net-exp)}$ of the predicted data set is in both cases about 1.5 after a long enough training. In particular the very bad behavior of the predicted NMC as the $\chi^{2(net-exp)}$ for BCDMS improves is a feature of short-medium training, 40M, as the training goes on also the predicted NMC improves again. Thus, the neural network can use either of the two experiments to predict the other one. Of course, if the experiment with smaller errors is used to train the neural network, the other one is predicted also with smaller error. In order to show the relevance of the fitting procedure, where the NMC data are only shown 10% of times, we can now consider the training where data are given equal weight, but letting it run for a very long training, 1000M training epochs, see Fig. 6.7.

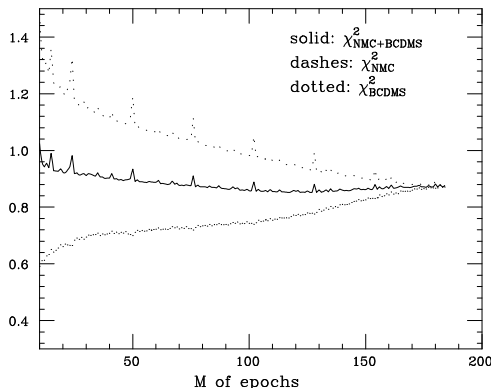


Figure 6.6. Training with BCDMS data and 10% of times with NMC data

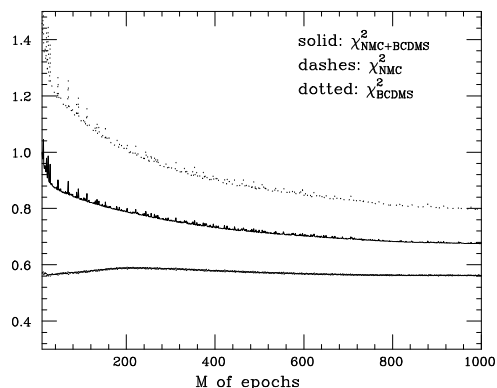


Figure 6.7. Long training with NMC and BCDMS data with equal weight

We see that the BCDMS $\chi^{2(\text{net-exp})}$ does improve constantly, so that also in this case the $\chi^{2(\text{net-exp})}$ for the two experiments would eventually intersect for long enough training. However, this way of training is both inefficient (it takes very long to find the intersection) and also subject to the criticism that at the intersection point the neural network is almost certainly over-learning (presumably at the intersection $\chi^2 \sim 0.6$). So training to NMC only 10% of times is a trick which helps both in making the training faster, and in obtaining the same $\chi^{2(\text{net-exp})}$ for the two experiments at a value where there is no over-learning yet.

Finally, we look again at the good training, *i.e.* 180M and 10% of times on NMC. As we have noted already the $\chi^{2(\text{net-exp})}$ for the average over the neural networks is good and essentially equal for both experiments. The errors and correlations are well reproduced for BCDMS, but very poorly for NMC (no correlation between neural networks average and data and so on). The reason why the errors and correlations are poorly reproduced for NMC is that that the local information provided by each NMC data point is very weak, and individual NMC points carry little information on the shape of F_2 . In other words, a few NMC points are sufficient to train the neural network and the remaining ones do not provide significant extra information. As a consequence, the values of error and correlations for each individual point (or pair of points) have little or no impact on the neural network. This fact can be seen in the fit where we use all BCDMS data, but only 20 NMC points (7% of NMC points arbitrarily chosen among those where the systematics is less than the statistical error), Fig. 6.8. This fit is as good as the fit where all NMC data are kept.

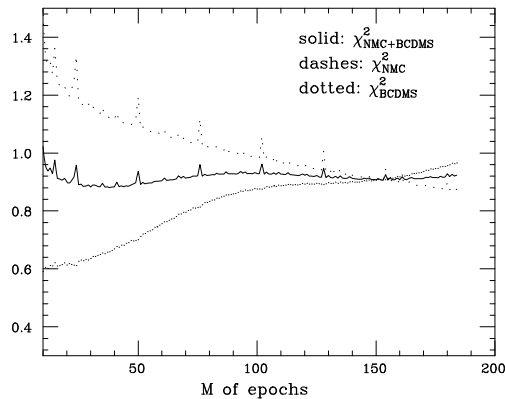


Figure 6.8. Training with BCDMS data and 20 points of NMC

6.4.2 Proton and Deuteron

Fits of proton and deuteron structure functions are more complicated. Here we will outline only some interesting features. Tables 6.5 and 6.6 show the results for a 10M training of 100 neural networks for the two structure functions. We have used the same learning parameters for the non-singlet structure function fit, while the number of epochs on the first cycle has been taken equal to 4.6×10^6 . The data sets of the two experiments have been shown an equal number of times.

First we observe that the behavior of neural networks is approximately the same for F_2^p and F_2^d . We note also that there are differences from the fit of $F_2^p - F_2^d$. Indeed, the ratio \mathcal{R} for the two experiments is of order 1. Specifically, we have that $\mathcal{R}_{NMC} = 0.77$ and $\mathcal{R}_{BCDMS} = 1.51$ for the proton and $\mathcal{R}_{NMC} = 0.84$ and $\mathcal{R}_{BCDMS} = 1.05$ for the deuteron. This means that while for NMC the neural networks perform a smoothing, for BCDMS they do not. In particular, we find that the neural network errors for NMC are smaller than the experimental ones, while correlations are larger. However, their ratio is smaller than in the non-singlet case. Thus, neural networks are smoothing, but less than in the non-singlet case. For BCDMS neural network errors and correlations are very close to the experimental ones showing that no additional correlation has been added. BCDMS data are all necessary to constraint the neural network behavior. Some other features can be summarized as follows:

- when we increase the training for both the proton and the deuteron, χ_{BCDMS}^2 always decreases (it can become less than 1), while χ_{NMC}^2 , although initially decreases faster, saturates at a value of about 1.3 for the proton and 1.2 for the deuteron;

- for both the proton and the deuteron χ_{NMC}^2 is already minimized by the first cycle; it very little decreases with the second cycle, and sometimes if the learning rate is too large (order 10^{-8}) it increases. The situation is the same if we fit only NMC excluding BCDMS data points;
- systematic correlated errors do not play a significant role, as χ_{CME}^2 is not much less than χ_{SCE}^2 ;
- correlations for central values, errors and correlations, are better than in the non-singlet case, although here we have only 100 neural networks; the scatter plots in Figs. 6.9 and 6.10 show that for both the proton and the deuteron we have a good agreement on central values. However, the statistical experimental errors are very small compared with the differences between the experimental values and the fitted ones, and this is why the χ^2 is still bad although all the other estimators are good.

6.5 Results

We consider the case of neural networks trained over 1000 replicas of the experimental data. The learning parameters are the same used in the previous examples, *i.e.* $\eta = 0.004$ for the first cycle, $\eta = 4 \times 10^{-8}$ for the second, the momentum term $\alpha = 0.9$. We have trained the neural networks 4.6×10^6 times for the first cycle, 180×10^6 for the second one. We have shown the NMC data 10% of times. As we have discussed in the previous Section, this is only a trick to improve the training time. Results for the non-singlet structure function are collected in Table 6.7. We observe that:

- $\chi_{CME}^2 \leq 1$ for each experiment, *i.e.* our fit differs from data for less than one standard deviation, even properly keeping into account correlations between systematic uncertainties. The same result occurs if we consider the $\chi_{d.o.f.}^2$ whose values are collected in Table 6.8. As we have used 552 experimental points and 47 parameters (38 weights and 9 thresholds), the number of *degrees of freedom* is 505;
- central values are correlated each other at the level of 81%; the fit over BCDMS data is more correlated (95%) than that of NMC data (69%), according to what we have shown in the previous section;
- the loss of information due to the smaller error given by neural networks is regained in the increasing of correlations. As we have shown this effect is due to the ability of neural networks of finding an underlying law, $\mathcal{R} = 0.58$;

- the mean value of the covariance between data points is approximately the same for the fit over NMC and NMC+BCDMS data, while it is exactly the same for BCDMS data.

Results for proton and deuteron structure functions are forthcoming. Once they are ready, they will be available through a package to be embedded in a code for practical purposes. A web site will also be realized for an on-line distribution of the fitted data.

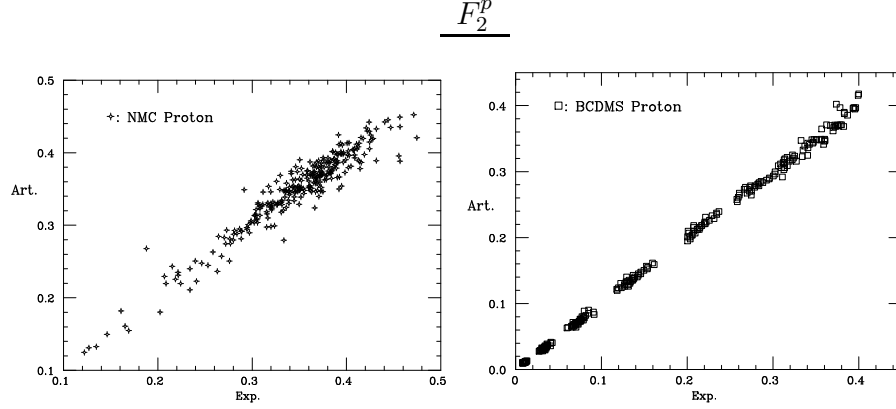


Figure 6.9. Comparison between neural networks and experimental data for the proton structure function with a 10M training.

N_{net}	NMC+BCDMS	NMC	BCDMS
$\chi_{SCE}^{2(net-exp)}$	1.48	1.53	1.43
$\chi_{CME}^{2(net-exp)}$	1.38	1.44	1.31
$\left\langle \chi^2(net-art) \right\rangle_{points}$	3.01	3.22	2.78
$\left\langle \chi^2(net-exp) \right\rangle_{points}$	3.30	2.49	4.19
\mathcal{R}	1.10	0.77	1.51
$\tilde{r}[F^{(net-exp)}]$	0.995	0.959	0.999
$\left\langle PE[\sigma^{(net-exp)}] \right\rangle_{points}$	59%	73%	44%
$\left\langle \sigma^{(exp)} \right\rangle_{points}$	0.012	0.017	0.007
$\left\langle \sigma^{(net)} \right\rangle_{points}$	0.006	0.008	0.005
$\tilde{r}[\sigma^{(net-exp)}]$	0.51	0.09	0.92
$\left\langle r^{(exp)} \right\rangle_{points}$	0.32	0.17	0.52
$\left\langle r^{(net)} \right\rangle_{points}$	0.64	0.54	0.76
$\tilde{r}[r^{(net-exp)}]$	0.59	0.32	0.77
$\left\langle COV^{(exp)} \right\rangle_{points}$	3.9×10^{-5}	4.5×10^{-5}	3.3×10^{-5}
$\left\langle COV^{(net)} \right\rangle_{points}$	2.7×10^{-5}	3.0×10^{-5}	2.3×10^{-5}
$\tilde{r}[COV^{(net-exp)}]$	0.67	0.57	0.92

Table 6.5. Comparison between neural networks and experimental data for the proton structure function with a 10M training.

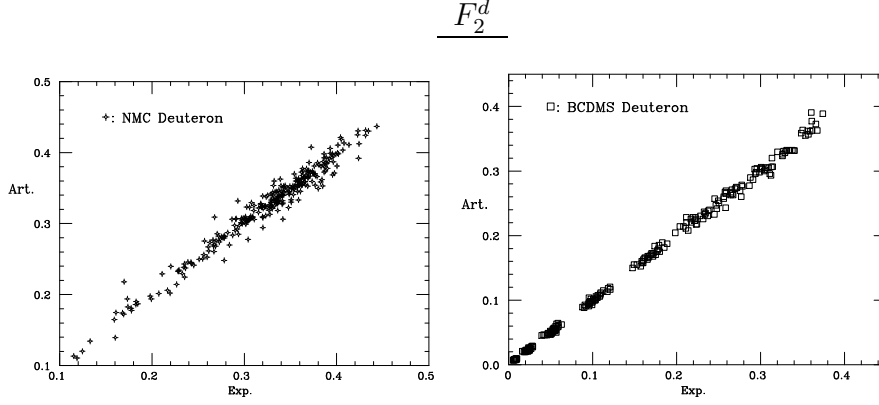


Figure 6.10. Comparison between neural networks and experimental data for the deuteron structure function with a 10M training.

N_{net}	NMC+BCDMS	NMC	BCDMS
$\chi_{SCE}^{2(net-exp)}$	1.30	1.42	1.16
$\chi_{CME}^{2(net-exp)}$	1.25	1.33	1.16
$\left\langle \chi^2(net-art) \right\rangle_{points}$	3.01	3.40	2.58
$\left\langle \chi^2(net-exp) \right\rangle_{points}$	2.78	2.84	2.72
\mathcal{R}	0.93	0.84	1.05
$\tilde{r}[F^{(net-exp)}]$	0.997	0.985	0.999
$\left\langle PE[\sigma^{(net-exp)}] \right\rangle_{points}$	61%	69%	52%
$\left\langle \sigma^{(exp)} \right\rangle_{points}$	0.010	0.014	0.006
$\left\langle \sigma^{(net)} \right\rangle_{points}$	0.006	0.007	0.004
$\tilde{r}[\sigma^{(net-exp)}]$	0.67	0.31	0.93
$\left\langle r^{(exp)} \right\rangle_{points}$	0.31	0.22	0.43
$\left\langle r^{(net)} \right\rangle_{points}$	0.61	0.55	0.69
$\tilde{r}[r^{(net-exp)}]$	0.48	0.27	0.66
$\left\langle \text{COV}^{(exp)} \right\rangle_{points}$	3.3×10^{-5}	4.0×10^{-5}	2.2×10^{-5}
$\left\langle \text{COV}^{(net)} \right\rangle_{points}$	2.0×10^{-5}	2.6×10^{-5}	1.3×10^{-5}
$\tilde{r}[\text{COV}^{(net-exp)}]$	0.69	0.62	0.88

Table 6.6. Comparison between neural networks and experimental data for the deuteron structure function with a 10M training.

N_{net}	$F_2^p - F_2^d$		
	NMC+BCDMS	NMC	BCDMS
$\chi_{SCE}^{2(net-exp)}$	0.83	0.80	0.86
$\chi_{CME}^{2(net-exp)}$	0.79	0.78	0.80
$\langle \chi^{2(net-art)} \rangle_{points}$	1.95	2.00	1.89
$\langle \chi^{2(net-exp)} \rangle_{points}$	1.14	1.05	1.25
\mathcal{R}	0.58	0.53	0.66
$\tilde{r} [F^{(net-exp)}]$	0.81	0.69	0.95
$\langle V[\sigma^{(net-exp)}] \rangle_{points}$	1.7×10^{-4}	2.9×10^{-4}	3.5×10^{-5}
$\langle PE[\sigma^{(net-exp)}] \rangle_{points}$	80%	82%	77%
$\langle \sigma^{(exp)} \rangle_{points}$	0.011	0.016	0.006
$\langle \sigma^{(net)} \rangle_{points}$	0.004	0.005	0.003
$\tilde{r}[\sigma^{(net-exp)}]$	0.50	-0.02	0.92
$\langle V[r^{(net-exp)}] \rangle_{points}$	0.34	0.33	0.35
$\langle r^{(exp)} \rangle_{points}$	0.09	0.04	0.16
$\langle r^{(net)} \rangle_{points}$	0.57	0.45	0.73
$\tilde{r}[r^{(net-exp)}]$	0.37	0.12	0.56
$\langle V[\text{cov}^{(net-exp)}] \rangle_{points}$	9.7×10^{-10}	1.7×10^{-9}	2.1×10^{-11}
$\langle \text{cov}^{(exp)} \rangle_{points}$	8.4×10^{-6}	9.7×10^{-6}	6.8×10^{-6}
$\langle \text{cov}^{(net)} \rangle_{points}$	9.0×10^{-6}	1.1×10^{-5}	6.8×10^{-6}
$\tilde{r}[\text{cov}^{(net-exp)}]$	0.26	0.21	0.86

Table 6.7. Comparison between neural networks and experimental data for the non-singlet structure function with a 180M training.

	NMC+BCDMS	NMC	BCDMS
SCE	0.91	0.96	1.04
CME	0.86	0.93	0.97

Table 6.8. $\chi_{d.o.f.}^2$ for SCE and CME with 505 degrees of freedom for all the experimental points, and for each experiment.

7

Determination of α_s with truncated moments

The strong coupling constant α_s is the only free parameter in the QCD Lagrangian, and more and more accuracy is needed in its determination. As shown in Fig. 7.1 there are several experimental processes from which we can extract α_s . Deep inelastic scattering is one of the prime ways of determining the strong coupling constant α_s .

Here we will show how the technique of truncated moments can be used for a determination of the strong coupling constant by keeping under control theoretical biases. We will take the fit of the non-singlet structure function given in the previous Chapter to obtain the truncated moments of the non-singlet parton distribution at the initial and the final scale. Then the value of α_s will be extracted from the evolution of truncated moments [51].

7.1 The DIS phenomenology

In this Section we will complete the phenomenology of Deep Inelastic Scattering processes introduced in Chapter 3. Specifically, we will introduce and describe possible effects of theoretical uncertainty, and the techniques we adopt to keep them under control.

7.1.1 Target Mass Corrections

Within the operator product expansion [52] the structure functions are given by the sum of contributions coming from operators of different twists. For unpolarized lepton scattering only even twists larger or equal to two contribute. Thus keeping the twist-4 contributions into account, we have

$$F_2(x, Q^2) = F_2^{\text{LT,TMC}}(x, Q^2) + \frac{H(x)}{Q^2}, \quad (7.1.1)$$

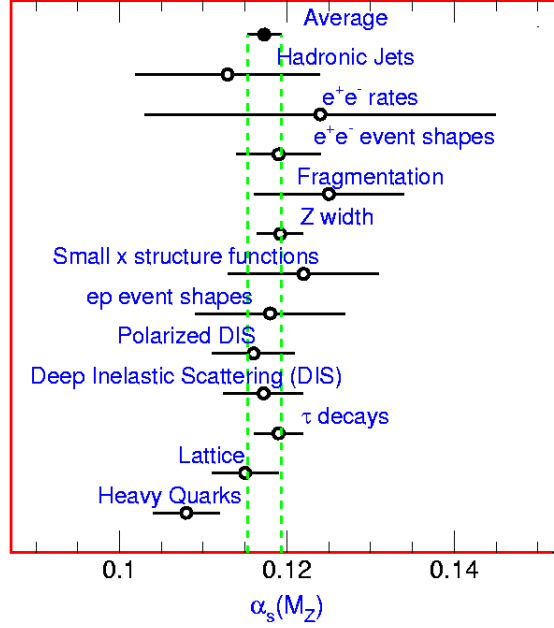


Table 7.1. Present status of the determination of α_s as given in Ref. [50].

where $F_{2,L}^{\text{LT,TMC}}$ gives the leading twist (LT) including target mass corrections, as calculated in Ref. [53]:

$$\begin{aligned}
 F_{2,L}^{\text{LT,TMC}}(x, Q^2) &= \frac{x^2}{r^3} F_2(\xi, Q^2) + 6 \frac{m^2 x^3}{Q^2 r^4} \int_{\xi}^1 d\xi' F_2(\xi', Q^2) \\
 &+ 12 \frac{m^4 x^4}{Q^4 r^5} \int_{\xi}^1 d\xi' \int_{\xi'}^1 d\xi'' F_2(\xi'', Q^2), \quad (7.1.2)
 \end{aligned}$$

where

$$\xi = \frac{2x}{1 + \sqrt{r}}, \quad r = \sqrt{1 + \frac{4x^2 m^2}{Q^2}} \quad (7.1.3)$$

and F_2 is the structure function of twist 2 eq. (3.2.11). This approach allows us to separate pure kinematical corrections, so that the functions $H(x)$ correspond to “genuine” or “dynamical” contribution of the twist 4 operators.

There is a well-known difficulty in eqs. (7.1.2) at $x = 1$ (see *e.g.* discussion and references in [54]): in fact, when $x = 1$ the structure functions should vanish for kinematical reasons, while the *r.h.s.* of eq. (7.1.2) is clearly nonzero, since $\xi(x = 1) < 1$. Indeed, in the large x region dynamical higher twist corrections become important and cannot be neglected any more. This is

because the twist $2+2k$ contribution to the n^{th} moment of a generic structure function has the form

$$B_{kn}(Q^2) \left(\frac{n\Lambda^2}{Q^2} \right)^k, \quad (7.1.4)$$

where Λ is a mass scale of the order of a few hundreds MeV, and the coefficients $B_{kn}(Q^2)$ have no power dependence on n, k or Q^2 . The crucial feature of eq. (7.1.4) is the presence of a factor n^k , which arises because there are at least n twist $2+2k$ operators of a given dimension for each leading twist operator of the same dimension. One can prove that the behavior of structure functions in the $x \sim 1$ region is governed by moments $n = \mathcal{O}(Q^2/m^2)$; in fact, when $x = 1$ and $m^2/Q^2 \ll 1$ we have

$$\xi \simeq 1 - \frac{m^2}{Q^2}; \quad (7.1.5)$$

on the other hand, if we assume a $(1-\xi)^{a_2}$ behavior for the structure function, with a_2 of order 1, its n^{th} moment receives the dominant contribution from the region

$$\xi \simeq \frac{n}{a_2 + n} \simeq 1 - \frac{a_2}{n}. \quad (7.1.6)$$

Comparing eqs. (7.1.5) and (7.1.6), we obtain that the relevant moments for the $x = 1$ region are of order

$$n = \frac{a_2 Q^2}{m^2} \quad (7.1.7)$$

as announced. Inserting this in eq. (7.1.4), one immediately realizes that the contribution of dynamical higher twists is no longer suppressed by inverse powers of Q^2 when x is close to 1, and we cannot expect eqs. (7.1.1) and (7.1.2), to hold in this region. A solution to this problem is that of expanding the result in powers of m^2/Q^2 up to any finite order. In this way, the dangerous contribution of terms with large powers of m^2/Q^2 is not included. The expansion remains reliable even when Q^2 is as low as m^2 , provided x is not too large; in fact, powers of m^2/Q^2 always appear multiplied by an equal power of x^2 . The expanded result of course cannot be reliable at $x \simeq 1$, but this would not be the case even without expanding in m^2/Q^2 , since we are not including the contributions of eq. (7.1.4), which are important in this region.

There are several attempts to give a theoretical estimation of dynamical HT (see *e.g.* [55]), as well as to extract HT contribution from data taken at low Q^2 (see *e.g.* [56]). Meanwhile, due to the fast fall of the HT contribution with Q^2 , it is significant for $Q^2 \leq 10 \text{ GeV}^2$ only. Thus, if we choose a kinematic range given by $x_0 = 0.01$ and $Q^2 \geq 20 \text{ GeV}^2$, target mass corrections and dynamical HT will be numerically negligible, even in the large- x limit.

7.1.2 Renormalization and factorization scales

As we have seen in Sect. 3.2 F_2 is given by the convolution of coefficient functions and parton distributions which both depend on a factorization scale μ_F^2 . A dependence on the renormalization scale μ_R^2 is introduced by NLO QCD approximation of α_s and by the NLO splitting functions, when we consider the scale evolution of parton distributions with the Altarelli-Parisi equations. Since we use the truncated perturbative series, the results depend on the factorization scale μ_F^2 and the renormalization scale μ_R^2 .

Only a limited set of Mellin moments of the NNLO Altarelli-Parisi splitting functions [57], as well as some asymptotes, are known [58]. Nevertheless, there are attempts to analyze the DIS data in the NNLO QCD approximation considering the available moments only [59], or modeling splitting functions [60]. Our analysis is performed in the NLO QCD approximation with the use of the splitting and coefficient functions in x -space as they are given in Refs. [15, 18], and the DIS scheme change given in [29]. We also set $\mu_F^2 = \mu_R^2 = Q^2$.

Since we work in the DIS factorization scheme F_2 is given by eq. (3.4.18). The parton distributions are defined at the physical scale of F_2 , and the factorization scale is identified with the renormalization scale. As we will consider only the non-singlet structure function, we will not need a prescription for the gluon (see Sects. 3.4.1 and 4.3). We are then left to estimate the theoretical uncertainty due to the choice of μ_R^2 in the evolution equations. This will be done using the approach described in Ref. [61]. In accordance with this approach the renormalization scale μ_R^2 is chosen equal to $k_R Q^2$. The effect of a variation of the scale at LO in α_s is given by

$$\begin{aligned} \alpha_s(k_R Q^2) &= \frac{\alpha_s(M_Z^2)}{1 + \frac{b_0}{2\pi} \alpha_s(M_Z^2) \log \frac{k_R Q^2}{M_Z^2}} \\ &\approx \alpha_s(Q^2) - \frac{b_0}{2\pi} \alpha_s^2 \log k_R. \end{aligned} \quad (7.1.8)$$

Thus, the NLO evolution equations are modified in the following way

$$\begin{aligned} \frac{d}{dt} q^{(NS)}(x, k_R Q^2) &= \\ \frac{\alpha_s(t)}{2\pi} \left[P_{qq}^{(0)} + \frac{\alpha_s(t)}{2\pi} (P_{qq}^{(1)} - b_0 P_{qq}^{(0)} \log k_R) \right] \otimes q^{(NS)}(x, Q^2). \end{aligned} \quad (7.1.9)$$

where $P^{(0)}$ and $P^{(1)}$ are respectively the LO and NLO splitting functions. This contribution can be compensated at NLO by a redefinition of the NLO splitting function

$$P_{qq}^{(1)} \rightarrow P_{qq}^{(1)} + b_0 P_{qq}^{(0)} \log k_R. \quad (7.1.10)$$

In the following analysis we will take a variation of k_R from 1/4 to 4 which gives an estimate of the error due to renormalization scale uncertainty. By definition, this uncertainty is connected with the impact of higher order terms of the perturbative series.

7.1.3 Elastic contribution

Elastic contributions are taken into account with the nucleon structure function, *e.g.* of the proton, given by [62]

$$F_2^{(el)}(x, Q^2) = \frac{G_E^2 + G_M^2 \tau}{1 + \tau} \frac{1}{(1 + Q^2 r_0^2)^4} \delta(x - 1), \quad (7.1.11)$$

where G_E and G_M are the elastic form factors, $\tau = Q^2/4M^2$ with M the proton mass, $r_0 = 1/0.71 \text{ GeV}^{-2}$ is the scale of the proton radius.

This contribution may be significant in our analysis thus spoiling its accuracy. Indeed, if we take the lower integration bound of truncated moments to be large, and we fit a higher moment, the elastic contribution to the fitted truncated moment may reach 20%. To make this effect negligible we will consider only the fit of the first 10 moments.

7.1.4 Evolution uncertainties

In Sect. 4.4, we have given an estimation of the theoretical uncertainty introduced by truncated moments. There we used a toy model PDF to have an upper bound on these uncertainties. Here we reproduce those checks for the non-singlet PDF for all moments that will be considered in our analysis. As the input PDF we take the one obtained from the neural networks fit of F_2 discussed in the previous Chapter. In the DIS factorization scheme we have

$$q^{NS}(x, Q^2) = 2 \frac{F_2^p(x, Q^2) - F_2^d(x, Q^2)}{x}. \quad (7.1.12)$$

In Table 7.2 we show the percentage errors on the *r.h.s.* of the LO evolution equations for $x_0 = 0.1$ that exhibits the largest errors on the evolution. As expected the values of the percentage errors are less than those given with the toy PDF, even if of the same order and higher moments have negligible errors on their evolution. We checked that the results hold also at NLO. The value of x_0 that we will use for our final analysis is $x_0 = 0.01$. In this case even for the fitted non-singlet PDF, we have $\mathcal{R}_{n,M}^a \sim \mathcal{R}_{n,M,N}^b \sim 0.1\%$ as reported in Table 4.5.

$x_0 = 0.1$		
n	$\mathcal{R}_{n,11}^a$	$\mathcal{R}_{n,11,6}^b$
1	4.5×10^{-1}	5.4×10^{-2}
2	9.9×10^{-2}	1.3×10^{-2}
3	1.9×10^{-2}	5.7×10^{-3}
4	3.2×10^{-3}	1.3×10^{-3}
5	5.1×10^{-4}	2.4×10^{-4}
6	7.5×10^{-5}	3.9×10^{-5}
7	1.0×10^{-5}	5.7×10^{-6}
8	1.4×10^{-6}	7.9×10^{-7}
9	1.8×10^{-7}	1.1×10^{-7}
10	2.3×10^{-8}	1.4×10^{-8}
11	2.8×10^{-9}	1.7×10^{-9}

Table 7.2. Comparison between percentage errors on the LO evolution equation for $M = 11$ and $N = 6$.

7.2 Fitting procedure and results

The technique of truncated moments requires a high numerical precision in the computation of the evolution matrices (see Sect. 4.4). Thus, the following results are obtained with 11 truncated moments, *i.e.* the maximum number of truncated moments we can use to avoid numerical uncertainties on the evolution. The evolution is performed between an initial scale of 20 GeV^2 and a final scale of 70 GeV^2 . A logarithmically equally spaced intermediate scale is used. Details on these choices will be discussed at the end of the section. We will show both results with $x_0 = 0.01$ and $x_0 = 0.1$. We checked that with $x_0 = 0.1$ higher twists effects as well as elastic contributions are negligible. We do not take into account the fit of the first truncated moment. This is because the exact first Mellin moment does not evolve and does not affect a fit of α_s . The same holds for the first truncated moment with a small value of x_0 . We also observe that the percentage error on the evolution of the first truncated moment is significant for large values of x_0 , thus spoiling the precision of our analysis.

We generate truncated moments of the LO and NLO splitting functions, as well as the matrices R and R^{-1} that diagonalize the evolution equation given in eq. (4.4.27), with a *Mathematica* code [63]. Results are passed to a FORTRAN code that reads the parameters of the neural network fit of F_2 and that performs the minimization of the χ^2 with the MINUIT routine [64]. The errors on α_s reported in this section are the statistical errors given by MINUIT.

We will start our analysis by fitting α_s and a single truncated moment.

n	α_s	
	$x_0 = 0.1$	$x_0 = 0.01$
2	0.0914 ± 0.0469	0.0886 ± 0.0798
3	0.1002 ± 0.0240	0.1059 ± 0.0311
4	0.1131 ± 0.0187	0.1153 ± 0.0193
5	0.1222 ± 0.0151	0.1225 ± 0.0153
6	0.1266 ± 0.0142	0.1266 ± 0.0142
7	0.1286 ± 0.0146	0.1286 ± 0.0146
8	0.1294 ± 0.0160	0.1294 ± 0.0160
9	0.1292 ± 0.0184	0.1292 ± 0.0184
10	0.1282 ± 0.0217	0.1282 ± 0.0217
11	0.1264 ± 0.0260	0.1264 ± 0.0260

Table 7.3. Values of the fitted $\alpha_s(M_Z^2)$ for the fit with a single moment for different values of x_0 .

$x_0 = 0.1$	
Fitted moments	α_s
3+4	0.1369 ± 0.0106
3+5	0.1360 ± 0.0115
3+6	0.1337 ± 0.0125
3+7	0.1306 ± 0.0135
3+8	0.1273 ± 0.0143

Table 7.4. Values of the fitted $\alpha_s(M_Z^2)$ for the fit with a pair of moments.

From Table 7.3 we first observe that all central values, whenever different from the world average, are compatible with it at least within 1σ . We see also that lower moments have a central value lower than 0.119 and large errors. The error is minimum for $n = 6$. As we expect, higher truncated moments are independent from the lower integration bound x_0 . In the chosen kinematic range from eq. (7.1.6) we have

$$x \simeq \frac{n}{a_2 + n} \simeq 1 - \frac{a_2}{n}. \quad (7.2.1)$$

Thus, only the lower truncated moments are sensitive to the small- x region. Notice that if we fit a single truncated moment we can not take into account all the available information we have from data.

Let us consider a fit of pairs of moments. As an example, we have collected results with $x_0 = 0.1$ in Table 7.4. We observe that α_s obtained by fitting simultaneously two truncated moments slightly differs from the weighted average of the α_s given by the case in which we fit the corresponding truncated

$x_0 = 0.2$	
Fitted moments	α_s
2+4+5	0.1099 ± 0.0079
3+5+7	0.1169 ± 0.0079
2+5+7	0.1130 ± 0.0079
2+3+4	0.0949 ± 0.0081
3+6+9	0.1152 ± 0.0092
2+4+5+6	0.1046 ± 0.0077
2+3+5+7	0.0874 ± 0.0100

Table 7.5. Values of the fitted $\alpha_s(M_Z^2)$ for the fit with different combinations of moments.

$x_0 = 0.1$	
Fitted moments	α_s
2+3+4	0.1279 ± 0.0082
2+3+5	0.1188 ± 0.0097
2+4+5	0.1214 ± 0.0104
2+4+6	0.1200 ± 0.0104
3+4+5	0.1202 ± 0.0117
3+5+7	0.1207 ± 0.0153
2+3+4+5	0.1160 ± 0.0067
2+4+5+6	0.0953 ± 0.0096

Table 7.6. Values of the fitted $\alpha_s(M_Z^2)$ for the fit with different combinations of moments.

moments one by one. The central values are different and the errors are smaller. Thus correlations play an important role. As we expect, the effect of correlations is higher for neighboring moments, while it is smaller for distant ones. In particular, we have that if moments are weakly correlated the fit is closer to the fit of the single more precise moment. We have checked that this behavior is independent of the chosen value of x_0 .

Results for different combination of fitted moments are given in Tables 7.5, 7.6 and 7.7. In this case we also show for completeness the results for $x_0 = 0.2$ that is close to the x cut of the fit given in [65]. At first sight we note that we have the smallest error on α_s when the number of fitted moments is the largest, *i.e.* $x_0 = 0.01$ and 6 or 7 truncated moments. However, from Table 7.7 we observe also that there is a trade-off due to the fact that we have a limited amount of information: 6 truncated moments and 3 scales is the number of parameters sufficient to extract the whole information from data. Increasing the number of parameters does not improve the fit.

$x_0 = 0.01$	
Fitted moments	α_s
3+6+9	0.1395 ± 0.0096
2+5+7	0.1352 ± 0.0097
2+3+4	0.1301 ± 0.0105
3+5+7+9	0.1248 ± 0.0074
3+4+6+8	0.1200 ± 0.0082
2+4+6+8	0.1207 ± 0.0097
2+3+5+7	0.1350 ± 0.0121
3+5+6+7+8	0.1271 ± 0.0050
2+3+5+6+7	0.1284 ± 0.0051
3+5+6+7+9	0.1272 ± 0.0051
2+3+5+7+9	0.1279 ± 0.0059
3+4+5+7+9	0.1261 ± 0.0060
2+3+4+6+8	0.1264 ± 0.0107
2+3+4+5+6+7	0.1279 ± 0.0047
2+4+5+6+7+9	0.1281 ± 0.0049
2+3+4+5+6+8	0.1281 ± 0.0049
1+3+4+5+6+9	0.1279 ± 0.0051
1+2+4+5+6+7	0.1243 ± 0.0055
2+3+4+5+7+8+9	0.1279 ± 0.0049
2+3+4+5+6+8+9	0.1282 ± 0.0050
2+3+4+5+6+7+9	0.1286 ± 0.0050

Table 7.7. Values of the fitted $\alpha_s(M_Z^2)$ for the fit with different combinations of moments.

The number of fitted moments is sometimes different for different values of x_0 . When x_0 is large the x -range is very narrow and moments are strongly correlated. As a consequence the correlation matrix is almost singular since all its elements are close to one. Thus, the numerical precision on the inversion of the correlation matrix may fail. In Appendix B.4 we show that under these conditions also pathological effects on the minimization of the χ^2 may arise, *i.e.* values of α_s with extremely small errors and pathological best fits of moments. When $x_0 = 0.01$ the x -range is wider and even if correlations still play an important role, they are generally not so strong as to give rise to pathological effects. The best value of α_s is given by

$$\alpha_s(M_Z^2) = 0.128 \pm 0.005. \quad (7.2.2)$$

As an example, for the case of the fit with 7 moments, in Table 7.8 we give also asymmetric errors. In order to be sure that no local minima are present in the parameter space, we explore the region of the minimum for

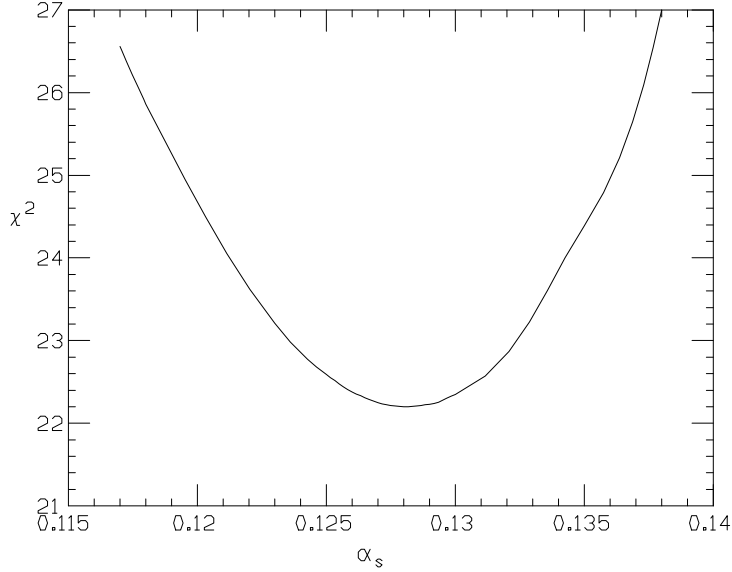


Figure 7.1. χ^2 vs. $\alpha_s(M_Z^2)$ with $x_0 = 0.01$, fit 2+3+4+5+6+8+9 and 15 d.o.f..

$x_0 = 0.01$	
Fitted moments	α_s
2+3+4+5+6+8+9	$0.1282^{+0.0047}_{-0.0051}$
2+3+4+5+7+8+9	$0.1279^{+0.0046}_{-0.0050}$
2+3+4+5+6+7+9	$0.1286^{+0.0048}_{-0.0052}$

Table 7.8. Values of the fitted $\alpha_s(M_Z^2)$ with asymmetric errors for the fit with 7 moments.

α_s . From Fig. 7.1 we can see that we have a well located parabolic minimum as confirmed by asymmetric errors.

We then address the choice of the number of scales and of the Q^2 range. We need at least two scales to fit one moment and α_s . Additional intermediate scales increase the number of points of the fit, and thus reduce the error. However, we can not increase arbitrarily the number of scales, especially when we fit several moments simultaneously. We have seen already that we have a limited amount of information from data, and, as a result, we must use a limited number of truncated moments as well as of intermediate scales.

As it is shown in Table 7.9 when we take the simultaneous fit of several moments, the error is smaller for 3 scales, than for 2 scales. Moreover, increasing the number of scales to 4 has a worse effect than increasing the number of fitted moments. Since a moment at different scales is more cor-

$x_0 = 0.01$		
Fitted moments	N. of Scales	α_s
2+3+5+6+7	2	0.1193 ± 0.0077
2+3+5+6+7	3	0.1284 ± 0.0050
2+3+5 +7	4	0.1051 ± 0.0071

Table 7.9. Values of the fitted $\alpha_s(M_Z^2)$ for the fit with a different number of scales and moments with $x_0 = 0.01$

$x_0 = 0.1$	
Q^2 range	α_s
20-70	0.1131 ± 0.0187
20-100	0.1091 ± 0.0176
30-100	0.1071 ± 0.0183
30-120	0.1064 ± 0.0181

Table 7.10. Values of the fitted $\alpha_s(M_Z^2)$ for the fit with different ranges of Q^2 and $x_0 = 0.01$

related than two neighboring moments at the same scale, a large number of scales does not add significant information and only causes pathological effects in the minimization of the χ^2 as discussed above. Thus, for the problem at hand the best choice is to use 3 scales.

The plot of the kinematic region Fig. 6.1 indicates how we have to choose x and Q^2 , if we want to avoid extrapolating outside the experimental kinematic region. Such a request is needed as we know (see Chapter 5) that neural networks are good in interpolation, but they are not very trustworthy in extrapolation. When $x_0 = 0.01$ the maximum allowed value of Q^2 is 70 GeV^2 . Thus, in order to understand the effects of varying the Q^2 range we will take $x_0 = 0.1$ that allows us more flexibility in the choice of the final scale (see Fig. 6.1). Table 7.10 shows that the effect of varying the Q^2 range is small and within the statistical errors.

7.3 The theoretical uncertainties

The theoretical uncertainties of a phenomenological analysis can not be ultimately defined. The progress of studies may increase or decrease such biases. Throughout this thesis we have shown how we can avoid some of them, specifically:

- with the technique of truncated moments we can avoid theoretical assumptions on the shape of parton distributions in the small- x region

(see Chapter 4). As we have shown the evolution uncertainty is negligible;

- with a neural network fit we can avoid theoretical assumptions on the shape of the structure function F_2 when we fit experimental data (see Chapter 6);
- with a careful choice of the kinematical region over which we perform our analysis we can avoid kinematical and dynamical higher twists, as well as elastic contributions.

We are then left with only two sources of uncertainties, *i.e.* the matching of α_s at quark mass thresholds and the effects NNLO unaccounted contributions.

It is worth noting that since combinations with several moments may be sensitive to the numerical precision (see previous Section) of calculations and since we are looking for small effects, we prefer to adopt in the following analysis the truncated moments combination 2+3+5+6+7 with $x_0 = 0.01$ that yields the same central value and the same error of combinations with more moments, but with a more stable numerical precision.

We have seen in Sect. 2.4.3 how we can define α_s in a scheme where it varies with the number of active quarks. We have shown also how we can match the different couplings to let α_s be continuous when it crosses quark mass thresholds. As result we may have a dependence on the matching conditions we have used to connect the couplings. As explained we will assess this ambiguity by requiring that α_s is continuous at $Q_i^2 = k_{th} m_i^2$, with m_i the heavy quark mass. Then, we will let k_{th} vary from 1/2 to 2. In the kinematic range we have chosen, we have only the b -quark threshold, and we have used $m_b = 5$ GeV. From Tab. 7.11 we observe that matching conditions effects are negligible. For completeness in Fig. 7.2 we show the effects of varying k_{th} over a wider range. Almost all points lay in the systematic error band of the value with $k_{th} = 1$ and their spread is very narrow.

The uncertainty due to the renormalization scale has been discussed in previous section. Tab. 7.12 shows the results of varying k_R from 1/4 to 4. Again in Fig. 7.2 we show the effects of varying k_R over a wider range, analogous to that used in [65]. We observe that the uncertainties are relevant. Note also that they are asymmetric and that we have a larger effect when the central value is closer to the world average. Thus, we can conclude that NNLO contributions play an important role in the evolution of truncated moments, and an analysis taking into account these contributions may be explored. Our final result is

$$\alpha_s(M_Z^2) = 0.128 \pm 0.005 (stat.)_{-0.006}^{+0.004} (theor.). \quad (7.3.1)$$

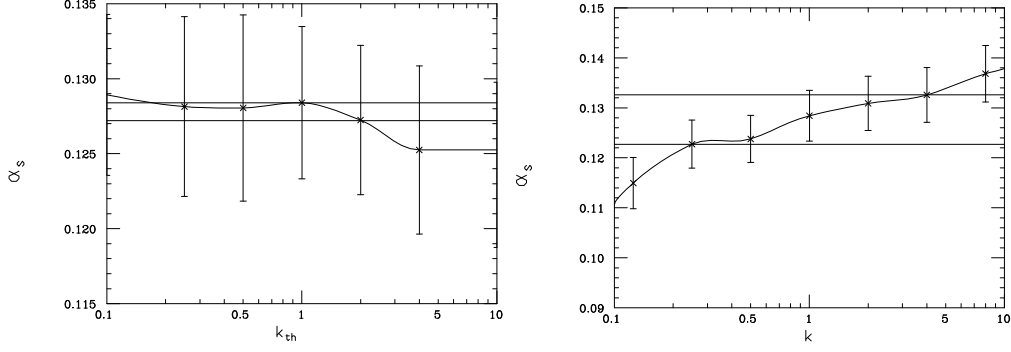


Figure 7.2. Variation of $\alpha_s(M_Z^2)$ as a function of k_{th} and k_R with $x_0 = 0.01$, fit $2+3+5+6+7$ with theoretical systematic error bands obtained from Tables 7.11 and 7.12 and statistical error bars on each point.

$x_0 = 0.01$	
k	α_s
2	0.1272 ± 0.0050
1	0.1284 ± 0.0051
1/2	0.1281 ± 0.0062

Table 7.11. Values of the fitted $\alpha_s(M_Z^2)$ for the fit with different quark mass thresholds and moments $2+3+5+6+7$.

$x_0 = 0.01$	
k	α_s
4	0.1326 ± 0.0055
1	0.1284 ± 0.0051
1/4	0.1227 ± 0.0048

Table 7.12. Values of the fitted $\alpha_s(M_Z^2)$ for the fit with different renormalization scales and moments $2+3+5+6+7$.

8

Conclusions

We have performed a phenomenological analysis of DIS data in the context of perturbative QCD with the purpose of reducing theoretical uncertainties, and taking into proper account all experimental errors and correlations. Specifically:

- we have extended the method of truncated moments suggested in [28] for the case of non-singlet parton distributions to the singlet case [29]. Truncated moments of parton distributions are defined by restricting the integration range over the Bjorken variable to an experimentally accessible subset $x_0 < x < 1$ of the allowed kinematic range $0 < x < 1$. This method provides a way to avoid theoretical biases on the shape of parton distributions. We have shown how to increase the numerical efficiency of the method, and how to use it as a way to solve the Altarelli-Parisi evolution equations [30];
- we have performed a fit of the non-singlet structure function data. Preliminary work on individual (proton and deuteron) structure function fits has also been performed. The neural network approach we have suggested allows to avoid sources of theoretical bias, such as the choice of a given shape of the fitted function, which are difficult to keep under control. We have adopted a Monte Carlo technique to estimate errors and correlations for any quantity which can be extracted from our fit, such as *e.g.* the error on F_2 for given values of x and Q^2 , or the correlation between two Mellin moments. Our results will be published in [41];
- using the techniques outlined above, we have performed a determination of the strong coupling constant α_s [51]. We have taken into account all correlated systematic experimental errors. As a result of the adopted methods the theoretical bias is lower than in the case of

previous analyses. Our result for α_s is compatible within errors with the world average; the analysis may be refined in order to reduce the statistical errors. We have also pointed out the need of a more precise knowledge of NNLO contributions when all other theoretical biases are correctly taken into account.

Outlook

The work presented in this thesis can be extended in different directions.

The neural network fit of F_2 should be extended to include HERA, and E665 data. This would cover the whole experimental range presently explored. In particular, this would allow a detailed analysis of the small- x region. An analogous fit of the structure functions with deep inelastic neutrino scattering data may be performed as well.

The approach we have suggested to fit the unpolarized structure functions may also be adopted to fit the polarized structure function g_1 . A neural network fit of g_1 would allow an analysis of the spin structure of the nucleon, as well as an independent extraction of α_s .

Finally, a determination of α_s may be performed with truncated moments of singlet parton distributions. In this case, the theoretical uncertainties are generally larger than in the non-singlet case, but on the other hand the amount of available data is also larger.

Acknowledgments

I am greatly indebted to Giovanni Ridolfi and Stefano Forte for reducing the theoretical biases on my knowledge.

I thank Lorenzo Magnea for opening my mind to truncated moments.

I thank José I. Latorre and L. Garrido for training my neural networks on neural networks.

I thank Carlo Becchi for wise advice at the right time.

I thank Beppe Carlino, Franz Montalenti and Stefano Giusto for teaching me how a good PhD. fellow should behave.

I thank the Departament d'Estructura i Constituents de la Matèria de la Universitat de Barcelona for kind hospitality during part of this work.

I thank the INFN Sezione di Roma III and PhD. students of the Università di Roma III for kind hospitality during the last part of this work.

A

Diagonalization of triangular matrices

In this Appendix, we show how to construct the matrix R which diagonalizes a generic $n \times n$ triangular matrix T by means of the recursion relations eqs. (4.1.16,4.1.17). The matrix R is defined by the requirement that

$$RTR^{-1} = \text{diag}(\gamma_1, \dots, \gamma_n) , \quad (\text{A.1.1})$$

where the matrix T is upper triangular, *i.e.* $T_{ij} = 0$ if $i > j$. It is easy to see, by solving the secular equation, that the eigenvalues γ_i of T coincide with its diagonal elements,

$$\gamma_i = T_{ii} . \quad (\text{A.1.2})$$

Now, define eigenvectors v^j associated to the j^{th} eigenvalue T_{jj} , with components v_i^j :

$$\sum_{k=1}^n T_{ik} v_k^j = \gamma_j v_i^j . \quad (\text{A.1.3})$$

Clearly, the matrix R^{-1} coincides with the matrix of right eigenvectors, $(R^{-1})_{ij} = v_i^j$, while the matrix R coincides with the matrix of left eigenvectors $\sum_{k=1}^n \hat{v}_k^j T_{ki} = \gamma_j \hat{v}_i^j$, $R_{ij} = \hat{v}_i^j$. The eigenvector condition eq. (A.1.3) immediately implies that the j^{th} component of the j^{th} eigenvector is equal to one: $v_j^j = 1$. Furthermore, it is clear that eq. (A.1.3) can only be satisfied if all components v_k^j of the j^{th} eigenvector with $k > j$ vanish,

$$v_j^j = 1 ; \quad v_k^j = 0 \quad \text{if } k > j . \quad (\text{A.1.4})$$

Using eq. (A.1.4) and the fact that the matrix T is triangular, eq. (A.1.3) can be written as

$$\sum_{k=i}^j T_{ik} v_k^j = \gamma_j v_i^j . \quad (\text{A.1.5})$$

Substituting the explicit form of the eigenvalues, eq. (A.1.2), and identifying $v_i^j = (R^{-1})_{ij}$, this is immediately seen to coincide with eq. (4.1.17). Furthermore, using the condition $v_j^j = 1$, this equation can be viewed as a recursion relation which allows the determination of the $(k - 1)^{th}$ element of v^j once the k^{th} element is known, which is what we set out to prove. The same argument, applied to the left eigenvectors, leads to the expression in eq. (4.1.16) for R .

B

Tools of statistics

The aim of this appendix is to report basic and useful definitions of statistic and introduce the notations adopted in the thesis. Here we will follow [66, 67].

B.1 Distribution of several random variables

We only consider the case of two continuous variables (X and Y). The extension to more variables is straightforward. The infinitesimal element of probability is $dF(x, y) = f(x, y) dx dy$, and the probability density function

$$f(x, y) = \frac{\partial^2 F(x, y)}{\partial x \partial y}. \quad (\text{B.1.1})$$

The probability of finding the variable inside a certain area A is

$$\int_A f(x, y) dx dy. \quad (\text{B.1.2})$$

Expected Value

$$\mu_X = E[X] = \int_{-\infty}^{\infty} x f(x, y) dx dy, \quad (\text{B.1.3})$$

and analogously for Y. Generally,

$$E[g(X, Y)] = \int_{-\infty}^{\infty} g(x, y) f(x, y) dx dy. \quad (\text{B.1.4})$$

Variance

$$V[X] = \sigma_X^2 = \int_{-\infty}^{\infty} (x - \mu)^2 f(x, y) dx dy = E[X^2] - E[X]^2, \quad (\text{B.1.5})$$

and analogously for Y.

Covariance

$$\begin{aligned} V_{XY} &= \text{cov}[X, Y] = E[(X - E[X])(Y - E[Y])] = E[XY] - \mu_X \mu_Y \\ &= \int_{-\infty}^{\infty} xyf(x, y) dx dy - \mu_X \mu_Y, \end{aligned} \quad (\text{B.1.6})$$

where $\mu_X = E[X]$ and $\mu_Y = E[Y]$. The covariance matrix is also called the error matrix, as $V_{XX} = V[X] = \sigma_X^2$. If X and Y are independent, then $E[XY] = E[X]E[Y]$ and hence $V_{XY} = 0$ (the opposite is true only if X and Y have the same normalization).

Correlation coefficient

$$\rho_{XY} = \frac{\text{cov}[X, Y]}{\sqrt{V[X]V[Y]}} = \frac{V_{XY}}{\sigma_X \sigma_Y}, \quad (\text{B.1.7})$$

The correlation coefficient gives a dimensionless measure of the level of correlation between two random variables X and Y. One can show that the correlation coefficient lies in the range $-1 \leq \rho_{XY} \leq 1$.

Linear combination of random variables

If $Y = \sum_i c_i X_i$ with c_i real, then

$$\mu_Y = E[Y] = \sum_i c_i E[X_i] = \sum_i c_i \mu_i \quad (\text{B.1.8})$$

$$\begin{aligned} V[Y] &= \sigma_Y^2 = \sum_i c_i V[X_i] + 2 \sum_{i < j} c_i c_j \text{cov}[X_i, X_j] \\ &= \sum_i c_i c_j \sigma_{ij}, \end{aligned} \quad (\text{B.1.9})$$

where $\sigma_{ij} = \text{cov}[X_i, X_j] = V_{ij}$, $\sigma_{ii} = V[X_i]$ and $\rho_{ii} = 1$.

B.2 Gaussian distribution

The N-dimensional Gaussian distribution is defined by

$$f(\mathbf{X}; \boldsymbol{\mu}, V) = \frac{1}{(2\pi)^{N/2} |V|^{1/2}} \exp \left[\frac{1}{2} (\mathbf{X} - \boldsymbol{\mu})^T V^{-1} (\mathbf{X} - \boldsymbol{\mu}) \right], \quad (\text{B.2.1})$$

where \mathbf{X} and $\boldsymbol{\mu}$ are column vectors containing X_1, \dots, X_N and μ_1, \dots, μ_N , \mathbf{X}^T and $\boldsymbol{\mu}^T$ are the corresponding row vectors, and $|V|$ is the determinant of a symmetric $N \times N$ matrix V, thus containing $N(N + 1)/2$ parameters.

The importance of the Gaussian distribution stems from the central limit theorem. The theorem states that the sum of N independent continuous random variables X_i with means μ_i and variance σ_i^2 becomes a Gaussian random variable with mean $\mu = \sum_{i=1}^N \mu_i$ and variance $\sigma^2 = \sum_{i=1}^N \sigma_i^2$ in the limit that N approaches infinity. This holds regardless of the form of the individual probability density functions of the X_i . This is the formal justification for treating measurements errors as Gaussian random variables, and holds to the extent that the total error is the sum of a large number of small contributions. The expectation values, variances and covariances can be computed to be

$$\begin{aligned} E[X_i] &= \mu_i \\ V[X_i] &= V_{ii} \\ \text{cov}[X_i, X_j] &= V_{ij}. \end{aligned} \tag{B.2.2}$$

B.3 Estimators for mean, variance, covariance

Consider the case where one has made N measurements of a random variable X whose probability density function $f(x)$ is not known. Our task is to infer properties of $f(x)$ based on observations x_1, \dots, x_N . Specifically, we would like to construct functions of the x_i to estimate the various properties of the probability density function $f(x)$. Usually we have a hypothesis for the probability density function $f(x)$ which depends on an unknown parameter (or parameters $\theta = (\theta_1, \dots, \theta_m)$). The goal is then to construct a function of the observed x_i to estimate parameters.

A function of the observed measurements x_1, \dots, x_N which contains no unknown parameters is called *statistic*. In particular, a statistic used to estimate some property of a probability density function (*e.g.* its mean, variance or other parameters) is called an *estimator*. The estimator of a quantity θ is usually written with a hat, $\hat{\theta}$, to distinguish it from the true value θ whose exact value is unknown.

If $\hat{\theta}$ converges to θ in the limit of large N , the estimator is said to be *consistent*. Here convergence is meant in the sense of probability: for any $\epsilon > 0$, one has

$$\lim_{N \rightarrow \infty} P(|\hat{\theta} - \theta| > \epsilon) = 0. \tag{B.3.1}$$

Consistency is usually a minimum requirement for a useful estimator. Other features of estimators are *bias* (see later) and *robustness*, *i.e.* the property of being insensitive to departures from assumptions in the probability density function owing to factors such as noise. The procedure of estimating the value of a parameter, given the data x_1, \dots, x_N , is called *parameter fitting*.

The expectation value of an estimator $\hat{\theta}$ with the sampling probability density function $g(\hat{\theta}, \theta)$ is

$$E[\hat{\theta}] = \int \hat{\theta} g(\hat{\theta}, \theta) d\hat{\theta}. \quad (\text{B.3.2})$$

Recall that this is the expected mean value of $\hat{\theta}$ from an infinite number of similar experiments, each with a sample of size N . We define the *bias* of an estimator $\hat{\theta}$ as

$$b = E[\hat{\theta}] - \theta. \quad (\text{B.3.3})$$

Note that the bias does not depend on the measured values of the sample but rather on the sample size, the functional form of the estimator and on the true properties of the probability density function $f(x)$, including the true value of θ . A parameter for which the bias is zero independent of the sample size N is said to be unbiased; if the bias vanishes in the limit $N \rightarrow \infty$ then it is said to be asymptotically unbiased.

We now consider the case where one has a sample of size N of a random variable $X, (x_1, \dots, x_N)$. It is assumed that X is distributed according to some probability density function $f(x)$ which is not known, not even as a parametrization. We would like to construct a function of the x_i to be an estimator for the expectation value of X, μ . One possibility is the arithmetic mean of the x_i , defined by

$$\langle x \rangle_N = \frac{1}{N} \sum_{i=1}^N x_i. \quad (\text{B.3.4})$$

The arithmetic mean of the elements of a sample is called the *sample mean*, and is denoted by $\langle x \rangle$ (where we generally omit the index N) or by a bar, *e.g.* \bar{x} . This should not be confused with the expectation value (population mean or central value of $f(x)$) of x , denoted by μ or $E[x]$, for which $\langle x \rangle$ is an estimator. The first important property of the sample mean is given by the weak law of large numbers. This states that if the variance of x exists, then $\langle x \rangle$ is a consistent estimator for the population mean μ . That is, for $N \rightarrow \infty$, $\langle x \rangle$ converges to μ in the sense of probability.

The expectation values of the sample mean $E[\langle x \rangle]$ is given by

$$E[\langle x \rangle] = E \left[\frac{1}{N} \sum_{i=1}^N x_i \right] = \frac{1}{N} \sum_{i=1}^N E[x_i] = \mu, \quad (\text{B.3.5})$$

for all i . Thus one can see that the sample mean $\langle x \rangle$ is an unbiased estimator for the population mean μ .

If the mean μ is known, then the quantity $\hat{\sigma}^2$ defined by

$$\hat{\sigma}^2 = \frac{1}{N-1} \sum_{i=1}^N (x_i - \mu)^2 = \langle x^2 \rangle - \mu^2, \quad (\text{B.3.6})$$

is an unbiased estimator of the variance σ^2 . In a similar way one can show that the quantity

$$\hat{V}_{XY} = \frac{1}{N-1} \sum_{i=1}^N (x_i - \langle x \rangle)(y_i - \langle y \rangle) \quad (\text{B.3.7})$$

is an unbiased estimator for the covariance V_{XY} of two random variables X and Y of unknown mean. This can be normalized by the square root of the estimators for the sample variance to form an estimator r for the correlation coefficient ρ :

$$r = \frac{\langle xy \rangle - \langle x \rangle \langle y \rangle}{\sqrt{\langle x^2 \rangle - \langle x \rangle^2} \sqrt{\langle y^2 \rangle - \langle y \rangle^2}}. \quad (\text{B.3.8})$$

Given an estimator $\hat{\theta}$ one can compute its variance $V[\hat{\theta}] = E[\hat{\theta}^2] - (E[\hat{\theta}])^2$. Recall that $V[\hat{\theta}]$ (or equivalently its square root $\sigma_{\hat{\theta}}$) is a measure of the variation of $\hat{\theta}$ about its mean in a large number of similar experiments each with sample size N , and as such is often quoted as the statistical error of $\hat{\theta}$. For example, the variance of the sample mean $\langle x \rangle$ is

$$V[\langle x \rangle] = \frac{\sigma^2}{N}, \quad (\text{B.3.9})$$

where σ^2 is the variance of $f(x)$. In a similar way, the variance of the estimator $\hat{\sigma}^2$ for a Gaussian distribution, can be computed to be

$$V[\hat{\sigma}^2] = \frac{2}{N-1} \sigma^4. \quad (\text{B.3.10})$$

The expectation value and variance of the estimator of the correlation coefficient for a two dimensional Gaussian are found to be

$$E[r] = \rho - \frac{\rho(1-\rho^2)}{2N} + O(N^2), \quad (\text{B.3.11})$$

$$V[r] = \frac{(1-\rho^2)^2}{N} + O(N^2). \quad (\text{B.3.12})$$

The estimator r given by eq. (B.3.8) is only asymptotically unbiased. Thus, we should be very careful when applying eq. (B.3.12) to evaluate the significance of an observed correlation.

B.4 Least squares minimization

Consider now a set of N independent Gaussian random variables m_i , $i = 1, \dots, N$, each related to another variable x_i , which is assumed to be known without error. Assume that each value m_i has a different unknown mean, t_i , and a different but known variance, σ_i . The N measurements of m_i can be equivalently regarded as a single measurement of an N -dimensional random vector, for which the joint probability distribution function is the product of N Gaussians,

$$f(m_1, \dots, m_N; t_1, \dots, t_N, \sigma_1^2, \dots, \sigma_N^2) = \prod_{i=1}^N \frac{1}{\sqrt{2\pi\sigma_i^2}} \exp\left(-\frac{(m_i - t_i)^2}{2\sigma_i^2}\right). \quad (\text{B.4.1})$$

We suppose also that the true value is given as a function of x , $t = t(x; \boldsymbol{\theta})$, which depends on unknown parameters $\boldsymbol{\theta} = (\theta_1, \dots, \theta_N)$. The aim of the method of the least squares is to estimate the parameters $\boldsymbol{\theta}$. In addition, the method allows for a simple evaluation of the goodness-of-fit of the hypnotized function $t(x; \boldsymbol{\theta})$.

Taking the logarithm of the joint probability function and dropping additive terms that do not depend on the parameters gives the log-likelihood function,

$$\log L(\boldsymbol{\theta}) = -\frac{1}{2} \sum_{i=1}^N \frac{(m_i - t_i)^2}{\sigma_i^2}. \quad (\text{B.4.2})$$

This is maximized by finding the values of the parameters $\boldsymbol{\theta}$ that minimize the quantity

$$\chi^2(\boldsymbol{\theta}) = \sum_{i=1}^N \frac{(m_i - t_i)^2}{\sigma_i^2}, \quad (\text{B.4.3})$$

namely the quadratic sum of differences between measured and hypnotized values, weighted by the inverse of variances. This is the basis of the *method of least squares* (LS), and it is used to define the procedure even in cases where individual measurements are not Gaussian, but as long as they are independent.

If the measurements are not independent but can be described by an N -dimensional Gaussian probability distribution function with known covariance matrix V but unknown mean values, the corresponding log-likelihood function is obtained from the logarithm of the joint probability function given

by eq. (B.2.1)

$$\log L(\boldsymbol{\theta}) = -\frac{1}{2} \sum_{i,j=1}^N (m_i - t_i(x_i; \boldsymbol{\theta})) V_{ij}^{-1} (m_j - t_j(x_j; \boldsymbol{\theta})), \quad (\text{B.4.4})$$

where additive terms not depending on the parameters have been dropped. This is maximized by minimizing the quantity

$$\chi^2(\boldsymbol{\theta}) = \sum_{i,j=1}^N (m_i - t_i(x_i; \boldsymbol{\theta})) V_{ij}^{-1} (m_j - t_j(x_j; \boldsymbol{\theta})) \quad (\text{B.4.5})$$

which reduces to eq. (B.4.3) if the covariance matrix (and hence its inverse) are diagonal. The parameter that minimize the χ^2 are called the LS estimators, $\hat{\theta}_1, \dots, \hat{\theta}_m$. The explicit expression of \mathbf{V} can be found by taking

$$m_i = t_i(\boldsymbol{\theta}) + r_i \sigma_i + \sum_k s_k \Delta_{ik} \quad (\text{B.4.6})$$

where m_i is the measurement of data point i , $t_i(\boldsymbol{\theta})$ is the model prediction depending on a set of parameters $\boldsymbol{\theta}$, σ_i is the uncorrelated (statistical) error on data point i and Δ_{ik} is the correlated (systematic) error from source k . In eq. (B.4.6), r_i and s_k denote Gaussian random variables with zero mean and unit variance. These random variables are assumed to be independent of each other:

$$\langle \Delta r_i \Delta r_j \rangle = \langle \Delta s_i \Delta s_j \rangle = \delta_{ij} \quad \langle \Delta r_i \Delta s_j \rangle = 0. \quad (\text{B.4.7})$$

From eqs. (B.4.6) and (B.4.7) the covariance matrix \mathbf{V} of the measurements is given by

$$V_{ij} = \langle \Delta m_i \Delta m_j \rangle = \delta_{ij} \sigma_i^2 + \sum_k \Delta_{ik} \Delta_{jk}. \quad (\text{B.4.8})$$

Minimizing χ^2 defined by eq. (B.4.5) is impractical because it involves the inversion of the measurement covariance matrix (B.4.8) which, in global fits, tends to become very large. Because the systematic errors of different data sets are in general uncorrelated (but not always, see [42]) this matrix takes a block diagonal form and each block could, in principle, be inverted once and for all. However, the dimension of these block matrices can still easily be larger than a few hundred. Furthermore, if the systematic errors dominate, the covariance matrix might, numerically, be uncomfortably close to a matrix with the simple structure $V_{ij} = \Delta_i \Delta_j$, which is singular.

Fortunately, the χ^2 of (B.4.5) can be cast in an alternative form which avoids the inversion of large matrices [68]:

$$\begin{aligned}\chi^2 &= \sum_i \left(\frac{m_i - t_i}{\sigma_i} \right)^2 - \mathbf{B} \mathbf{A}^{-1} \mathbf{B} \\ B_k &= \sum_i \Delta_{ik} (m_i - t_i) / \sigma_i^2 \\ A_{kl} &= \delta_{kl} + \sum_i \Delta_{ik} \Delta_{il} / \sigma_i^2.\end{aligned}\tag{B.4.9}$$

The matrix \mathbf{A} in eq. (B.4.9) has the dimension of the number of systematic sources only and can be inverted at the initialization phase of a fitting program once the number of data points included in the fit (*i.e.* after cuts) is known. An example of a global QCD fit with error calculations based on the covariance matrix approach can be found in [56].

It is remarkable that minimizing eq. (B.4.9) is equivalent to a fit where *both* the parameters θ and \mathbf{s} are left free. In such a fit χ^2 is defined as follows. First, the effect of the systematic errors is incorporated in the model prediction

$$f_i(\boldsymbol{\theta}, \mathbf{s}) = t_i(\boldsymbol{\theta}) + \sum_k s_k \Delta_{ik}.\tag{B.4.10}$$

Next, χ^2 is defined by

$$\chi^2 = \sum_i \left(\frac{m_i - f_i(\boldsymbol{\theta}, \mathbf{s})}{\sigma_i} \right)^2 + \sum_k s_k^2.\tag{B.4.11}$$

The second term in eq. (B.4.11) serves to constrain the fitted values of \mathbf{s} . The presence of this term is easily understood if one takes the view that the calibration of each experiment yields a set of ‘measurements’ $s_k = 0 \pm 1$ [69].

Because f is linear in \mathbf{s} the minimization with respect to the systematic parameters can be done analytically. It is easy to show, by solving the equations $\partial\chi^2/\partial s_k = 0$, that this leads to the χ^2 given by eq. (B.4.9) which, in turn, is equivalent to eq. (B.4.5), see [68]. The relation between the optimal values of \mathbf{s} , the matrix \mathbf{A} and the vector \mathbf{B} of eq. (B.4.9) is

$$\mathbf{s} = \mathbf{A}^{-1} \mathbf{B}.\tag{B.4.12}$$

Remarks

- If we have data with correlated systematic uncertainties, the minimization of eq. (B.4.3) called also the *simplest χ^2 estimator* (SCE), is an

estimator of the χ^2 given by eq. (B.4.5), *covariance matrix estimator* (CME). It can be shown [70] that the value of the error due to improved statistical precision for the SCE does not necessarily decrease after adding a new point. Qualitatively, for SCE the fitted curve tightly follows the data points and, if these points are shifted due to the systematic errors fluctuations, the parameter gains appropriate systematic errors. At the same time, since for the CME the information on data correlations is explicitly included in χ^2 , the correlated fluctuation of data due to systematic shift does not necessary leads to the fitted curve shift and parameter deviation gets smaller than for SCE.

- If we have strong correlations, the correlation matrix is almost singular and we may find pathological results. Eq. (B.4.5) can be written as

$$\chi^2 = \sum_{i,j=1}^N \frac{m_i - t_i}{\sigma_i} \rho_{ij}^{-1} \frac{m_j - t_j}{\sigma_j}. \quad (\text{B.4.13})$$

If we take as an example the case with only two data, we have

$$\begin{aligned} \rho &= \begin{pmatrix} 1 & 1 - \delta \\ 1 - \delta & 1 \end{pmatrix} \\ \rho^{-1} &= \frac{1}{2\delta - \delta^2} \begin{pmatrix} 1 & -1 + \delta \\ -1 + \delta & 1 \end{pmatrix}. \end{aligned} \quad (\text{B.4.14})$$

Thus, we get

$$\begin{aligned} \chi^2 &\approx \frac{1}{2\delta - \delta^2} \left[\left(\frac{m_1 - t_1}{\sigma_1} \right)^2 + \left(\frac{m_2 - t_2}{\sigma_2} \right)^2 \right. \\ &\quad \left. - 2 \frac{(m_1 - t_1)(m_2 - t_2)}{\sigma_1 \sigma_2} \right], \end{aligned} \quad (\text{B.4.15})$$

that can be zero not only if $m_i = t_i$. Notice also that the covariance matrix has N diagonal terms and $N(N - 1)$ off-diagonal ones. If off-diagonal terms are large, their effect may be stronger than that of the diagonal terms. An example of such a pathological result is shown in Fig. B.1.

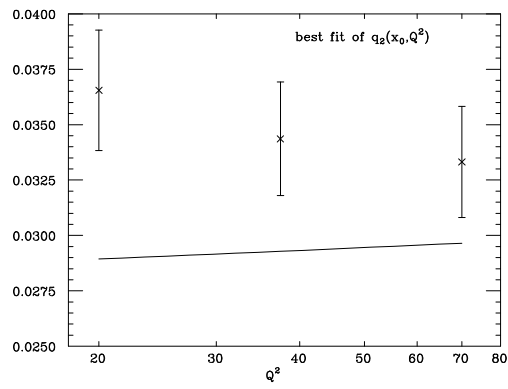


Figure B.1: *Pathological fit of the second truncated moment with $x_0 = 0.2$*

C

Numerical routines

Here we reproduce the codes given in [49] that we have used to generate random numbers. The random numbers generator `ran1` is very trustful as it is not known any statistical test that it fails to pass, except when the number of calls starts to become on the order of the period m , say $> 10^8$. For our applications the maximum number of calls is less than 10^5 .

```
FUNCTION ran1(idum)
  INTEGER idum,IA,IM,IQ,IR,NTAB,NDIV
  REAL ran1,AM,EPS,RNMX
  PARAMETER (IA=16807,IM=2147483647,
*AM=1./IM,IQ=127773,IR=2836,
*NTAB=32,NDIV=1+(IM-1)/NTAB,EPS=1.2e-7,RNMX=1.-EPS)
  INTEGER j,k,iv(NTAB),iy
  SAVE iv,iy
  DATA iv /NTAB*0/, iy /0/
  if (idum.le.0.or.iy.eq.0) then
    idum=max(-idum,1)
    do 11 j=NTAB+8,1,-1
      k=idum/IQ
      idum=IA*(idum-k*IQ)-IR*k
      if (idum.lt.0) idum=idum+IM
      if (j.le.NTAB) iv(j)=idum
11    continue
    iy=iv(1)
  endif
  k=idum/IQ
  idum=IA*(idum-k*IQ)-IR*k
  if (idum.lt.0) idum=idum+IM
  j=1+iy/NDIV
  iy=iv(j)
```

```

iv(j)=idum
ran1=min(AM*iy,RNMX)
return
END

```

The routine `gasdev` simply returns normally distributed Gaussian random numbers with zero mean and unit variance, using `ran1(idum)` as the source of random numbers.

```

FUNCTION gasdev(idum)
INTEGER idum
REAL gasdev
INTEGER iset
REAL fac,gset,rsq,w1,w2,ran1
SAVE iset,gset
DATA iset/0/
if (iset.eq.0) then
1   w1=2.*ran1(idum)-1.
   w2=2.*ran1(idum)-1.
   rsq=w1**2+w2**2
   if(rsq.ge.1..or.rsq.eq.0.)goto 1
   fac=sqrt(-2.*log(rsq)/rsq)
   gset=w1*fac
   gasdev=w2*fac
   iset=1
else
   gasdev=gset
   iset=0
endif
return
END

```

The `idirty` generator is a quick random number generator used to *somewhat* randomize things. What we need in the training of neural networks is to process data from experiments not always in the same order to avoid a bias on the training (see Chapter 5). Here the period is 6075.

```

jran=mod(jran*106+1283,6075)
idirty=jlo+((jhi-jlo+1)*jran)/6075

```

References

Basics of QCD

- [1] G. Altarelli, *Phys. Rep.* **81** (1982) 1.
- [2] R.K. Ellis, W.J. Stirling and B.R. Webber, *QCD and Collider Physics*, C.U.P., Cambridge (1996).
- [3] F. Halzen and A. D. Martin, *Quarks and leptons. An introductory course in modern particles theory*, Wiley and Sons, New York (1984).
- [4] M. E. Peskin and D. V. Schroeder, *An introduction to Quantum Field Theory*, Addison-Wesley, Reading (1995)
- [5] P. Ramond, *Field Theory: a modern primer*, Addison-Wesley, (1990).
- [6] G. 't Hooft, *Nucl. Phys.* **B138** (1978) 1;
G. 't Hooft, *Physica Scripta* **24** (1981) 841.
- [7] T. Appelquist and J. Carazzone, *Phys. Rev.* **D11** (1975) 2856.
- [8] G. Rodrigo and A. Santamaria, *Phys. Lett.* **B313** (1993) 441,
[arXiv:hep-ph/9305305].
- [9] R.G. Roberts, *The structure of the proton* C.U.P., Cambridge (1990)
- [10] W.J. Marciano, *Phys. Rev.* **D29** (1984) 5801.

QCD and the parton model

- [11] J. M. Conrad, M. H. Shaevitz and T. Bolton, *Rev. Mod. Phys.* **70** (1998) 1341, [arXiv:hep-ex/9707015].
- [12] J. D. Bjorken *Phys. Rev.* **179** (1969) 1547.
- [13] R. P. Feynman, *Photon-Hadron Interactions*, Benjamin, New York (1972).

-
- [14] C. G. Callan and D. J. Gross, *Phys. Rev. Lett.* **22** (1969) 156.
- [15] W. A. Bardeen, A. J. Buras, D. W. Duke and T. Muta, *Phys. Rev.* **D18** (1978) 3998.
- [16] W. L. van Neerven and E. B. Zijlstra, *Phys. Lett.* **B272** (1991) 127, *Phys. Lett.* **B273** (1991) 476;
W. L. van Neerven and E. B. Zijlstra, *Nucl. Phys.* **B382** (1992) 11, *Nucl. Phys.* **B383** (1992) 525.
- [17] G. Altarelli and G. Parisi, *Nucl. Phys.* **B126** (1977) 298
- [18] W. Furmanski and R. Petronzio, *Phys. Lett.* **B97** (1980) 437;
G. Curci, W. Furmanski and R. Petronzio, *Nucl. Phys.* **B175** (1980) 27.
- [19] G. Altarelli, R.K. Ellis and G. Martinelli, *Nucl. Phys.* **B143** (1979) 521
- [20] M. Diemoz, S. Ferroni, M. Longo and G. Martinelli, *Zeit. Phys.* **C39** (1988) 20.
- [21] S. Catani and F. Hautmann, *Nucl. Phys.* **B427** (1994) 475
[arXiv:hep-ph/9405388];
S. Catani, *Zeit. Phys.* **C75** (1997) 665, [arXiv:hep-ph/9609263].

Truncated Moments of parton distributions

- [22] H. L. Lai, J. Huston *et al.*, *Eur. Phys. J.* **C12** (2000) 375,
[arXiv:hep-ph/9903282];
A. D. Martin, R. G. Roberts, W. J. Stirling and R. Thorne, *Eur. Phys. J.* **C4** (1998) 463, [arXiv:hep-ph/9906231];
G. Altarelli *et al.*, *Nucl. Phys.* **B496**, 337 (1997),
[arXiv:hep-ph/9701289].
- [23] See *e.g.* S. Forte, *Nucl. Phys.* **A666** (2000) 113.
- [24] W. T. Giele and S. Keller, *Phys. Rev.* **D58** (1998) 094023,
[arXiv:hep-ph/9803393];
D. Kosower, W. T. Giele and S. Keller, Proc. of the 1999 “Rencontres de Physique de la Vallée d’Aoste”, pag. 255 (INFN, Frascati, 1999);
R. D. Ball and J. Huston, in S. Catani *et al.*, [arXiv:hep-ph/0005114].
- [25] F. J. Yndurain, *Phys. Lett.* **B74** (1978) 68.
- [26] G. Parisi and N. Surlas, *Nucl. Phys.* **B151** (1979) 421.
- [27] W. Furmanski and R. Petronzio, *Nucl. Phys.* **B195** (1982) 237.

-
- [28] S. Forte and L. Magnea, *Phys. Lett.* **B448** (1999) 295, [arXiv:hep-ph/9812479]; in Proceedings of the International Europhysics Conference on High-Energy Physics (EPS-HEP 99), Tampere 1999, [arXiv:hep-ph/9910421].
- [29] S. Forte, L. Magnea, A. Piccione and G. Ridolfi, *Nucl. Phys.* **B594** (2001) 46, [arXiv:hep-ph/0006273];
- [30] A. Piccione, *Phys. Lett.* **B518** (2001) 207, [arXiv:hep-ph/0107108];
- [31] See *e.g.* Encyclopedic Dictionary of Mathematics, ed. by S. Iyanaga and Y. Kawada, M.I.T. Press, Cambridge MA (1980).

Introduction to Neural Networks

- [32] C. Peterson and T. Rönvaldsson, LU-TP-91-23 *Lectures given at 1991 CERN School of Computing, Ystad, Sweden, Aug 23 - Sep 2, 1991.*
- [33] W. S. McCulloch and W. Pitts, *Bull. Math. Biophys.* **5** (1943) 115
- [34] F. Rosenblatt, *Principles of neurodynamics*, Spartan, New York (1962).
- [35] J. S. Denker *et al.*, *Complex Systems* **1** (1987) 877.
- [36] G. Cybenko, *Math. Control Signal Systems* **2** (1989) 303.
- [37] D. E. Rumelhart, G.E. Hinton and R. J. Williams, *Learning internal representations by error propagation*, in *Parallel Distributed processing*, D. E. Rumelhart and J. L. Clelland (eds.), MIT Press, Cambridge MA (1986)
- [38] A. Weigend, B. A. Huberman and D. Rumelhart, *Int. Jour. of Neural Systems* **3** (1990) 193.
- [39] E. Baum and D. Haussler, *Neural Computation* **1** (1989) 151.

Neural Network fit of F_2

- [40] See *e.g.* S. Catani *et al.*, in the proceedings of the workshop *Standard Model Physics (and more) at the LHC* (CERN, 1999), [arXiv:hep-ph/0005025].
- [41] S. Forte, L. Garrido, J. I. Latorre and A. Piccione, [arXiv:hep-ph/0204232].
- [42] M. Arneodo *et al.* [New Muon Collaboration], *Nucl. Phys.* **B483** (1997) 3, [arXiv:hep-ph/9610231].

-
- [43] A. C. Benvenuti *et al.* [BCDMS Collaboration], *Phys. Lett.* **B223** (1989) 485;
A. C. Benvenuti *et al.* [BCDMS Collaboration], *Phys. Lett.* **B237** (1990) 592.
- [44] M. R. Adams *et al.* [E665 Collaboration] *Phys. Rev.* **D54** (1996) 3006.
- [45] A. C. Benvenuti *et al.* [BCDMS Collaboration], CERN-EP/89-06;
A. C. Benvenuti *et al.* [BCDMS Collaboration], CERN-EP/89-170.
- [46] A. Milsztajn, private communication.
- [47] T. Çuhadar, PhD. Thesis, Amsterdam Free Univeristy, 1998.
- [48] A. C. Benvenuti *et al.* [BCDMS Collaboration], *Phys. Lett.* **B223** (1989) 490.
- [49] William H. Press (Editor) *et al.*, *Numerical Recipes in Fortran*, Cambridge University Press, Cambridge (1992).

Determination of α_s with truncated moments

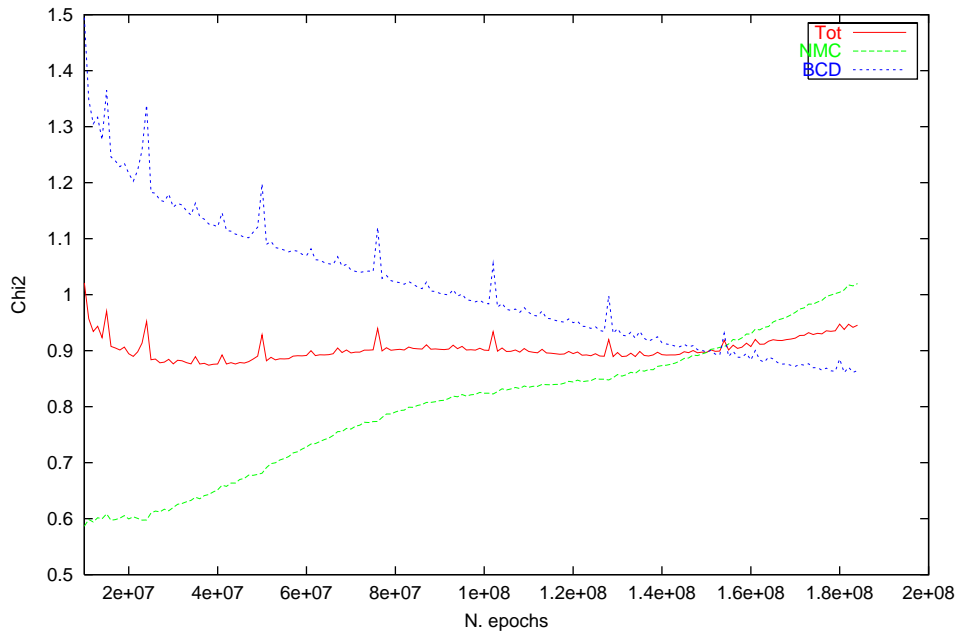
- [50] D. E. Groom *et al.* [Particle Data Group Collaboration], *Eur. Phys. J.* **C15** (2000) 1.
- [51] S. Forte, J. I. Latorre, L. Magnea and A. Piccione, [arXiv:hep-ph/0205286].
- [52] K. G. Wilson, *Phys. Rev.* **179** (1969) 1499.
- [53] H. Georgi and H. D. Politzer, *Phys. Rev.* **D14** (1976) 1829.
- [54] A. Piccione and G. Ridolfi, *Nucl. Phys.* **B513** (1998) 301, [arXiv:hep-ph/9707478].
- [55] M. Beneke, *Phys. Rep.* **317** (1999) 1 [arXiv:hep-ph/9807443];
M. Dasgupta, [arXiv:hep-ph/0109220].
- [56] S. I. Alekhin, *Phys. Rev.* **D63** (2001) 094022, [arXiv:hep-ph/0011002].
- [57] S. A. Larin, P. Nogueira, T. van Ritbergen and J. A. Vermaseren, *Nucl. Phys.* **B492** (1997) 338, [arXiv:hep-ph/9605317];
A. Retey and J. A. Vermaseren, [arXiv:hep-ph/0007294].
- [58] W. L. van Neerven and A. Vogt, *Nucl. Phys.* **B568** (2000) 263, [arXiv:hep-ph/9907472];
W. L. van Neerven and A. Vogt, *Phys. Lett.* **B490** (2000) 111, [arXiv:hep-ph/0007362].

- [59] A. L. Kataev, A. V. Kotikov, G. Parente and A. V. Sidorov, *Phys. Lett.* **B417** (1998) 374, [arXiv:hep-ph/9706534];
A. L. Kataev, G. Parente and A. V. Sidorov, *Nucl. Phys.* **B573** (2000) 405, [arXiv:hep-ph/9905310];
J. Santiago and F. J. Yndurain, *Nucl. Phys.* **B563** (1999) 45 [arXiv:hep-ph/9904344].
- [60] A. Vogt, *Nucl. Phys. Proc. Suppl.* **79** (1999) 102, [arXiv:hep-ph/9906337].
- [61] A. D. Martin, W. J. Stirling and R. G. Roberts, *Nucl. Phys.* **B266** (1991) 173
- [62] A. Bodek, UR-1376 *Presented at 6th Rencontres de Blois: The Heart of the Matter: from Nuclear Interactions to Quark - Gluon Dynamics, Blois, France, 20-25 Jun 1994*
R. C. Walker *et al.*, *Phys. Rev.* **D49** (1994) 5671.
- [63] S. Wolfram, *The Mathematica Book*, CUP, Cambridge (1999).
- [64] F. James, *MINUIT Reference manual version 94.1*, CERN Program Library Long Writeup D506 (1994).
- [65] M. Virchaux and A. Milsztajn, *Phys. Lett.* **B274** (1992) 221.

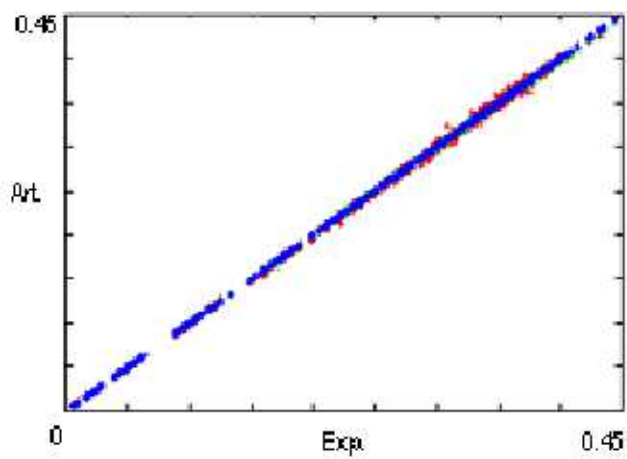
Tools of statistics

- [66] G. D'Agostini, "Bayesian reasoning in high-energy physics: Principles and applications," CERN-99-03.
- [67] G. Cowan, *Statistical data analysis*, Clarendon, Oxford (1998).
- [68] D. Stump *et al.*, [arXiv:hep-ph/0101051];
M. Botje, [arXiv:hep-ph/0110123].
- [69] G. D'Agostini, *Nucl. Instr. Meth.* **A346** (1994) 306.
- [70] S. I. Alekhin, [arXiv:hep-ex/0005042].

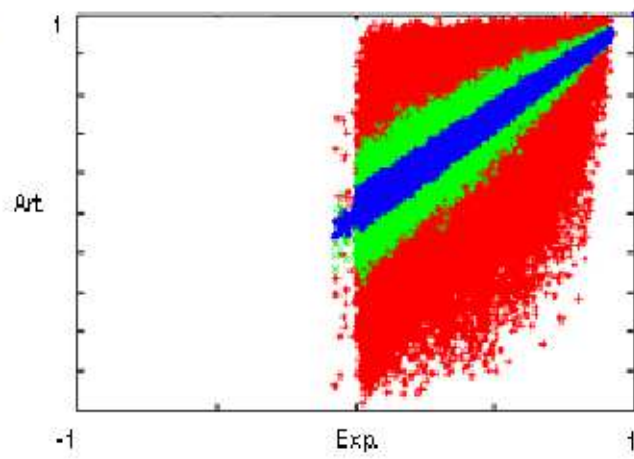
Fit on BCDMS+17 points of NMC

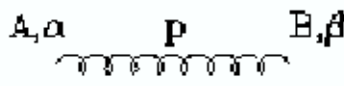


Mean Values

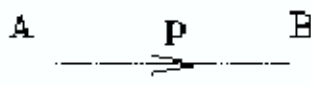


Deuteron

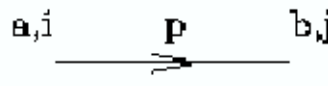




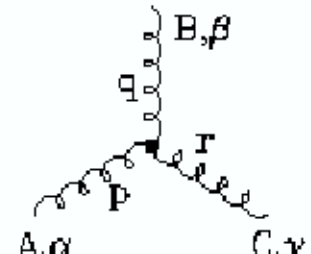
$$\delta^{AB} \left[-g^{\alpha\beta} + (1-\lambda) \frac{p^\alpha p^\beta}{p^2 + i\epsilon} \right] \frac{i}{p^2 + i\epsilon}$$



$$\delta^{AB} \frac{i}{(p^2 + i\epsilon)}$$

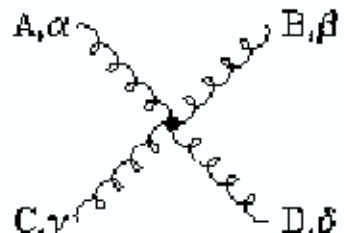


$$\delta^{ab} \frac{i}{(p^2 - m^2 + i\epsilon)_{ji}}$$



$$-g f^{ABC} \left[(p-q)^\gamma g^{\alpha\beta} + (q-r)^\alpha g^{\beta\gamma} + (r-p)^\beta g^{\gamma\alpha} \right]$$

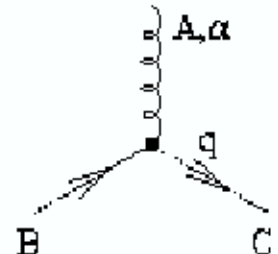
(all momenta incoming, $p+q+r = 0$)



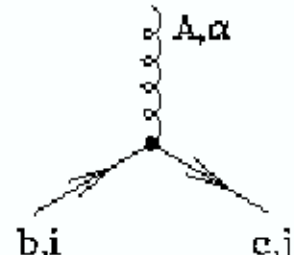
$$-ig^2 f^{XAC} f^{XBD} \left[g^{\alpha\beta} g^{\gamma\delta} - g^{\alpha\delta} g^{\beta\gamma} \right]$$

$$-ig^2 f^{XAD} f^{XBC} \left[g^{\alpha\beta} g^{\gamma\delta} - g^{\alpha\gamma} g^{\beta\delta} \right]$$

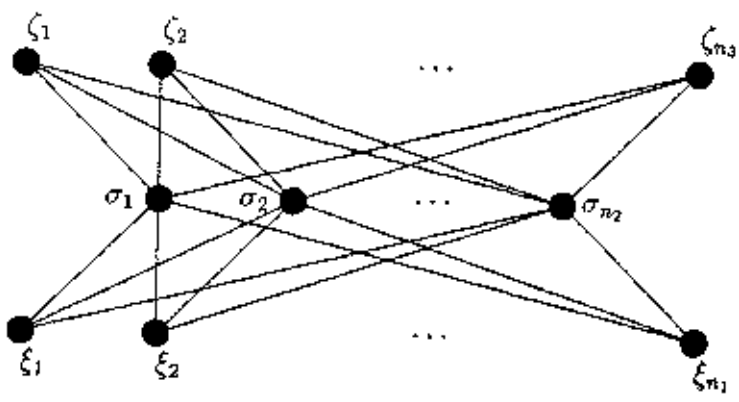
$$-ig^2 f^{XAB} f^{XCD} \left[g^{\alpha\gamma} g^{\beta\delta} - g^{\alpha\delta} g^{\beta\gamma} \right]$$



$$ig f^{ABC} q^\alpha$$



$$-ig (t^A)_{cb} (\gamma^\alpha)_{ji}$$



Output

$$\uparrow \omega_{ij}^{(3)}, \theta_i^{(3)}$$

Hidden

$$\uparrow \omega_{jk}^{(2)}, \theta_j^{(2)}$$

Input

